Realization of low dose XPCS experiments for the investigation of protein dynamics

DISSERTATION
zur Erlangung des Grades eines Doktors
der Naturwissenschaften

vorgelegt von
M.Sc. Hendrik Rahmann
geb. am 22.01.1990 in Norden

eingereicht bei der Naturwissenschaftlich-Technischen Fakultät
der Universität Siegen
Siegen 2020

Erster Gutachter und Betreuer: Prof. Dr. Christian Gutt, Universität Siegen
Zweiter Gutachter: PD Dr. Fajun Zhang, Universität Tübingen
Tag der mündlichen Prüfung: 08.12.2020

Contents

1. Introduction **1**

2. Theoretical Background of X-ray Scattering Techniques **5**

2.1. Basics of X-ray Scattering 5
2.2. Small Angle X-ray Scattering (SAXS) 6
2.3. Coherent X-ray Scattering 9
2.4. X-ray Photon Correlation Spectroscopy (XPCS) 11
2.5. Signal-to-noise ratio of XPCS experiments 14
2.6. Radiation damage 15
2.6.1. Interaction of X-rays and matter and X-ray absorption 16
2.6.2. Radiation damage regarding biological samples 17
2.6.3. Reducing radiation damage effects 20

3. Protein interactions and phase transitions **23**

3.1. Biomolecular crowding and biocondensates 23
3.2. Intermolecular interactions in protein solutions 24
3.3. Thermodynamic fundamentals of phase transitions 27
3.4. Spinodal decomposition and Cahn-Hilliard equation 28
3.5. Arrested State and Glass Transition 32
3.6. IgG-PEG model system 35

4. Experimental setup and sample environment **39**

4.1. PETRA III synchrotron at DESY 39
4.2. The P10 Coherence Applications Beamline 41
4.2.1. The USAXS setup 42
4.2.2. The SAXS setup 44
4.3. Data treatment using Eiger 4M detector 45
4.4. IgG sample preparation 45
4.5. IgG sample measurement protocol 46
4.5.1. USAXS-XPCS measurements 46
4.5.2. SAXS-XPCS measurements 47

5. Data Analysis and Discussion **49**

5.1. Raw data preparation 49

5.2. Radiation damage to IgG proteins 52
5.2.1. Radiation damage measurements in USAXS setup 52
5.2.2. Radiation damage measurements in SAXS setup 55
5.3. USAXS analysis of the quenched IgG model system 58
5.3.1. Kinetics 58
5.3.2. Aging dynamics at small q 62
5.3.3. USAXS data discussion 75
5.4. SAXS data 79
5.4.1. SAXS data discussion 83

6. Conclusion and Outlook **85**

A. Appendix **87**

Abstract

In the cell cytoplasm proteins are surrounded by water and a crowd of macromolecules. For a quantitative understanding of the cellular system knowledge of the dynamic processes in this crowded environment is of key importance. Reversible formation of protein condensates guarantee vitally essential functions. Irreversible protein aggregation processes are responsible for protein condensation diseases such as sickle cell anemia. Furthermore protein dynamics in concentrated solutions are relevant for the design of future drugs and important in the food industry. Up to now, static properties of proteins in crowded environments are well investigated, but little is known about their dynamics.

X-ray photon correlation spectroscopy (XPCS) provides access to both the spatial and temporal properties of the sample simultaneously. Using new X-ray sources such as forth generation storage rings, XPCS experiments on time scales from femtoseconds to hours will be feasible. However, the highly intense X-ray beam is also the cause of radiation damage which requires to develop and implement new avenues of low dose XPCS experiments.

This thesis demonstrates the feasibility of Bio-XPCS measurements to investigate protein dynamics during a liquid-liquid phase separation on a hierarchy of length scales from droplet sizes in the region of micrometers down to the single protein length scale at nanometers. Established strategies to mitigate radiation damage, such as cyro-cooling, are not feasible for investigating protein dynamics. Therefore we increased the beam size leading to a reduced photon density on the sample. To optimize the signal-to-noise ratio we employed a large sample-to-detector distance in the USAXS setup at the P10 Coherence Application Beamline at PETRA III to resolve the speckles.

The experiments, performed at the Deutsches Elektronen-Synchrotron (DESY), revealed the dynamics of a protein model system composed of the antibody γ-globulin (IgG) in presence of polyethylene glycol (PEG) during the liquid-liquid phase separation (LLPS). On the protein droplet scale dynamics caused by the interface formation of the LLPS followed by heterogeneous ballistic motion of the protein domains due to interfacial coarsening were identified. Furthermore highly heterogeneous dynamics associated with particle clusters inside the protein rich domains were found on the length scale of nanometers.

Further research regarding protein condensation diseases and the design of future protein drugs will benefit from the methods developed in this thesis by making Bio-XPCS experiments at the new X-ray sources feasible.

Zusammenfassung

Im Zytoplasma der Zelle sind Proteine von Wasser und einer Menge von Makromolekülen umgeben. Für ein quantitatives Verständnis des zellulären Systems ist die Kenntnis der dynamischen Prozesse in dieser gedrängten Umgebung von zentraler Bedeutung. Die reversible Bildung von Proteinkondensaten garantiert lebenswichtige Funktionen. Irreversible Proteinaggregationsprozesse sind für Proteinkondensationskrankheiten wie die Sichelzellanämie verantwortlich. Darüber hinaus ist die Proteindynamik in konzentrierten Lösungen relevant für die Entwicklung zukünftiger Medikamente und wichtig in der Lebensmittelindustrie. Bislang sind die statischen Eigenschaften von Proteinen in überfüllten Umgebungen gut untersucht, aber über ihre Dynamik ist wenig bekannt.
Die Röntgenkorrelationsspektroskopie (XPCS) ermöglicht den gleichzeitigen Zugriff auf die räumlichen und zeitlichen Eigenschaften der Probe. Mit neuen Röntgenquellen, wie Speicherringen der vierten Generation, werden XPCS-Experimente auf Zeitskalen von Femtosekunden bis Stunden möglich sein. Der hochintensive Röntgenstrahl ist jedoch auch die Ursache von Strahlenschäden, was die Entwicklung und Umsetzung neuer Wege für XPCS-Experimente mit niedrigen Dosen erforderlich macht.
Diese Arbeit zeigt die Machbarkeit von Bio-XPCS-Messungen zur Untersuchung der Proteindynamik während einer Flüssig-Flüssig-Phasentrennung auf einer Hierarchie von Längenskalen von Tröpfchengrößen im Bereich von Mikrometern bis hinunter zur Längenskala eines einzelnen Proteins im Nanometerbereich. Etablierte Strategien zur Abschwächung von Strahlenschäden, wie z.B. die Cyro-Kühlung, sind für die Untersuchung der Proteindynamik nicht durchführbar. Deshalb haben wir die Strahlgröße vergrößert, was zu einer verringerten Photonendichte auf der Probe führt. Um das Signal-Rausch-Verhältnis zu optimieren, setzten wir einen großen Proben-Detektor-Abstand im USAXS-Setup an der Beamline P10 an PETRA III ein, um die Speckles auflösen zu können.
Die Experimente, die am Deutschen Elektronen-Synchrotron (DESY) durchgeführt wurden, zeigten die Dynamik während der Flüssig-Flüssig-Phasentrennung (LLPS) eines Protein-Modellsystems, das aus dem Antikörper γ-Globulin (IgG) in Gegenwart von Polyethylenglykol (PEG) besteht. Auf der Protein-Tröpfchenskala wurden Dynamiken identifiziert, die durch die Grenzflächenbildung der LLPS verursacht werden, gefolgt von heterogener ballistischer Bewegung der Proteindomänen aufgrund von Coarsening. Darüber hinaus wurde eine sehr heterogene Dynamik auf der Längenskala von Nanometern gefunden, die mit Bewegung von Partikelclustern innerhalb der proteinreichen Domänen assoziiert ist.

Die weitere Erforschung von Protein-Kondensationskrankheiten und die Entwicklung zukünftiger Protein-Medikamente wird von den in dieser Arbeit entwickelten Methoden profitieren, indem Bio-XPCS-Experimente an den neuen Röntgenquellen durchführbar geworden sind.

1. Introduction

Proteins are biopolymers composed of amino acids which are involved in many vital tasks in living organisms. In the cellular environment proteins are surrounded by a crowd of other molecules such as salts, sugars, water and other proteins. A quantitative understanding of the cellular system requires knowledge of dynamic processes in this crowded environment [71]. Vitally essential functions are guaranteed by reversible formation of protein condensates through processes such as protein aggregation, phase separation or protein self-assembly [9]. However, proteins can also reach an irreversible arrested state like amyloid fibers [87]. Irreversible protein aggregation processes can cause protein condensation diseases like eye cataract [8] or sickle cell anemia [31]. Fibrous depositions were also found in alzheimer brains [1]. Knowledge about dynamic properties of concentrated protein solutions is essential for the design of future protein drugs [89]. Furthermore protein phase separation is an important driving mechanism in the food industry [69]. While static properties of proteins in crowded environments have been studied by Bio-SAXS experiments [25, 24], little is known about their dynamics.

X-ray photon correlation spectroscopy (XPCS) [88] has been established as a technique to study spatial and temporal properties simultaneously by measuring fluctuations in X-ray speckle patterns. Heterogeneous processes can be investigated using multi-speckle two-time correlation functions (TTC) [64]. Intensity autocorrelation functions in the form of Kohlrausch-Williams-Watts functions [99] provide access to dynamical properties of the sample. As XPCS is a coherent measurement technique it will highly benefit from new X-ray sources such as 4th generation storage rings and X-ray free electron lasers (XFEL) [77]. Fourth generation storage rings are based on new multi-bend-achromat (MBA) lattice technology and will lead to an increase in brilliance and coherence of two to three orders of magnitude. An increase by one order of magnitude in coherent flux leads to a two order of magnitude better temporal resolution [72]. Thus XPCS experiments on the microsecond scale or possibly on tens of nanoseconds via correlation of single storage ring pulses will be feasible [84]. Protein XPCS experiments will also be performed at superconducting XFELs. By using the split-and-delay technique time scales in order of the pulse duration on the 100 fs scale and below are accessible [77]. With using new X-ray sources XPCS measurements on time scales from femtoseconds to hours and on length scales from micrometer to the molecular scale will be feasible. Bio-XPCS experiments on a hierarchy

of length scales from droplet sizes in the region of micrometers down to the single protein length scale at nanometers will be performed using the new sources.

For the realization of Bio-XPCS experiments a major challenge is to overcome radiation damage. Synchrotron sources emit a highly intense X-ray beam which can change the sample structure. Atomic scale XPCS experiments usually use small beam sizes adopted to a small coherence volume which lead to doses of MGy and beyond deposited in the sample. The critical dose D_c defines the dose beyond which the sample starts to degrade by radiation [53, 77]. For the protein lysozyme a critical dose $D_c \approx 500\,\mathrm{kGy}$ for crystals at room temperature was reported [90]. Using cryo-cooling lysozyme crystals can withstand up to $\approx 43\,\mathrm{MGy}$ [75]. However, for the realization of a Bio-XPCS experiment cryo-cooling is not feasible because the dynamics at in vivo temperatures are of interest. Another adversity of measuring biological dynamics is that in aqueous solutions incident X-rays interact with water and create hydroxyl and hydroperoxyl radicals which also cause radiation damage to biomolecules [36]. This effect leads to a critical dose of $D_c \approx 0.4\,\mathrm{kGy}$ for lysozyme in aqueous solution [61], which is reached within milliseconds at modern synchrotron rings. Therefore, the realization of Bio-XPCS experiments require a strategy to mitigate radiation damage. Unfortunately some common approaches to overcome radiation damage cannot be applied to Bio-XPCS measurements. Radical scavengers [61] such as glycerol would change the dynamical properties of the sample. The concept of a rapid flow [58] of the sample is ruled out because for coherent measurement methods the same sample volume during the whole measurement time is required. The fast scanning technique X-ray Speckle Visibility Spectroscopy (XSVS) [95] is developed to investigate millisecond to microsecond dynamics but is not suitable for slow dynamics on the scale of minutes.

To overcome this bottleneck of radiation damage a new experimental approach is required. This thesis will show the feasibility of XPCS experiments to study protein dynamics at two length scales. Using an ultra small-angle X-ray scattering (USAXS) setup experiments on the protein droplet size on the micrometer length scale were performed. The design of the experimental parameters were chosen to optimize the signal-to-noise ration (SNR) while reducing the photon density to minimize the X-ray dose accumulated by the sample [72]. Therefore the beam size was increased to $100 \times 100\,\mu\mathrm{m}^2$ leading to a reduced photon density on the sample. This measurement approach requires a long sample-to-detector distance in order to resolve the smaller speckles. The USAXS setup at the P10 coherence application beamline at PETRA III at the Deutsches Elektronen-Synchrotron offers a sample-to-detector distance of 21.2 m to realize this measurement approach. A further challenge was to perform XPCS measurements in the small-angle X-ray scattering (SAXS) setup to reveal dynamics on the length scales of single proteins. Here the difficulties were

a lower speckle contrast and the low scattering intensity at the corresponding large q values, which is four orders of magnitude lower than the scattering intensity in the USAXS experiments. A measurement protocol was developed to obtain a sufficient large SNR by increasing the number of repetitions. This made it possible for the first time to measure correlation functions of protein dynamics on the molecular length scale.
For showing the feasibility of Bio-XPCS measurements a protein model system composed of the antibody γ-globulin (IgG) in presence of polyethylene glycol (PEG) was studied. The system shows a liquid-liquid phase separation with an upper critical solution temperature behaviour. The sample kinetics were already investigated by Da Vela et al. [23], who found an arrested phase transition for deep quenches to low temperatures. This thesis determines a critical dose D_c for the IgG model system and discusses the measured dynamics on both the droplet and the single protein length scale.

The thesis is structured as follows: In chapter 2 an introduction to X-ray scattering is given including the measurement techniques (ultra) small-angle X-ray scattering and X-ray photon correlation spectroscopy. Also the signal-to-noise ratio and the phenomenon of radiation damage are described. Chapter 3 gives an overview about protein interactions and phase transitions and describes the measured IgG-PEG model system. In chapter 4 the experimental setup and the sample environment at the beamline P10 at the Deutsches Elektronen-Synchrotron is introduced. The chapter finishs with the presentation of the measurement protocol. In chapter 5 the experimental data are analysed. A radiation damage threshold for the IgG model system is determined and the sample dynamics are discussed on the domain size scale as well as the single protein length scale. A summary of the results and an outlook on future studies are given in chapter 6.

2. Theoretical Background of X-ray Scattering Techniques

This chapter provides an introduction to the concepts of X-ray scattering. Section 2.2 describes the experimental measurement technique small angle X-ray scattering (SAXS). The following sections present an introduction to coherent X-ray scattering and X-ray photon correlation spectroscopy (XPCS), which is a powerful method for investigating the sample dynamics. Finally, section 2.6 focuses on the phenomenon radiation damage and the question how to perform XPCS measurements using radiation dose sensitive samples. This chapter is based in parts on the book "Elements of Modern X-Ray Physics" by Jens Als-Nielsen and Des McMorrow [2].

2.1. Basics of X-ray Scattering

A scheme of a basic X-ray scattering experiment is shown in Figure 2.1. The X-rays are generated by a synchrotron and are described as a plane electromagnetic wave,

$$\vec{E}\left(\vec{r},t\right) = \vec{\epsilon}\, E_0 \exp\left(i\left(\vec{k}\cdot\vec{r}-\omega t\right)\right), \tag{2.1}$$

characterized by a wavevector $\vec{k}$ along the direction of propagation, an amplitude E_0, an angular frequency ω and a electric polarisation vector $\vec{\epsilon}$. The absolute value of the wavevector $\vec{k}$ is given by

$$k = \frac{2\pi}{\lambda}, \tag{2.2}$$

with an X-ray wavelength,

$$\lambda = \frac{hc}{E}, \tag{2.3}$$

in the region of an Ångström (10^{-10} m), where E is the X-ray energy, h is the Planck constant and c is the speed of light. In an X-ray scattering experiment the incident X-ray wave with wavevector $\vec{k_i}$ is scattered by a sample under a scattering angle 2θ. The scattered X-ray wave with wavevector $\vec{k_f}$ is detected. The scattering vector also known as wavevector transfer is defined as

$$\vec{q} = \vec{k_i} - \vec{k_f}. \tag{2.4}$$

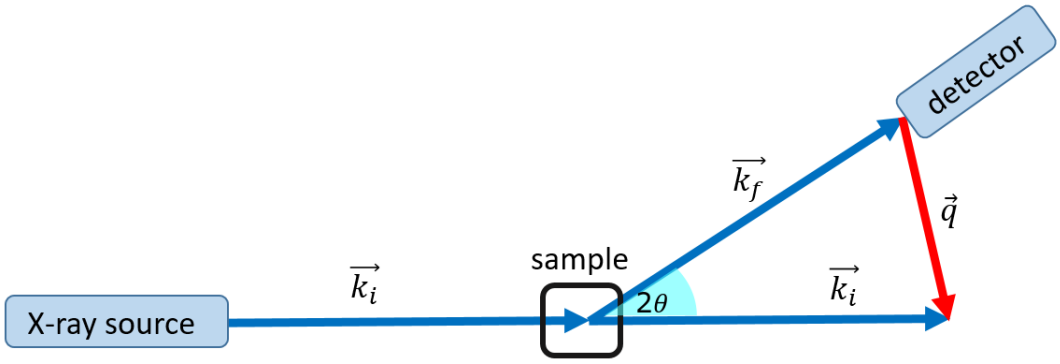

Figure 2.1.: Sketch of an X-ray scattering experiment setup. The incoming wave described by the wave vector $\vec{k_i}$ illuminates the sample. The scattered wave vector $\vec{k_f}$ under an angle of 2θ is measured by the detector. $\vec{q}$ is the scattering vector.

For elastic scattering the energy of the incident and the scattered wave are same and the magnitude of the scattering vector $\vec{q}$ is given by

$$|\vec{q}| = \frac{4\pi}{\lambda} \sin \frac{2\theta}{2}. \tag{2.5}$$

The amplitude of the scattered X-ray wave is described by

$$A_s(\vec{q}) = \sum_j f_j(\vec{q}) \exp(i\vec{q} \cdot \vec{r_j}), \tag{2.6}$$

where the index j is labeling the different atoms, $f_j(\vec{q})$ is the atomic form factor and $\vec{r_j}$ is the position of the jth atom. The scattered intensity,

$$I_s(\vec{q}, t) = \frac{1}{t_{exp}} \int_t^{t+t_{exp}} A_s(\vec{q}, t') A_s^*(\vec{q}, t') \, \mathrm{d}t', \tag{2.7}$$

over an exposure time t_{exp} can be measured by the detector.

2.2. Small Angle X-ray Scattering (SAXS)

Information on the sample structure and shape can be deduced from the scattered intensity $I_s(\vec{q})$. To analyse structures at mesoscopic length scales (1 nm to 1 μm) such as protein samples (ultra) small-angle X-ray scattering is a convenient method. The momentum transfer q determines the characteristic length scales ξ which can be detected via

$$\xi = \frac{2\pi}{q}. \tag{2.8}$$

X-ray scattering at very small scattering angles and momentum transfers ($4 \cdot 10^{-3}\,\mathrm{nm}^{-1}$ to $5 \cdot 10^{-2}\,\mathrm{nm}^{-1}$) is referred as ultra small-angle X-ray scattering (USAXS). Due to eq. (3.35) large protein domains at micrometer scale can be observed using USAXS. Measurements at larger q-values up to $1.5\,\mathrm{nm}^{-1}$ related to smaller structures are called small-angle X-ray scattering (SAXS). The following equations are valid for USAXS and SAXS as both measurement techniques follow the same formalism.
The scattered intensity $I_{\mathrm{saxs}}(\vec{q})$ is given by

$$I_{\mathrm{saxs}}(\vec{q}) = I_0 \cdot t_{\mathrm{exp}} \cdot T_{\mathrm{sample}} \cdot d \cdot \frac{\mathrm{d}\Sigma}{\mathrm{d}\Omega}(\vec{q}), \tag{2.9}$$

where I_0 is the incident flux, t_{exp} is the exposure time, T_{sample} is the sample transmission and d is the sample thickness. The scattering cross section for a monodisperse sample is defined as

$$\frac{\mathrm{d}\Sigma}{\mathrm{d}\Omega}(\vec{q}) = C \cdot M \cdot v^2 \cdot \Delta\rho^2 \cdot P(\vec{q}) \cdot S(\vec{q}), \tag{2.10}$$

where $\Delta\rho$ is the scattering contrast between the protein sample and water. C is the concentration, M is the molar mass and v is the specific volume, respectively. An exemplary protein scattering cross section $\frac{\mathrm{d}\Sigma}{\mathrm{d}\Omega} = 1.03 \pm 0.06\,\mathrm{m^2 kg^{-1}}$ for lysozyme is reported by [73]. The average interparticle structure factor, $S(\vec{q})$, is given by

$$S(\vec{q}) = \frac{1}{N}\left\langle \sum_{j\neq k}^{N}\sum_{1}^{N} \exp\left(-i\vec{q}\cdot(\vec{r_j} - \vec{r_k})\right)\right\rangle, \tag{2.11}$$

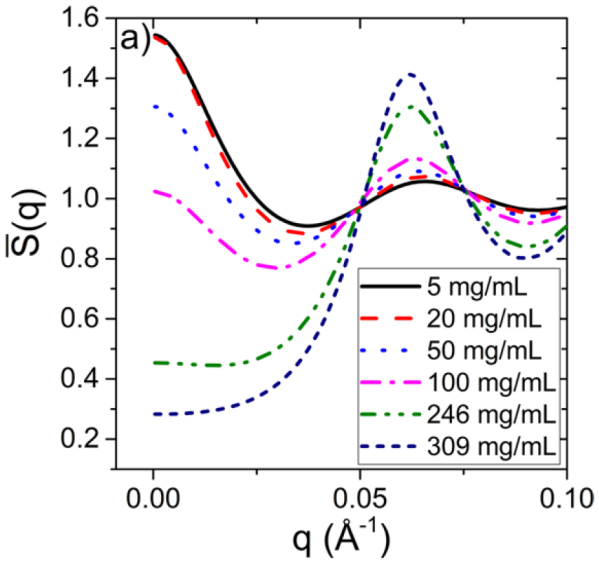

Figure 2.2.: Structure factor of IgG in pure water measured by SAXS [24].

where $\langle ... \rangle$ denotes a statistical average over all orientations, N is the number of particles, $\vec{r_j}$ is the jth atom and $\vec{r_k}$ is the kth atom position. In Figure 2.2 the structure factor of IgG is shown describing the inter-molecular interactions of the proteins. For low protein concentrations Figure 2.2 shows a strong low q upturn indicating the presence of attractive interactions on the corresponding length scale.
The particle formfactor, $P(\vec{q})$, is defined as the square of the Fourier transform of the electric charge distribution $\Delta\rho\left(\vec{r_j}, t\right)$:

$$F_j\left(\vec{q}, t\right) = \int_{V_j} \Delta\rho\left(\vec{r_j}, t\right) \exp\left(\mathrm{i}\vec{q}\cdot\vec{r_j}\right) \mathrm{d}V_j, \tag{2.12}$$

$$\begin{aligned} P(\vec{q}) &= \langle |F(\vec{q})|^2 \rangle = \langle F(\vec{q}) \cdot F^*(\vec{q}) \rangle \\ &= \left\langle \int \int_V \Delta\rho(\vec{r_1}) \Delta\rho(\vec{r_2}) \exp\left(\mathrm{i}\vec{q}\cdot(\vec{r_1} - \vec{r_2})\right) \mathrm{d}\vec{r_1}\mathrm{d}\vec{r_2} \right\rangle \\ &= \left\langle \int \int_V \Delta\rho(\vec{r_1}) \Delta\rho(\vec{r_1} - \vec{r}) \exp\left(\mathrm{i}\vec{q}\cdot\vec{r}\right) \mathrm{d}\vec{r_1}\mathrm{d}\vec{r} \right\rangle \end{aligned} \tag{2.13}$$

using $\vec{r} = \vec{r_1} - \vec{r_2}$. The auto-correlation function, $g(\vec{r})$, is established as the convolution square $\Delta\tilde{\rho}^2(\vec{r})$ of the density fluctuations

$$g(\vec{r}) = \Delta\tilde{\rho}^2(\vec{r}) = \int_V \Delta\rho(\vec{r_1}) \Delta\rho(\vec{r_1} - \vec{r}) \mathrm{d}\vec{r_1}. \tag{2.14}$$

Using eq. (2.14) the particle formfactor can be rewritten as

$$P(\vec{q}) = \left\langle \int g(\vec{r}) \exp\left(\mathrm{i}\vec{q}\cdot\vec{r}\right) \mathrm{d}\vec{r} \right\rangle. \tag{2.15}$$

The IgG particle form factor describing the shape of the protein is shown in Figure 2.3.

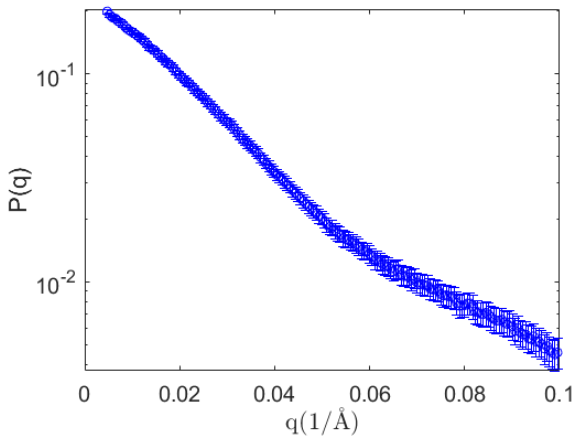

Figure 2.3.: Particle form factor of 5 mg/ml IgG measured by SAXS [24].

2.3. Coherent X-ray Scattering

In the previous sections we assumed a coherent beam with a perfect plane-wave state. For an X-ray experiment there are deviations from this assumption, the beam is neither perfectly monochromatic nor it is propagating in a perfectly well defined direction. The threshold of this assumption is given by the coherence length L of an X-ray beam. In the left part of Figure 2.4 two X-ray waves A and B with wavelengths λ and $\lambda - \Delta\lambda$ and with the same direction of propagation emitted by a source with the bandwidth $\frac{\Delta\lambda}{\lambda}$ are shown. In P both waves are in phase. The longitudinal coherence length,

$$L_L = \frac{1}{2}\frac{\lambda^2}{\Delta\lambda}, \tag{2.16}$$

describes the distance from the X-ray source where A and B are out of phase.
The right part of Figure 2.4 demonstrates the case of two perfect monochromatic X-ray waves A and B with a derivation in the direction of propagation by an angle of $\Delta\theta$ emitted by the ends of a source with size D. In the case that the observation point P is in a distance R from the X-ray source, then $\Delta\theta = \frac{R}{D}$ and the transversal coherence length is given by

$$L_T = \frac{\lambda}{2}\left(\frac{R}{D}\right). \tag{2.17}$$

The experiments presented in the thesis were conducted at the coherence application beamline P10 where at 90 m from the source and at 8 keV photon energy, the transverse coherence length is 277 μm in the vertical direction and 46 μm in the horizontal direction [27]. The coherence length determines an upper limit on the distance between two objects

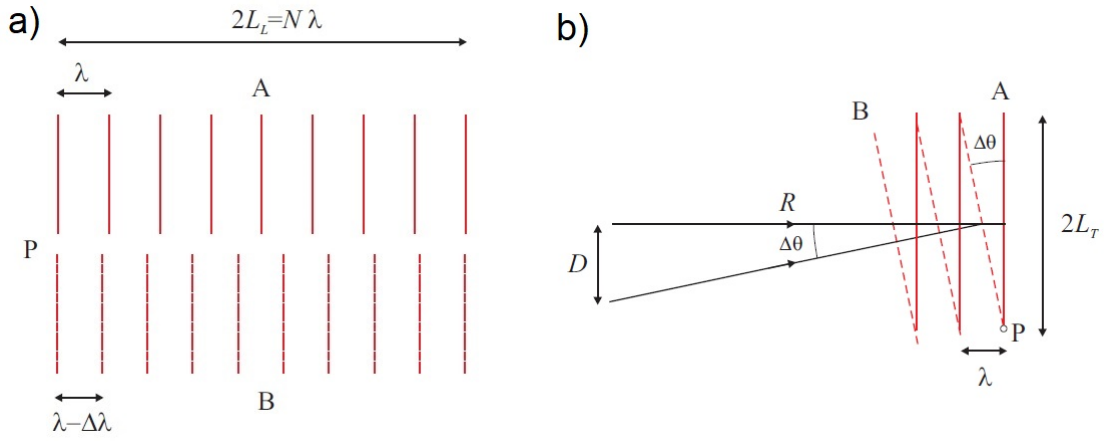

Figure 2.4.: a) longitudinal coherence length: After a distance L_L two plane waves with different wavelengths are out of phase by the factor π [2].
b) transversal coherence length: Two waves with the same wavelength are emitted from the ends of a source of height D [2].

to show interference phenomena. If this distance is larger than the coherence length the detector will measure the summed intensity of both objects instead of an interference signal.
A coherent X-ray experiment measures interference phenomena whose visibility increases with the coherence of the X-rays. The mutual coherence function [42],

$$\vec{\gamma}(\vec{P_1}, \vec{P_2}, \Delta t) = \left\langle \vec{E}(\vec{r_1}, t)\vec{E}^*(\vec{r_2}, t + \Delta t) \right\rangle_t \tag{2.18}$$

defines the correlation between two electric fields $\vec{E}(\vec{r_1}, t)$ and $\vec{E}(\vec{r_2}, t)$ over a time average $\langle ... \rangle_t$. In Young's double slit experiment a source illuminates two pinholes at the positions $\vec{P_1}$ and $\vec{P_2}$, exemplary. The scattered intensity $I(\vec{q})$ is measured on a screen at a point $\vec{q}$ with the distance r_1 from P_1 and the distance r_2 from P_2. $I(q)$ is given by

$$I(\vec{q}) = I_1(\vec{q}) + I_2(\vec{q}) + \vec{k_1}\vec{k_2}^*\vec{\gamma}\left(\vec{P_1}, \vec{P_2}, \frac{r_2 - r_1}{c}\right) + \vec{k_2}\vec{k_1}^*\vec{\gamma}\left(\vec{P_2}, \vec{P_1}, \frac{r_1 - r_2}{c}\right). \tag{2.19}$$

$\vec{k_1}$ and $\vec{k_2}$ are complex valued vectors, which describe the diffraction of the waves at the pinholes and c is the speed of light. The normalized mutual coherence function, also called complex degree of coherence, is given by

$$\vec{\gamma_c}(\vec{P_1}, \vec{P_2}, \Delta t) = \frac{\vec{\gamma_c}(\vec{P_1}, \vec{P_2}, \Delta t)}{\sqrt{I(\vec{P_1})I(\vec{P_2})}}, \tag{2.20}$$

where $I(\vec{P_1})$ and $I(\vec{P_2})$ are the averaged intensities emitted at the pinholes. The absolute value of the normalized mutual coherence function is given by

$$0 \leq |\vec{\gamma_c}(\vec{P_1}, \vec{P_2}, \Delta t)| \leq 1, \tag{2.21}$$

where a value of zero corresponds to incoherence and value of one corresponds to maximum coherence. For $I_1(\vec{q}) = I_2(\vec{q})$ the absolute value of the complex degree of coherence without pathlength difference $\gamma_c(\vec{P_1}, \vec{P_2}, 0)$ is equal to the contrast β of the interference pattern

$$\beta = \frac{I_{max} - I_{min}}{I_{max} + I_{min}} = \gamma_c(\vec{P_1}, \vec{P_2}, 0), \tag{2.22}$$

where I_{max} and I_{min} are the maximum and minimum intensity of the speckle pattern. The contrast β can also be written as a function of the longitudinal coherence length L_L, and the transverse coherence length $L_{T,v}$ and $L_{T,h}$ in vertical and horizontal direction [62],

$$\beta = \int\int \exp\left(-\left(\frac{\Delta x}{L_{T,h}}\right)^2\right) \exp\left(-\left(\frac{\Delta y}{L_{T,v}}\right)^2\right) \exp\left(-\left(\frac{\tau_c c}{\sqrt{2}L_L}\right)^2\right) \mathrm{d}V_1 \mathrm{d}V_2, \tag{2.23}$$

where V is the sample volume, τ_c is the coherence time and Δx and Δy are horizontal and vertical distances between two observation points.

2.4. X-ray Photon Correlation Spectroscopy (XPCS)

X-ray Photon Correlation Spectroscopy (XPCS) is a spatiotemporal coherent X-ray probe to measure micro- and nanoscale dynamics. In an XPCS experiment X-rays scattered by randomly distributed particles interfere and intensity fluctuations are measured due to interference effects [88]. The resulting pattern with spots of constructive and destructive interference is called a speckle pattern.

A common XPCS setup is shown in Figure 2.5. Due to motion inside the protein sample the intensity of each detector pixel changes with time. Therefore the pixel intensity at time t is different to the intensity at the time $t+\tau$ with a delay time τ. For small delay times τ compared to the sample fluctuation period $I(\vec{q},t+\tau)$ is in correlation with $I(\vec{q},t)$. With increasing delay time the correlation vanishs. The degree of correlation of images with exposure time t_e can be measured by the autocorrelation function,

$$\langle I(\vec{q},t)I(\vec{q},t+\tau)\rangle = \lim_{t_e\to\infty}\frac{1}{t_e}\int_0^{t_e} I(\vec{q},t)I(\vec{q},t+\tau)\mathrm{d}t, \tag{2.24}$$

where $\langle ...\rangle$ denotes the time average of all times $t_{start} < t < t_{stop}$. The normalized intensity autocorrelation function

$$g_2\left(\vec{q},\tau\right) = \frac{\langle I\left(\vec{q},t\right) I\left(\vec{q},t+\tau\right)\rangle}{\langle I\left(\vec{q},t\right)\rangle^2} \tag{2.25}$$

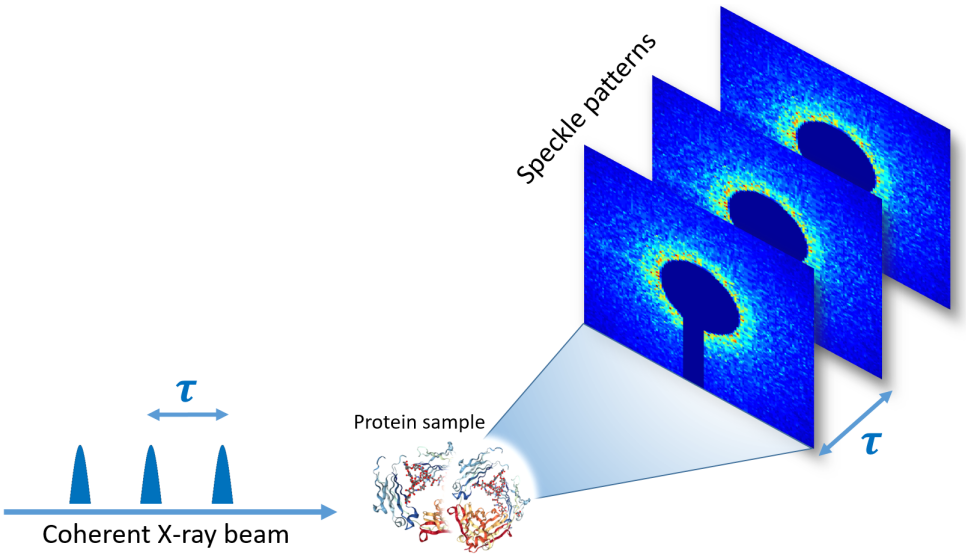

Figure 2.5.: Sketch of an XPCS experiment: Coherent incident X-rays are scattered by a protein sample. Speckle patterns with a delay time τ are recorded with a pixelated 2D array detector.

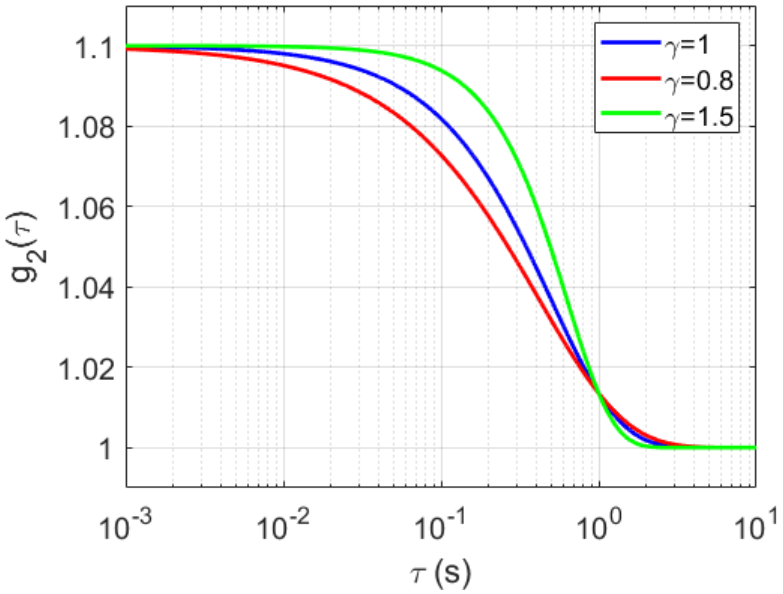

Figure 2.6.: Correlation functions with the parameters $\beta = 0.1$, $\Gamma = 1$ and different KWW exponents γ.

is associated with the intermediate scattering function also called normalized field autocorrelation function

$$g_1(\vec{q}, \tau) = \exp\left(-\left(\Gamma\tau\right)^{\gamma}\right) \tag{2.26}$$

via the Siegert relation [5]

$$g_2(\vec{q}, \tau) = 1 + \beta|g_1(\vec{q}, \tau)|^2 = 1 + \beta \exp\left(-2\left(\Gamma\tau\right)^{\gamma}\right). \tag{2.27}$$

The sample dynamics can be characterised by the speckle contrast β, the decay rate Γ and the Kohlrausch-Williams-Watts (KWW) exponent γ. The exponent γ provides information on the type of sample dynamics. For example brownian diffusive dynamics lead to $\gamma = 1$. In the case of brownian diffusive motion the decay rate Γ follows

$$\Gamma = Dq^2, \tag{2.28}$$

where D is the Stokes-Einstein diffusion coefficient

$$D = \frac{k_b T}{6\pi\eta R_h} \tag{2.29}$$

with the Boltzmann constant k_B, temperature T, viscosity η and the hydrodynamic radius R_h. Ballistic motion is known from colloidal gelation processes and lead to KWW exponents $\gamma > 1$ and follows a linear

$$\Gamma \propto q \tag{2.30}$$

behaviour [6]. The speckle contrast β is given by eq. (2.22). In Figure 2.6 correlation functions with different values for γ are shown.
The time average in eq. (2.25) is only valid for the assumption that the dynamics are stationary over the duration of the measurement. For out-of-equilibrium behaviour such as ageing or radiation damage effects the calculation of the time average to get the correlation function is not allowed [64]. Thus, the analysis has to be a function of waiting time t_w after the measurement start. Instead of the time average an ensemble average over equivalent scattering vectors can be used. In this case the two-time correlation function (TTC), which is defined as

$$ttc\left(\vec{q}, t_1, t_2\right) = \frac{\left\langle I\left(\vec{q}, t_1\right) I\left(\vec{q}, t_2\right)\right\rangle}{\left\langle I\left(\vec{q}, t_1\right)\right\rangle \left\langle I\left(\vec{q}, t_2\right)\right\rangle} \tag{2.31}$$

has to be analysed. Here $\langle ... \rangle$ denotes the average over the ensemble of pixels corresponding to a range of scattering vectors [64]. In Figure 2.7 a TTC of the liquid-liquid phase separation in a protein system, which demonstrates an ageing effect, is shown. By making horizontal cuts from the TTC diagonal $g2$ functions can be extracted starting from a waiting time t_w as marked by red arrows in Figure 2.7 [10]. In the case of a sample showing two dynamical relaxations the system can be modelled using a two exponential correlation function

$$g_2(\vec{q}, \tau) = 1 + \beta_1 \exp\left(-2\left(\Gamma\tau\right)^{\gamma_1}\right) + \beta_2 \exp\left(-2\left(\Gamma_2\tau\right)^{\gamma_2}\right). \tag{2.32}$$

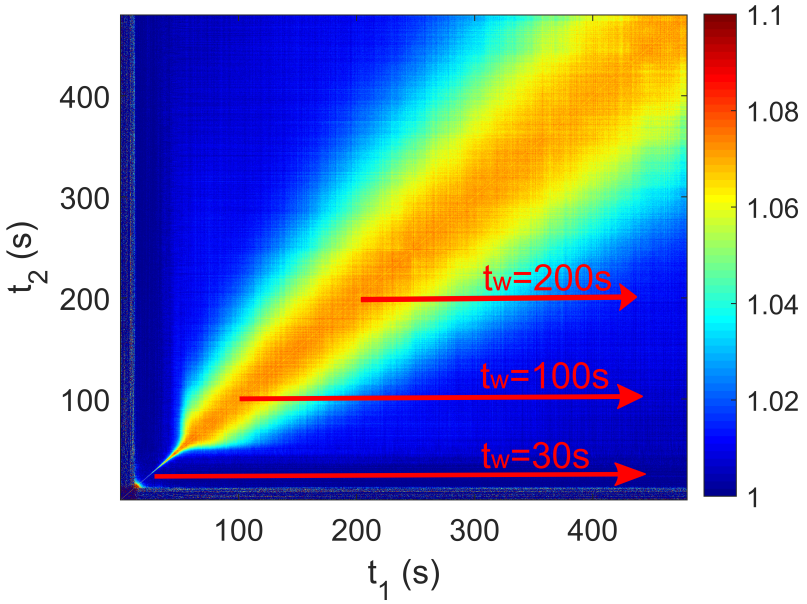

Figure 2.7.: Two time correlation function measured with a IgG-PEG protein sample.

2.5. Signal-to-noise ratio of XPCS experiments

In order to define several setup parameter it is important to know their influence on the signal-to-noise ratio (SNR) [72]. The SNR for the autocorrelation function eq. (2.27) is given by [32]

$$\mathrm{SNR} = \beta \cdot I_{pix} \cdot \sqrt{N} \tag{2.33}$$

with

$$N = N_{pix} \cdot N_{Image} \cdot N_{rep}, \tag{2.34}$$

where I_{pix} is the average intensity per pixel, β is the contrast, N_{pix} is the number of pixels and N_{rep} is the number of repetitions, respectively. $N_{Image} = \frac{t_{total}}{t_{exp}}$ is the number of frames with t_{exp} being the single-image exposure time and t_{total} being the total accumulated exposure time for N_{Image}. I_{pix} is proportional to the incoming coherent flux F_c, which is defined as

$$F_c = B\frac{\lambda^2}{4}. \tag{2.35}$$

with wavelength λ and the source brilliance B at beamline P10 at PETRA III [28]

$$B = 10^{20}\,\frac{\text{Photons}}{\text{s mm}^2\ \text{mrad}^2\ 0.1\%\ \text{BW}}. \tag{2.36}$$

Considering

$$\mathrm{SNR} \propto F_c\sqrt{t_{exp} \cdot t_{total}} \tag{2.37}$$

increasing F_c by one order of magnitude leads access to two orders of magnitude faster dynamics while retaining the SNR [72]. The speckle contrast β depends on the transverse and longitudinal coherence length as well as several experimental parameters like the speckle size

$$S = \frac{\lambda L}{a}, \tag{2.38}$$

the sample-to-detector distance L, the sample thickness d and the beam size a. The speckle contrast β can be written as

$$\beta(a, d, q, \lambda, L) = \beta_{cl}(a, d, q, \lambda) \cdot \beta_{res}(a, L, \lambda), \tag{2.39}$$

where β_{cl} is the contrast reduction from unity due to the finite coherence lengths (2.22) and β_{res} depends on the angular resolution of the experimental setup. The maximum β_{res} can be reached using a setup, which enables

$$S \geq P \tag{2.40}$$

with the pixel size P. In order to reduce radiation damage effects, which are described in section 2.6, one possibility is to increase the beam size a to reduce the photon density on the

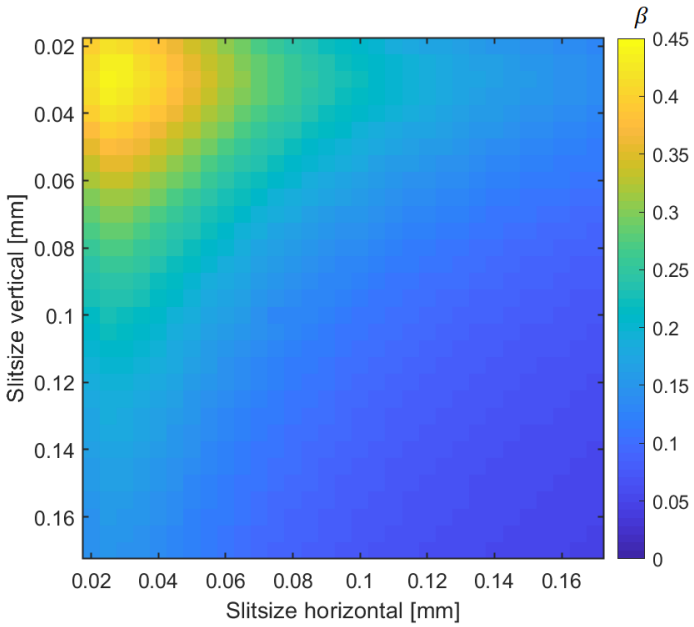

Figure 2.8.: Maximum contrast in P10 USAXS setup depending on the beamsize. Setup parameter are $E = 8\,\mathrm{keV}$, $L = 21.3\,\mathrm{m}$ and $P = 75\,\mu\mathrm{m}$.

sample. In order to satisfy the condition (2.40), XPCS experiments with a large beam size require a long sample-to-detector distance L. The thresholds to increase the beamsize are given by the transversal coherence length and the maximum sample-to-detector distance L feasible at the beamline. In Figure 2.8 the maximum contrast in USAXS setup in dependence of the beamsize is shown.
When defining the setup parameters, it is important that the critical dose D_c of the sample discussed in section 2.6.2 is not exceeded. The maximum number of images N_{im} which can be recorded below D_c is increasing with the photon energy E because the absorption length of X-ray is increasing and the radiation dose is spread over a larger sample volume [72]. Furthermore, it must be noted that the speckle contrast β is decreasing at large q.

2.6. Radiation damage

X-rays scattering is a powerful method to investigate the structure of materials due to their weak interaction with matter. In order to reach a high SNR a high X-ray intensity is favorable. At a third generation synchrotron source the high brilliance increased the X-ray dose which is deposited inside the sample to magnitudes which can change the properties of sample material. This phenomenon is called radiation damage. Biological samples are particularly sensitive to radiation damage (see section 2.6.2). A major challenge to perform an XPCS experiment using protein samples is to measure using a high SNR without damaging the sample. Thus in the beginning of the experiments a radiation

damage threshold has to be determined. Also the measurement setup has to be optimised reaching the maximum SNR while respecting this radiation damage threshold.

2.6.1. Interaction of X-rays and matter and X-ray absorption

To quantify the sample scattering efficiency in dependence on the photon energy the differential cross-section

$$\frac{d\sigma}{d\Omega} = \frac{(\text{Scattered X-ray photons per second into } \Delta\Omega)}{(\text{Incident flux})\Delta\Omega} \tag{2.41}$$

is considered. The scattered intensity I_{sc} into the solid angle of the detector $\Delta\Omega$ is normalized by the incident flux and the solid angle of the detector $\Delta\Omega$. Radiation damage is caused by X-ray photon absorption by the sample. The absorption can be quantified by the energy dependent linear absorption coefficient μ. At a depth z from the surface the X-ray intensity $I(z)$ is described by the Beer-Lambert-Law

$$I(z) = I_0 \exp(-\mu z). \tag{2.42}$$

The absorption cross section σ_a is given by

$$\sigma_a = \frac{\mu A}{\rho_m N_A}, \tag{2.43}$$

where N_A is Avogadro's number, A is the atomic mass number and ρ_m is the mass density, respectively. During an X-ray scattering experiment there are three main types how X-rays and matter can interact: absorption, coherent (Section 2.3) or incoherent scattering, and pair production [48]. The photoelectric effect is the dominant process at low energies. A photon with energy E_{ph} is absorbed causing that an electron with energy

$$E_{el} = E_{ph} - E_B \tag{2.44}$$

and binding energy E_B is removed from its shell. The cross section of the photoelectric effect is given by

$$\sigma \propto \begin{cases} \frac{Z^5}{(h\nu)^{3.5}}, \text{ if } E_{ph} < m_e c^2 \\ \frac{Z^5}{h\nu}, \text{ otherwise} \end{cases} \tag{2.45}$$

with electron rest energy m_e, the Planck constant h, the frequency ν and the atomic number Z. In compton scattering a photon is scattered incoherently by an electron bound in the atomic shell under an incident angle θ. The photon transfers a certain energy to the electron which results in a photon energy change

$$\nu' = \frac{\nu}{1 + (1 - \cos\theta)\frac{h\nu}{m_e c^2}}. \tag{2.46}$$

The compton scattering cross section is given by

$$\sigma \propto \frac{Z}{h\nu}. \tag{2.47}$$

Figure 2.9 shows the absorption cross section for carbon for the different types of X-ray interaction. The measurements regarding this thesis were performed using a photon energy of 8.54 keV and 13 keV. At this energy, photoabsorption is the predominant radiation damage process.

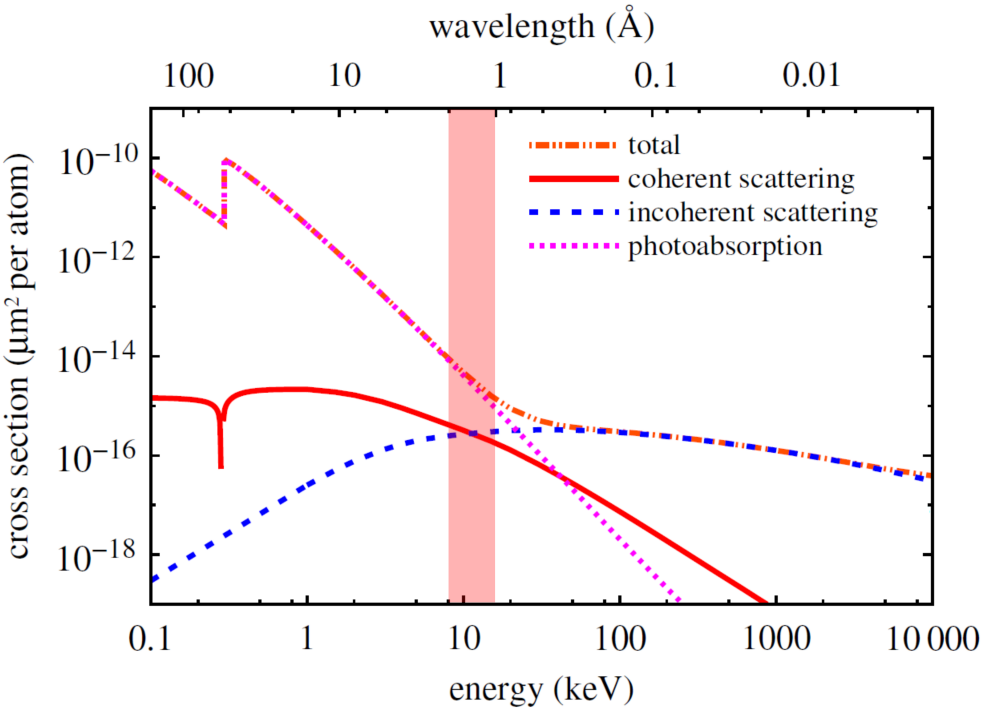

Figure 2.9.: Absorption cross section of carbon for different energies, data taken from [91]. The typical photon energy of XPCS experiments is marked by the red box.

2.6.2. Radiation damage regarding biological samples

Soft matter samples, especially biological samples, are highly sensitive to radiation damage because their molecular bonds can be quite easily broken. Protein aggregation results from radiation damage in X-ray experiments at high-brilliant synchrotron sources [61]. Direct radiation damage changes the structure of molecules with the possibility of loss of crystallinity to a more amorphous system [47]. In indirect radiation damage incident X-rays interact with water and create hydroxyl and hydroperoxyl radicals which can attach to proteins [36]. The production of free radicals due to the radiolysis and ionization of water is shown in Figure 2.10. Within 100 fs X-rays are causing water excitation and ionization, which is the origin of over 80% of the energy deposit in cells [47]. Free radicals

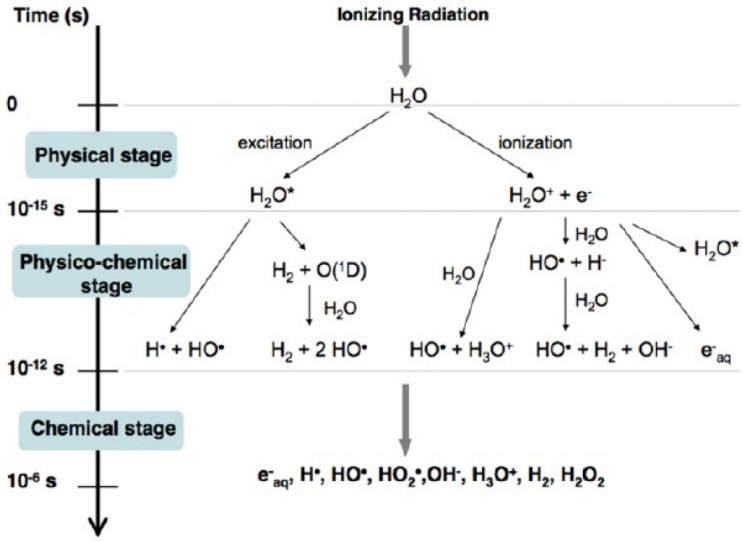

Figure 2.10.: Scheme showing the production of free radicals during water radiolysis [47].

are also formed by protein X-ray absorption. These processes combined lead to a very fast radical activation of the protein polypeptide chain [53]. To quantify beam damage effects the absorbed energy of the sample is transferred to an X-ray dose, which measures the absorbed energy per mass,

$$D = \frac{E}{m}, \tag{2.48}$$

in units of Gray ($1\,\mathrm{Gy} = 1\,\frac{\mathrm{J}}{\mathrm{kg}}$). For a protein SAXS (-XPCS) experiment D is given by

$$D = \frac{F_0 \cdot E_{ph} \cdot A(E,d) \cdot \phi \cdot t_{total}}{V_{irr} \cdot \rho}, \tag{2.49}$$

where F_0 is the incident photon flux, E_{ph} is the photon energy, ϕ is the protein volume fraction and ρ is the protein density. A denotes the sample X-ray absorption at the chosen photon energy and sample thickness d. The irradiated sample volume

$$V_{irr} = x_b \cdot y_b \cdot d = a \cdot d \tag{2.50}$$

is determined by the horizontal size x_b, the vertical size y_b of the X-ray beam and the sample thickness. The total accumulated exposure time t_{total} is given by

$$t_{total} = N_{image} \cdot t_{exp}, \tag{2.51}$$

where N_{image} is the number of images and t_{exp} is the single image exposure time. Each sample can be irradiated with a tolerable critical dose D_c before its structure is changed by radiation damage. This critical dose D_c has to be identified before XPCS experiment can be performed in compliance with D_c. Kuwamoto et al. determined $D_c \approx 400\,\mathrm{Gy}$ for

lysozyme in aqueous solution by SAXS measurements [61]. The radius of gyration R_g can be determined by fitting the SAXS intensity profile using the Guinier approximation [43],

$$I(S) = I(0) \exp\left(\frac{-4\pi^2 R_g^2 S^2}{3}\right), \tag{2.52}$$

where $S = 2\pi q$ is the reciprocal parameter and $I(0)$ is the forward-scattering intensity. SAXS measurements of a lysozyme sample with different doses are shown in Figure 2.11a. Radiation damage due to protein aggregation becomes visible in an increase of SAXS intensity at small q-values, which belong to larger length scales via (3.35). To quantify protein aggregation the ratios of R_g^2 and I_0 are considered, which are defined by the following,

$$F_{RG} = \frac{(R_G^2)_D}{(R_G^2)_0}, \tag{2.53}$$

$$F_{I0} = \frac{I(0)_D}{I(0)_0} = \frac{\sum_m m^2 N_m}{\sum_m m N_m}, \tag{2.54}$$

where the subscript D denotes the accumulate dose and N_m is the molar number of the m-mer of lysozyme. The forward-scattering intensity I_0 is proportional to the square of m. Hence, an increase in F_{I0} indicates radiation-induced aggregation. Figure 2.11b shows the occurrence of radiation damage for lysozyme above the critical dose $D_c \approx 400\,\mathrm{Gy}$ for a protein concentration of 4.9 $\frac{mg}{mL}$.

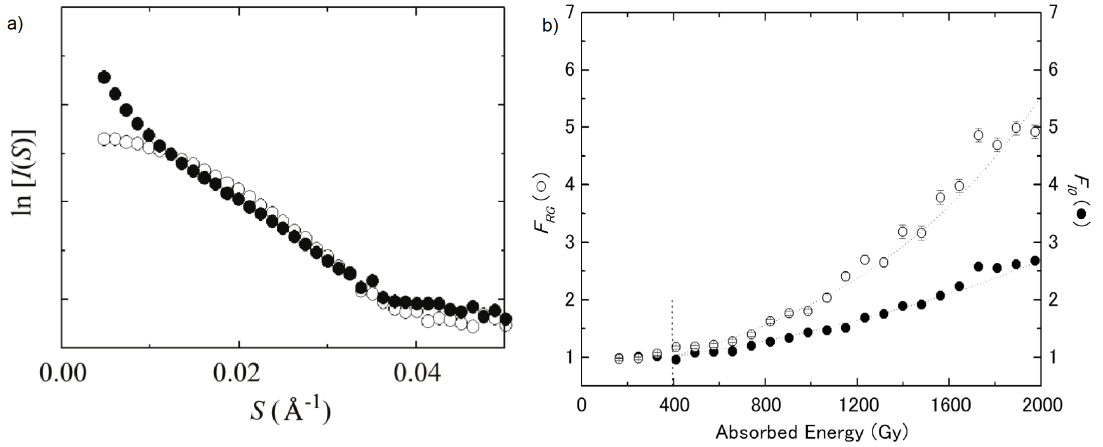

Figure 2.11.: a) Change in SAXS of lysozyme caused by radiation-induced aggregation. The protein concentration was 4.9 $\frac{mg}{mL}$. Open circles represents short-exposure (165 Gy) and solid circles express long-exposure (3300 Gy) [61].
b) Dependence of R_g and $I(0)$ on the accumulated dose. The protein concentration was 4.9 $\frac{mg}{mL}$. Radiation damage occurs above 400 Gy [61].

The aggregation process above the critical dose follows an exponential function (broken lines in Figure 2.11b),

$$Y = \exp\left(k_{app}(X - 400)\right), \tag{2.55}$$

where is k_{app} is the apparent rate of aggregation, X is the absorped energy and Y is either F_{RG} or F_{I0}.

2.6.3. Reducing radiation damage effects

Radiation damage effects in solution depend on the protein concentration. In Figure 2.12 F_{I0} is shown for different lysozyme concentrations. For dilute samples concentration F_{I0} is increasing faster than for dense concentrated samples [15, 61].

Radiation damage can also be reduced by adding radical scavengers such as PEG to the

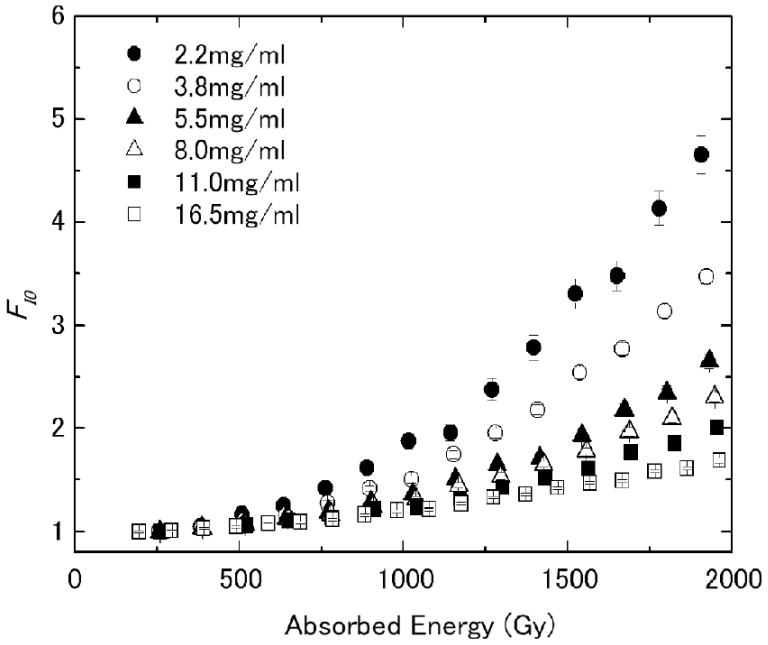

Figure 2.12.: Effect of the protein concentration on the radiation-induced aggregation [61].

sample [47, 59]. In general, the use of cryogenic temperatures diminish radiation damage by reducing the diffusion of free radicals [47]. With regard to this thesis, cryogenic technology is not feasible, since the temperature is a measurement variable. Some properties of the setup can be adjusted to reduce radiation damage. With an increase in photon energy E, the photoabsorption is decreased more than the coherent scattering (Figure 2.9). The beam diameter can be increased to reduce the photon density on the sample, as described in section 2.5. The incident flux F_c can be reduced using attenuators. Figure 2.12a clearly shows the occurrence of radiation damage after 250 ms using the unattenuated beam, while the measurement recorded with attenuator in Figure 2.12b shows no radiation damage at the same time scale. When setting the attenuator, it is important to find a compromise

that both avoids radiation damage and provides an sufficient SNR. For XPCS experiments on large time scales a 10 Hz fast stutter can be used, which blocks the X-ray beam during a delay time between the single images.

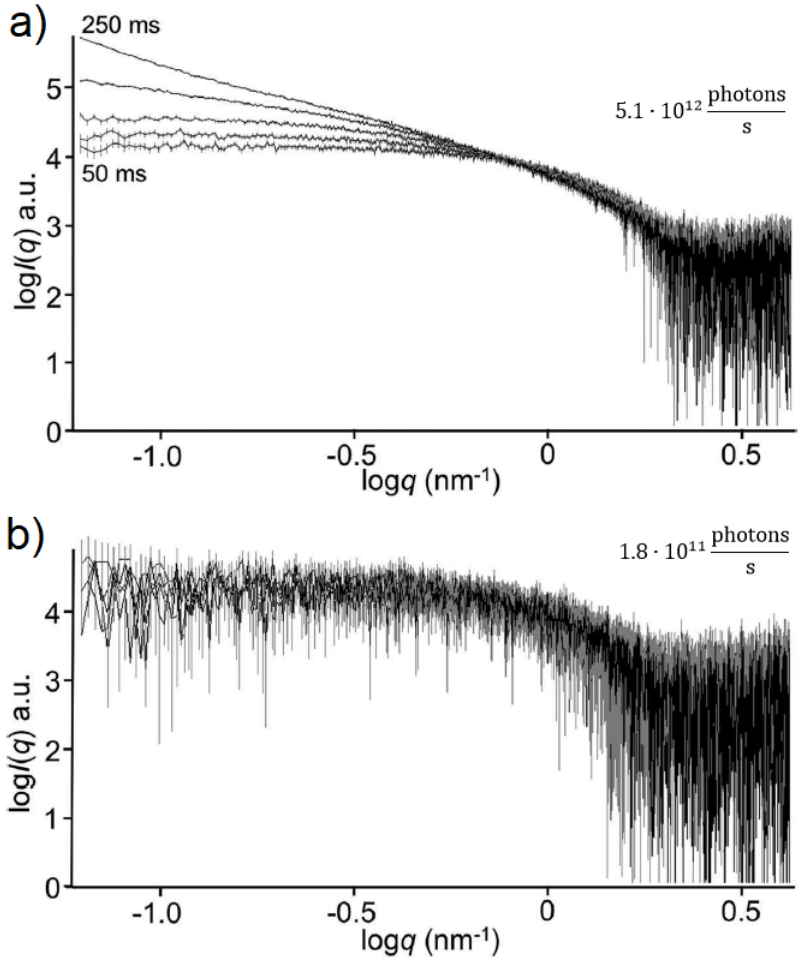

Figure 2.13.: Effect of beam attenuation. SAXS data from 4.4 $\frac{\text{mg}}{\text{mL}}$ lysozyme samples recorded
a) at incident flux $5.1 \cdot 10^{12}$ $\frac{\text{photons}}{\text{s}}$ [53].
b) at attenuated incident flux $1.8 \cdot 10^{11}$ $\frac{\text{photons}}{\text{s}}$ [53].

3. Protein interactions and phase transitions

Proteins are naturally occurring biopolymers and perform vitally important tasks in living organisms. They consists of amino acid monomers which are kept together by peptide bonds. The protein properties are determined by amino acid monomer side chains, which vary in charge, size, polarity and their capability to commit hydrogen bonds. In biology, an important question is how biomolecules like proteins function in a crowded environment [70]. The characteristics of a crowded environment are presented in section 3.1. An introduction to the physics of phase transitions is given by section 3.3 and section 3.4. Finally, the IgG-PEG model system is presented in section 3.6. This chapter is based in parts on the book "The Physics of Phase Transitions" by Pierre Papon et al [76].

3.1. Biomolecular crowding and biocondensates

In the cell cytoplasm proteins are surrounded by water and a crowd of macromolecules including other proteins, lipids and nucleic acids. Since no single type of molecule needs to be present in high concentration, this highly packed viscous environment is called 'crowded' instead of 'concentrated' [33]. Macromolecular concentrations of $300 - 450\,\frac{\mathrm{mg}}{\mathrm{mL}}$ or $25 - 45\,\mathrm{vol}\%$ are typical for a crowded cytoplasm. The volume fraction occupied by proteins of the total cellular volume is around $30\,\%$ [49].
Attractive protein-protein interactions (section 3.2) are an important molecular driving force for the formation of liquid condensates [98]. The process, which describes the self-assemble of liquid-like biomolecule droplets within the cytoplasm is known as liquid-liquid phase separation [101]. During the phase separation an initial mixed equilibrium state converts into a demixed equilibrium state. Phase separation is a transient, nonequilibrium process which is caused by a change of thermodynamic conditions. Systems can reach a phase separation seeking the lowest energy state determined by entropic and enthalpic conditions. Depending on the sample system there are condition-controlling parameters like the temperature or the molecular concentration. These parameters can tilt the balance between contributions like entropy which benefit mixing and others like self-affinity which induce molecular demixing [9]. Entropy driven systems feature a lower critical solution temperature (LCST) phase diagram. If the attractive interaction of a system is energy driven and increasing for lower temperatures, the system will show an upper critical solution temperature (UCST). A phase diagram displaying an UCST is shown in Figure 3.1.

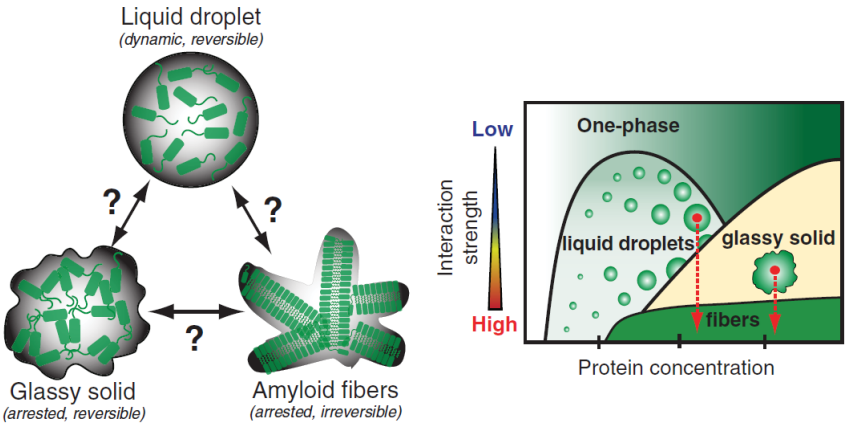

Figure 3.1.: Left: Protein can condense into different high-order structures [87].
Right: Phase diagram as a function of the attractive protein-protein interaction strength [87].

When a sample is quenched from an initial temperature T_0 to a final temperature T the sample becomes phase separated at the critical temperature T_C with $T < T_C < T_0$. With reaching T_C the initially disordered system becomes unstable and small ordered domains are formed as described in section 3.4.
In crowded environments phase transitions play a key role within living cells. To enable their biological function reversible phase separation is mandatory: Under in vivo conditions, reversibly vital protein condensates such as liquid droplets and glassy solids are formed. These biological condensates are able to maintain their macroscopic shape for hours while exchanging components with the cytoplasm on the time scales of seconds [87]. Proteins can also reach an arrested irreversible state like as example amyloid fibers [87]. These irreversible amyloid fibers are known from diseases, for example they were found in alzheimer brains. Also the cataract diseases is caused by an aberrant phase transition in eye lens cells. This disease produces blindness by converting the clear cytoplasm into an opaque system containing solid aggregates [65].

3.2. Intermolecular interactions in protein solutions

The liquid-liquid phase behaviour and the crystal growth properties of biological macromolecules are controlled by interaction potentials on the length scale of Å to a few nm. The interparticle interaction energy V_{22} for protein solutions is given by [22]

$$V_{22}(r) = V_{HS}(r) + V_C(r) + V_{VdW}(r) + V_o(r) + V_a(r). \tag{3.1}$$

$V_{HS}(r)$ is the excluded-volume hard-sphere potential given by

$$V_{HS}(r) = \begin{cases} \infty & \text{for } r < \sigma \\ 0 & \text{for } r > \sigma \end{cases}, \tag{3.2}$$

where σ is the particle diameter and r is the center-to-center separation of the particles. The excluded-volume hard-sphere potential represents the fact that the particles are impenetrable and can not occupy the same space. A repulsive electrostatic contribution is given by the screened Coulomb potential [94],

$$V_C(r) = \frac{Z^2 e^2 \exp(-\kappa(r-\sigma))}{\epsilon r(1+\frac{1}{2}\kappa\sigma)^2}, \tag{3.3}$$

where Ze is the charge on the particle and ϵ is the dielectric constant of the medium. The range of the interaction is determined by the reciprocal Debye-Huckel screening length

$$\kappa = \frac{8\pi e^2 N_A I}{1000\epsilon k_B T}, \tag{3.4}$$

where N_A is Avogadro's number, I is the ionic strength of the solution, k_B is the Boltzmann constant and T is the temperature.

Attractive van-der-Waals dispersion forces are important to understand the structure of condensed macromolecules like proteins [50]. The van-der-Waals potential $V_{VdW}(r)$ is given by [94]

$$V_{VdW}(r) = \frac{-A}{12}\left(\frac{\sigma^2}{r^2-\sigma^2} + \frac{\sigma^2}{r^2} + 2\ln\left(\frac{r^2-\sigma^2}{r^2}\right)\right), \tag{3.5}$$

with the Hamaker constant A, which is determined by the material properties of the particles and the dispersion medium.

The osmotic attractive potential $V_o(r)$ occurs due to the excluded-volume effect of salt ions and the depletion mechanism in a protein-polymer mixture. The osmotic-attraction potential of Asakura and Oosawa describes the contribution of the excluded-volume effect of salt ions and is given by

$$V_{o,salt}(r) = \begin{cases} -\frac{4}{3}\pi d'^3(\rho_s k_B T)\left[1 - \frac{3r}{4\sigma'} + \frac{r^3}{16\sigma'^3}\right] & \text{for } r < 2\sigma' \\ 0 & \text{for } r > 2\sigma' \end{cases}, \tag{3.6}$$

where σ_h is the mean hydrated diameter in $\sigma' = \sigma + \sigma_h$ and ρ_s is the total ion concentration. By adding non-adsorbing polymers like polyethylene glycol (PEG) attractive depletion protein interactions due to an osmotic pressure described by the Asakura-Oosawa-Vrij

model occur [96]. The depletion potential in presence of polymers is given by [78]

$$V_{o,depl}(r) = \begin{cases} \infty & \text{for } r < \sigma \\ -\Pi_p V_{overlap} & \text{for } \sigma < r < 2r_g \\ 0 & \text{for } r > \sigma + 2r_g \end{cases} \tag{3.7}$$

with the osmotic pressure Π_p, the volume of the overlapping depletion zones between two particles at an intercentre separation of r and the radius of gyration of the polymer r_g. The square-well potential $V_a(r)$ describes the self-association of the proteins, which is a result of strong, short-range interactions, such as hydrogen bonds, hydrophobic bonds and ionic bonds and is given by

$$V_a(r) = \begin{cases} \epsilon_{AB} & \text{for } r_{AB} < r_c \\ 0 & \text{for } r_{AB} > r_c \end{cases}, \tag{3.8}$$

where ϵ_{AB} is the bonding potential, r_{AB} is the distance between bonding sites A and B and r_c is the cut-off distance of the bondings sites [22].

The attractive potentials $V_{VdW}(r)$ and $V_o(r)$ can be modelled in the form of a Yukawa potential [74]

$$V_Y = -J\left(\frac{\sigma}{r}\right)\exp\left(\frac{-(r-\sigma)}{d}\right), \tag{3.9}$$

where d is the range of the attractive potential and J is its depth at $r = \sigma$ in units of k_BT. The balance between the repulsive screened Coulomb potential $V_C(r)$ and the attractive potentials described by V_Y considering the excluded-volume hard-sphere potential $V_{HS}(r)$

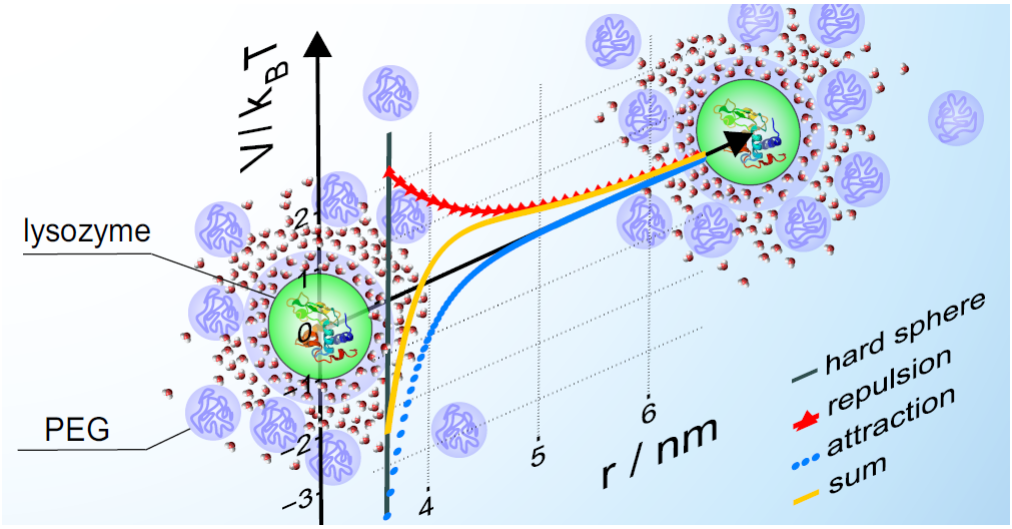

Figure 3.2.: The Derjaguin Landau Verwey Overbeek potential of two lysozyme proteins in solution and its contributions [55].

is described by the Derjaguin Landau Verwey Overbeek theory [26, 94]. The sum of the contributed potentials is given by

$$V_{DLVO}(r) = V_{HS}(r) + V_C(r) + V_Y. \tag{3.10}$$

and shown in Figure 3.2. If the attractive interactions are sufficient to exceed the repulsive forces, condensation processes like liquid-liquid phase separation are induced.

3.3. Thermodynamic fundamentals of phase transitions

If a mixed phase becomes unstable due to a change in thermodynamic conditions a phase transition occurs. The thermodynamic state of a system can be described by potentials, which are expressed by state variables characterizing the system. The potential free energy F is relevant for systems with the variables temperature T and volume V. In general the Gibbs-Duhem stability criterion is given by

$$\Delta U + p\Delta V - T\Delta S \geq 0, \tag{3.11}$$

where p is the pressure and ΔV, ΔS and ΔU are variations of V, the entropy S and the internal energy U from the equilibrium. For a system described by the variables T and V a stable phase is characterized by a minimum of F. To determine the stability of an equilibrium the difference in free energy

$$\Delta F = \delta F + \frac{1}{2}\delta^2 F + \frac{1}{3!}\delta^3 F + \frac{1}{4!}\delta^4 F + ... \tag{3.12}$$

in vicinity of the equilibrium must be considered. Here $\delta^2 F$, $\delta^3 F$ ... are the second-, third-order differentials of the free energy F. The exemplary phase diagram shown in Figure 3.3 shows three states depending on the thermodynamic conditions:

- The **mixed phase** is stable for $\delta F = 0$ and $\delta^2 F, \delta^3 F, ... > 0$.
- A **nucleation** occurs, if the conditions $\delta F = 0$ and $\delta^2 F > 0$ are satisfied, but some higher-ordered differentials are $\delta^3 F, ... < 0$. In this case the equilibrium is metastable. The threshold between a stable and metastable equilibrium is called binodal or coexistence line. $\delta^2 F = 0$ describes the metastability limit of the equilibrium.
- For $\delta^2 F < 0$ the equilibrium is unstable and the demixing process called **spinodal decomposition** occurs. The threshold between the metastable and unstable region inside the phase diagram shown in Figure 3.3 is called the spinodal line. The mixed system will become unstable and phase separated, if it is quenched beyond the spinodal line.

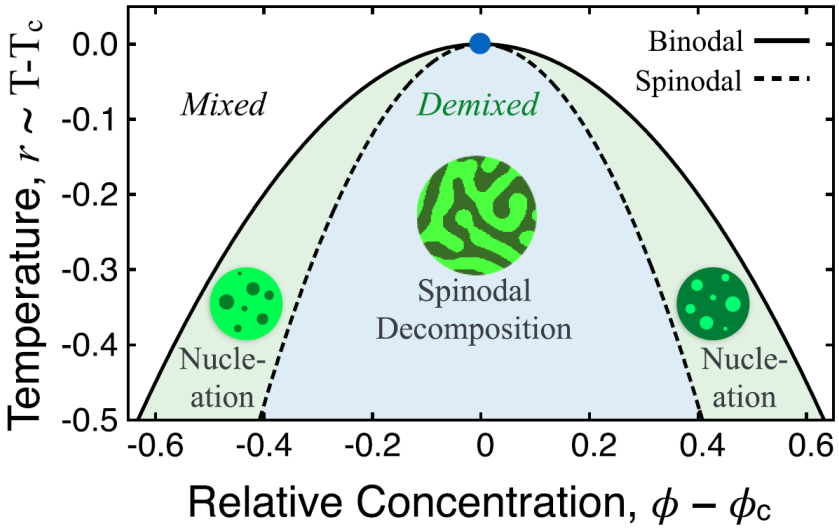

Figure 3.3.: Binary phase diagram with regions of mixed phase, nucleation and spinodal phase separation [9].

3.4. Spinodal decomposition and Cahn-Hilliard equation

The spinodal decomposition process is shown in Figure 3.4b and the nucleation process due to a quench between binodal and spinodal is shown in Figure 3.4a. For nucleation the occurring nuclei cause concentration discontinuities from the beginning of the process. In the case of spinodal decomposition the concentration becomes a local function $c(r)$ and varies continuously in space and time. The mathematical description of spinodal decomposition can be considered with a simple liquid-binary system A-B. The concentration c of constituent A is given by

$$c = \frac{n_A}{n_A + n_B}, \tag{3.13}$$

where n_A and n_B are the amounts of the constituents A and B, respectively. Initially the exemplary system is stable. The average concentration of component A inside the system AB is given by c_0. The free energy per unit of volume $f(c)$ around c_0 can be expanded by a series

$$f(c) = f(c_0) + (c - c_0)\left(\frac{\partial f}{\partial c}\right)_{c_0} + \frac{1}{2}(c - c_0)^2\left(\frac{\partial^2 f}{\partial c^2}\right)_{c_0} + \ldots \tag{3.14}$$

Using the approximation of relatively low amplitude fluctuations the total free energy F is given by

$$F = \int \left[f(c) + \frac{1}{2}K|\Delta c|^2\right] \mathrm{d}V, \tag{3.15}$$

where $K|\Delta c|^2$ with $K > 0$ is an energetic term which is a function of the concentration gradient in the system and can be considered as the equivalent of the energy to build up interfacial boundaries. Due to the definition of the average concentration $\int (c - c_0)\mathrm{d}V = 0$

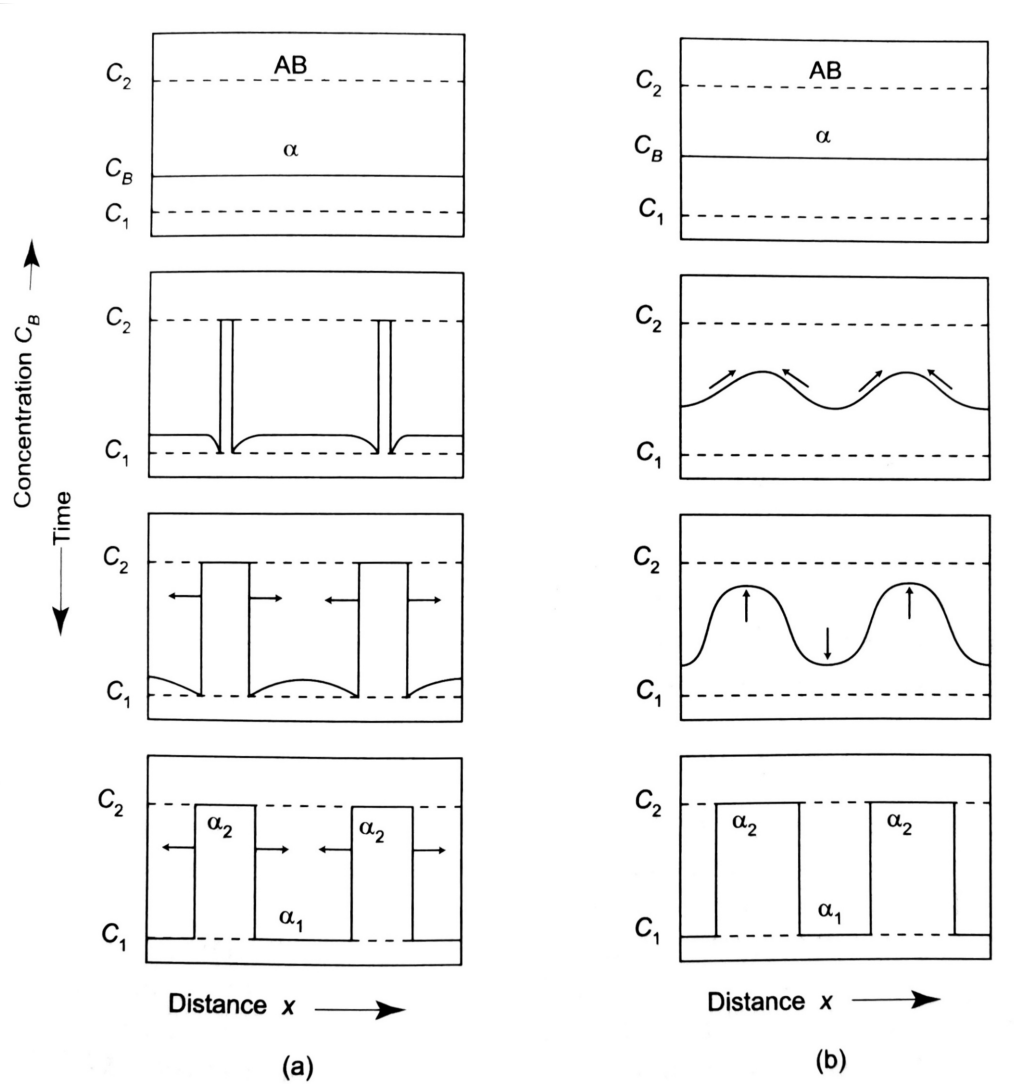

Figure 3.4.: (a) Nucleation and (b) spinodal decomposition: The local change of the concentration C of constituent A in a binary mixture A-B. [76].

applies and the first-order term in eq. (3.14) is eliminated. Terms higher than second order are neglected. The difference in free energy ΔF between the homogenous state and the inhomogenous state can be written as

$$\Delta F = \int \left[\frac{1}{2} (c - c_0)^2 \left(\frac{\partial^2 f}{\partial c^2} \right)_{c_0} + \frac{1}{2} K |\Delta c|^2 \right] \mathrm{d}V. \tag{3.16}$$

In the case of $\Delta F < 0$ the demixed system becomes stable and the spinodal decomposition occurs. The probability of a concentration fluctuation δc causing the spinodal decomposition is proportional to $\exp\left(-\frac{\Delta F}{kT}\right)$. The concentration fluctuations are changing in time

and can be expanded in the Fourier transformation

$$\delta c\left(\vec{r},t\right)=\int\delta c\left(\vec{k},t\right)\exp(-\mathrm{i}\vec{k}\vec{r})\ \mathrm{d}\vec{k}. \tag{3.17}$$

Under the assumption of an one-dimensional material with fluctuations $\delta c_K = A\cos(kx)$ with the same amplitude A, ΔF can be written as

$$\Delta F=\int\Delta F_{\vec{k}}\ \mathrm{d}\vec{k}. \tag{3.18}$$

An integration of eq. (3.16) over the entire volume of the material leads to

$$\Delta F_K=\frac{1}{4}VA_2\left[(c-c_0)^2\left(\frac{\partial^2 f}{\partial c^2}\right)_{c_0}+Kk^2\right]. \tag{3.19}$$

Fluctuations with a wavelength λ larger than a critical wavelength λ_c

$$\lambda_c=\frac{2\pi}{k_c} \tag{3.20}$$

lead to $\Delta F_k < 0$ and the spinodal decomposition occurs. The critical wavevector k_c is given by

$$k_c=\sqrt{-\frac{1}{K}\left(\frac{\partial^2 f}{\partial c^2}\right)_{c_0}}. \tag{3.21}$$

In the opposite case the occurrence of fluctuations with a wavelength λ smaller than a critical wavelength λ_c increase $\Delta F_k > 0$ and produce homogeneity within the thermodynamic unstable region $\left(\frac{\partial^2 f}{\partial c}\right) < 0$.
John Werner Cahn calculated a diffusion equation which characterises the kinetics of a binary mixture phase transition. The thermodynamic process is forced by a concentration current

$$\vec{J}=-M_0\nabla\mu, \tag{3.22}$$

where M_0 is a constant transfer coefficient and $\mu=\frac{\partial F}{\partial c}$ is the chemical potential of the mixture. The concentration currents for a binary system are defined as

$$\vec{J_A}=-\vec{J_B}=-M_0\nabla(\mu_A-\mu_B). \tag{3.23}$$

In the case of no chemical reactions the diffusion equation is given by

$$\frac{\partial c\left(\vec{r},t\right)}{\partial t}+\nabla\vec{J}=0, \tag{3.24}$$

where $c(\vec{r},t)$ is a variable describing an inhomogenous material. With $M = \frac{M_0}{n_a+n_b}$ and $\mu_A - \mu_B = \frac{1}{n_a+n_b}\frac{\partial f}{\partial c}$ eq. (3.24) can be written as

$$\frac{\partial c(\vec{r},t)}{\partial t} = M\nabla^2\frac{\partial f}{\partial c}. \tag{3.25}$$

The functional derivative of F with respect to c in 3.25 is given by

$$\delta F = \int \left[\frac{\partial f}{\partial c}\delta c + \frac{1}{2}K\nabla_r\delta c\nabla_r c + \frac{1}{2}K\nabla_r c\nabla_r\delta c\right] d\vec{r}. \tag{3.26}$$

A partial integration $\left(\int \nabla_r\delta c\nabla_r c = \delta c\nabla_r c - \int \delta c\nabla^2 c\right)$ and the assumption $\nabla_r c = 0$ on the integration surface leads to

$$\delta F = \int \left[\frac{\partial f}{\partial c} - K\nabla^2 c\right]\delta c d\vec{r} \tag{3.27}$$

and

$$\frac{\partial F}{\partial c} = \frac{\partial f}{\partial c} - K\nabla^2 c. \tag{3.28}$$

By inserting eq. (3.28) into eq. (3.24), finally the time-dependent evolution of the concentration can be described by a nonlinear diffusion equation

$$\frac{\partial\delta c(\vec{r},t)}{\partial t} = M\nabla^2\left[\frac{\partial f}{\partial c} - K\nabla^2 c(\vec{r},t)\right] \tag{3.29}$$

called Cahn-Hilliard equation [12, 17]. The Cahn-Hilliard equation can be linearized under the assumption of relatively low amplitude fluctuations

$$\frac{\partial\delta c(\vec{r},t)}{\partial t} = M\nabla^2\left[\left(\frac{\partial^2 f}{\partial c^2}\right)_{c_0} - K\nabla^2\right]\partial\delta c(\vec{r},t). \tag{3.30}$$

The Cahn-Hilliard equation can be solved using the Fourier transform eq. (3.17) and the assumption of an exponential relaxation mechanism of fluctuations

$$\delta c\left(\vec{k},t\right) = \delta c\left(\vec{k},0\right)\exp\left(-\omega_k t\right). \tag{3.31}$$

The damping coefficient ω_k can be obtained by inserting eq. (3.17) and eq. (3.31) into the linearized Cahn-Hilliard equation. Using eq. (3.21) ω_k can be written as

$$\omega_k = MKk^2\left(k^2 - k_c^2\right). \tag{3.32}$$

In the thermodynamically unstable region inside the phase diagram applies $\omega_k < 0$. In this case the concentration fluctuations are not damped. Thus they increase with time and cause spinodal decomposition.

3.5. Arrested State and Glass Transition

The properties of a LLPS system can change due to an occurrence of a glass transition. An arrested phase separation can be observed during deep quenches below the biondal of a LLPS system due to strong attractive depletion interactions between the particles [63, 66]. Sappelt et al. [82] reported for a binary liquid mixture, that a glass transition implies a decrease of the coefficient of mobility which depend on the concentration and the temperature. In this case all transport and relaxations rates decrease rapidly over several orders of magnitude [51].
Figure 3.5a shows the state diagram of a LLPS in a lysozyme solution, where the region below the binodal line can be separated into three regions. Thereby an arrested state can be characterized as a gel [102] or glass state depending on the precise quench pathway [20]. For shallow quenches in area I classical spinodal decomposition including complete demixing occurs. In area I the growth of the characteristic length follow the power law

$$\xi \approx t^{\frac{1}{3}}. \tag{3.33}$$

Outside area I the growth kinetics significantly slow down and the power law in eq. (3.33) is not valid anymore. This effect increases with the quench depth below the binodal as shown for the IgG-PEG model system (see section 3.6) in Figure 3.6. The local arrest line (filled circles in Figure 3.5a) separates region II where gels are formed due to an arrested spiondal decomposition and region III where homogenous arrested glasses are build [37].

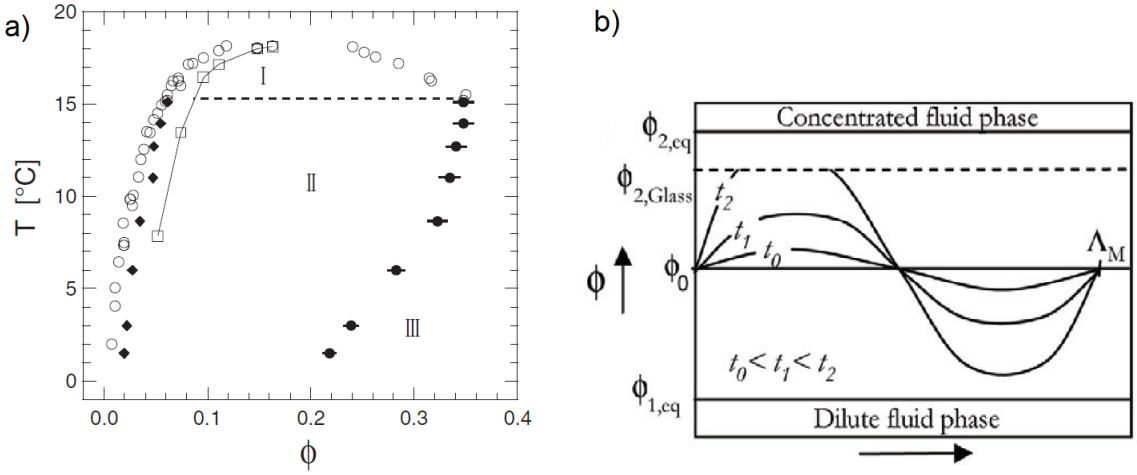

Figure 3.5.: a) State diagram of aqueous lysozyme solutions showing regions of crystal formation [18].
b) Schematically description of the evolution of density fluctuations as a function of time [37].

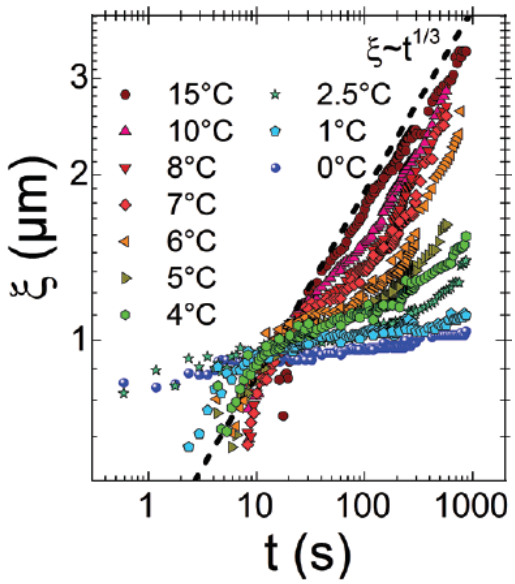

Figure 3.6.: Growth of IgG droplets characteristic length depending on quench temperature [23].

The **gel state** can be characterized by the following properties [46, 76]:

- A gel constitutes a homogeneous phase with a solid solute component dissolved in a liquid phase component.
- The gel behaves like a solid under the effect of microscopic forces.
- The entire volume of the gel phase is occupied by the dissolved constituent and the solvent which are interconnected in the form of a three-dimensional network.

The **glass state** can be described as a supercooled liquid where the fluctuations are frozen. Reaching the glass line the viscosity of the liquid increases significantly and a noncrystalline solid with the following properties is build [76]:

- A long-range order does not exist in a glass.
- Flexible bond angles occur, which is not allowed in the crystal.

In Figure 3.5b the evolution of the density fluctuations of wavelength Λ around the initial volume fraction ϕ_0 during the **glass transition** is shown. The phase separation process stops before the dense phase reaches the equilibrium value $\phi_{2,eq}$ and the system becomes arrested [37] in a glassy state at

$$\phi_2 = \phi_{2,glass} < \phi_{2,eq}. \tag{3.34}$$

For arrested states a typical two-step relaxation in correlation functions was reported by Zaccarelli [102]:

An initial microscopic β-relaxation indicating the particle vibration inside of a cage formed by their nearest neighbours in the network followed by a plateau and a final α-relaxation can be observed. The α-relaxation corresponds to the process when the particle is able to escape from its initial configuration by leaving the cage. The height of the plateau between α- and β-relaxation is defined as the non-ergodicity parameter.
For a glass transition the plateau becomes longer upon increasing volume fraction ϕ and all wavevectors show a non-ergodicity parameter simultaneously within numerical resolution. During a gel transition the non-ergodicity parameter becomes finite in a continuous way. In this case at fixed ϕ the non-ergodicity parameter shows a strong dependence increasing with q [102].

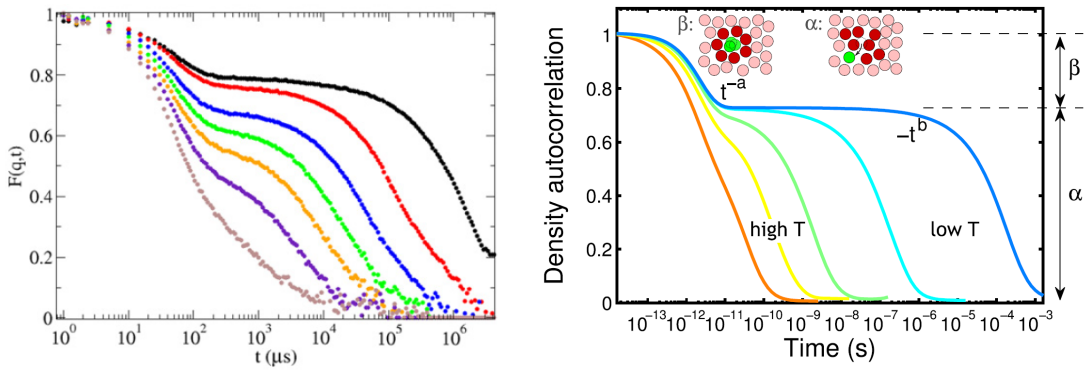

(a) (b)

Figure 3.7.: (a) Gel transition: Non-ergodicity parameter is changing continuously with increasing volume fraction [85].
(b) Slower alpha and faster beta relaxation processes in glasses [45].

3.6. IgG-PEG model system

Antibodies are a very important type of proteins in the human body, which are part of the blood plasma. The most abundant mammalian plasma protein is albumin, which is responsible for the molecular transport in the body, followed by immunoglobulins [29]. Immunoglobulins play a key role in the immune system [57] and can be divided into α_1-globulin, α_2-globulin, β-globulin and γ-globulin (IgG). IgG is used in drugs against human diseases like autoimmune diseases and kinds of cancer [97].

In Figure 3.8 the conformation of IgG is shown. IgG is a complex folded Y-shaped protein and consists of antigen-binding domains (Fab) and crystallizable domains (Fc) linked by disulfide bridges in the molecular centre. The IgG monomer molecular mass is $140 - 170\,\mathrm{kDa}$ and its radius of gyration is reported with $4.9 - 6\,\mathrm{nm}$ [56]. Its maximum intramolecular distance is $18.4\,\mathrm{nm}$ [24]. The biological functions of IgG are defined by its specific amino acid sequence in Fab [97].

In general IgG is highly soluble at physiological conditions, but there are also amino acid sequences existing which are causing an increase in the attractive interaction of IgG molecules. Due to this attractive interactions IgG condensates can formed due to liquid-liquid phase separation. IgG condensation is connected to some human diseases and changes in biopharmaceutical formulations [97].

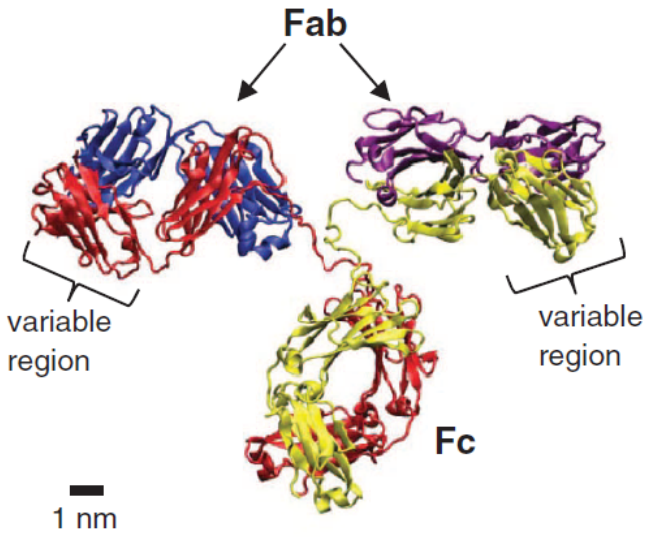

Figure 3.8.: X-ray crystallographic structure of an IgG molecule [44, 97].

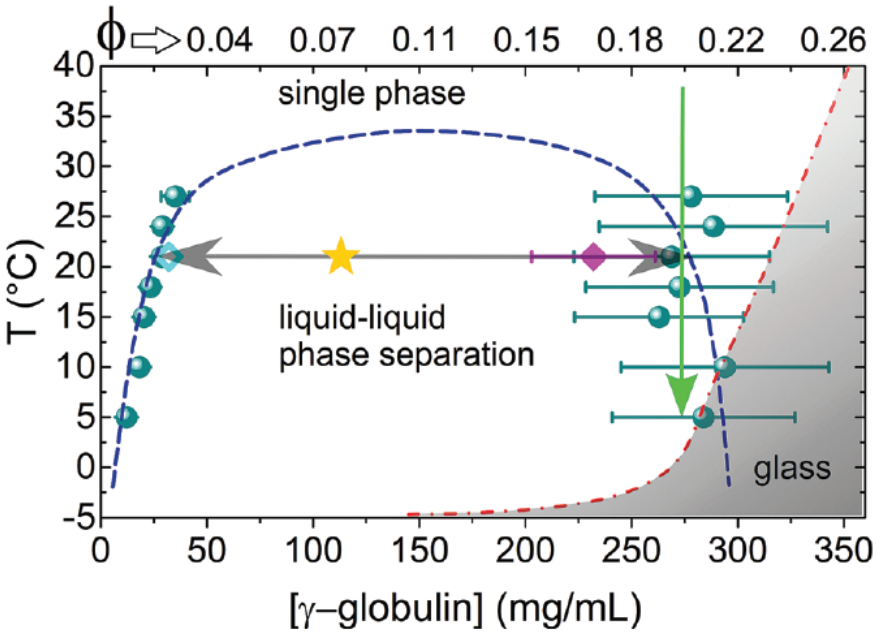

Figure 3.9.: Binodal of the LLPS for a parent solution of 110 $\frac{\text{mg}}{\text{mL}}$ IgG and 10% (w/v) PEG 1000 [23].

In this thesis a bovine IgG in vitro phase transition in presence of polyethylene glycol (PEG) and NaCl is investigated. The kinetics of this IgG-PEG model system are well understood [23]. The binodal phase diagram of the liquid-liquid phase separation for a parent solution with 110 $\frac{\text{mg}}{\text{mL}}$ bovine IgG and 10% (w/v) PEG 1000 is shown in Figure 3.9. The parent solution undergoes a first phase separation at 21 °C marked by the star in Figure 3.9. The green arrow shows a typical quenching process of the dense phase. The model system shows a liquid-liquid phase separation with an upper critical solution temperature. For deep quenches in the phase diagram the sample dynamics become arrested [18, 37, 38].

The kinetics of spinodal decomposition were investigated using ultra-small angle X-ray scattering (USAXS). Figure 3.10 shows coarsening kinetics for a quench from 38 to 10 °C. The growth of IgG protein domains during phase separation as described by Cahn-Hilliard theory is related to an increase of a peak in the structure factor $S(q)$. Further the peak position q_{max} is shifting to smaller scattering vectors, which is related to an increase of the characteristic length of the IgG droplets via

$$\xi = \frac{2\pi}{q_{max}}. \tag{3.35}$$

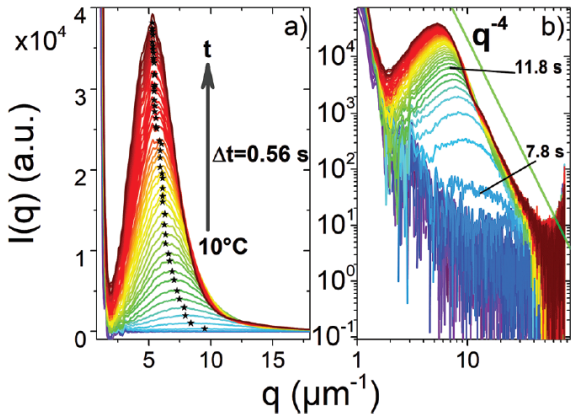

Figure 3.10.: IgG-PEG USAXS profiles show the phase separation at early times ($t \leq 36\,\mathrm{s}$) [23].

The behaviour of this coarsening kinetics differs with the quench temperature T_C. Figure 3.6 shows the growth of the characteristic length ξ for different quench temperatures T_C. For a shallow quench to for example 15 °C the growth kinetics follow the power law

$$\xi \approx t^{\frac{1}{3}} \tag{3.36}$$

known from diffusive growth. Deeper quenches beyond the glass line cause a slowdown of kinetics due to reaching the arrested state [23].

4. Experimental setup and sample environment

The experimental realization of the experiments is presented in this chapter. X-ray scattering experiments were conducted at the 3rd generation synchrotron Positron-Elektron-Tandem-Ring-Anlage III (PETRA III) at the Deutsches Elektronen-Synchrotron (DESY) in Hamburg. First, an introduction to the synchrotron PETRA III as the X-ray radiation source for the experiments is given in Section 4.1. The P10 Coherence Applications Beamline at PETRA III including the USAXS and the SAXS setup are described in Section 4.2. Later the data treatment using an Eiger 4M detector and the measurement protocol to investigate the IgG sample system will be presented.

4.1. PETRA III synchrotron at DESY

The PETRA III synchrotron is a circular accelerator, also called storage ring, where electrons are accelerated to an energy of 6 GeV. The electrons are forced on a circular trajectory by bending magnets. Synchrotron radiation is emitted in this process due to electrons that are accelerated lateral to their relativistic velocity.

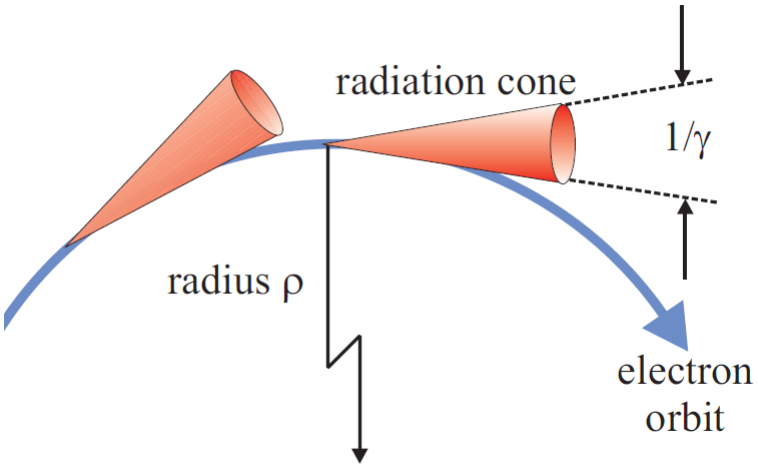

Figure 4.1.: Synchrotron radiation source: A relativistic electron is moving in a circular trajectory. The radiation is emitted in a cone with an opening angle $\frac{1}{\gamma}$ around the instantaneous velocity [2].

Figure 4.1 shows a sketch of a synchrotron radiation source, which is conically emitted in forward direction caused by the Lorentz transform for relativistic motion. The X-ray cone opening angle γ is proportional to the inverse Lorentz factor

$$\frac{1}{\gamma} = \frac{1}{\sqrt{1 - \frac{v_e^2}{c^2}}} \tag{4.1}$$

with the electron velocity v_e and the speed of light c.
The coherent flux of an X-ray radiation source is defined as

$$F_c = B\frac{\lambda^2}{4}, \tag{4.2}$$

where λ is the X-ray wavelength. The source brilliance B of PETRA III is given by

$$B = \frac{F_{ph}}{4\pi^2 \epsilon_x \epsilon_y} \approx 10^{21} \frac{\text{Photons}}{\text{s mm}^2 \text{ mrad}^2 \text{ 0.1\% BW}}, \tag{4.3}$$

where F_{ph} is the photon flux and ϵ_x and ϵ_y are the emittance in horizontal and vertical beam direction, respectively. At PETRA III undulators are inserted to increase the photon flux. An undulator forces the electron bunches to execute oscillations in the horizontal plane as they traverse through. The undulator is composed of arrays of permanent magnets that produce alternating magnetic fields with an undulator spatial period $\lambda_u = 2.9\,\text{cm}$. A scheme of an undulator is shown in Figure 4.2. The fundamental wavelength emitted by an undulator is given by

$$\lambda = \frac{\lambda_u}{2\gamma^2}\left(1 + \frac{K^2}{2}\right) = 2.194\,\text{Å}, \tag{4.4}$$

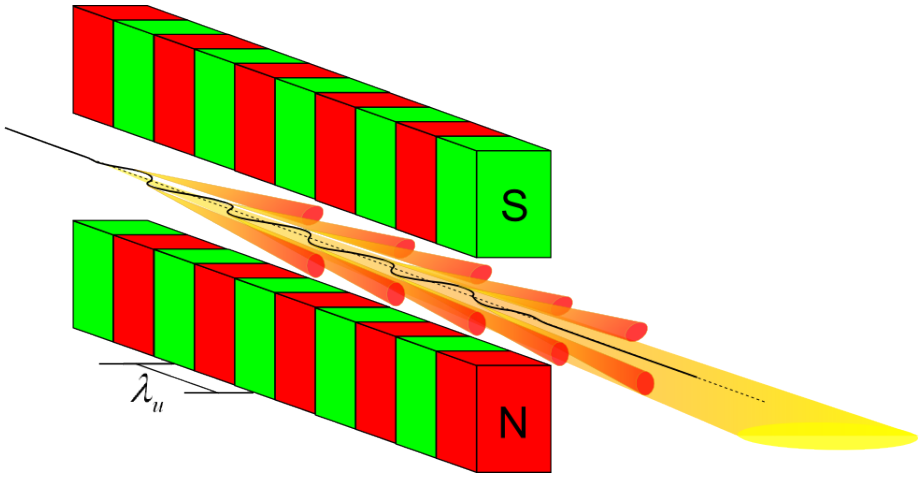

Figure 4.2.: Scheme of an undulator: Permanent magnets are arranged with a spatial period λ_u and alternating magnetic field direction [83].

where K denotes the undulator parameter, which is defined as

$$K = \frac{\lambda_u e B_0}{2\pi m_e c} = 2.0154 \cdot 10^{-10}\,\mathrm{m} \tag{4.5}$$

in dependence of the maximum magnetic field $B_0 = 0.81\,\mathrm{T}$ in the undulator. Here m_e is the electron mass and e is the electron charge [2].

4.2. The P10 Coherence Applications Beamline

The X-ray scattering experiments were conducted at the P10 Coherence Applications Beamline at PETRA III. The 5 m long undulator named U29 provides the synchrotron radiation at the beamline with a brilliance of $B = 4 \cdot 10^{20}\,\frac{\mathrm{Photons}}{\mathrm{s\ mm^2\ mrad^2\ 0.1\%\ BW}}$ at $E_{ph} = 8\,\mathrm{keV}$. P10 is divided into three hutches, one optics hutch and two experimental hutches. In Figure 4.3 the schematic layout of beamline P10 and the most important components are shown. At P10 the X-ray beam has to pass the optics hutch first where the energy is defined by a Si(111) high heat load monochromator (HHM). The monochromator is able to reduce the bandwidth to

$$\frac{\Delta\lambda}{\lambda} \approx 10^{-4}. \tag{4.6}$$

In order to suppress higher harmonics of the undulator spectrum two flat X-ray mirrors (M1,M2) are installed. Inside of the first experimental hutch (EH1) a 10 Hz fast shutter (FS) is mounted. The sample chamber was installed in EH1 (USAXS) or EH2 (S), respectively. The guard slits (G1,G2) define the beam size on the sample and are able to reduce parasitic scattering. The protein samples were mounted inside of a Linkam heating stage, which is able to change the sample temperature with a quench rate up to 150 $\frac{\mathrm{K}}{\mathrm{min}}$. To heat up the sample Linkam stage uses an electronic heating. The cooling function is provided by a liquid nitrogen connection. The Linkam stage can be moved with the usage of motors in all three spatial directions and contains a slot for sample capillaries with a diameter of 1.5 mm. The X-ray speckle pattern data were collected using an Eiger 4M detector (D) in the second experimental hutch (EH2) [28]. A beamstop was installed to block the direct beam to prevent detector damage due to overexposure.

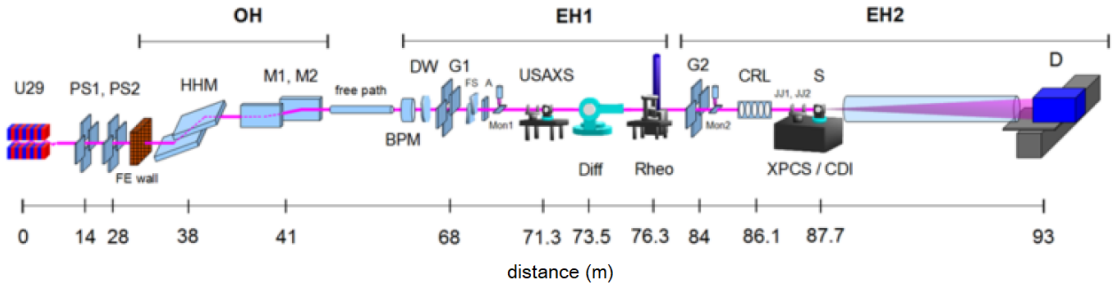

Figure 4.3.: Schematic layout of the P10 Coherence Applications Beamline. The X-ray beam is emitted by the undulator (U29) passes the components, which are labeled as follows with: undualtor (U29), monochromator (HMM), flat X-ray mirrors (M1,M2), guard slits (G1,G2), fast shutter (FS), sample chamber in USAXS setup (USAXS), sample chamber in SAXS setup (S) and detector (D) [28].

4.2.1. The USAXS setup

In the USAXS setup the sample was mounted inside of EH1. The incident coherent flux was $F_c = 10^{11}\,\frac{\text{photons}}{\text{s}}$. The distance between sample and the detector was 21.2 m. All measurements in the USAXS setup were performed at photon energy $E = 8.54\,\text{keV}$. The accessible q range was

$$0.004\,\text{nm}^{-1} < q < 0.05\,\text{nm}^{-1}, \tag{4.7}$$

limited by a beamstop at low q and the flight tube at large q values. Using the USAXS setup it was feasible to measure with a large beamsize of $100 \times 100\,\mu\text{m}^2$. Thus, the photon density on the sample was $10^{19}\,\frac{\text{photons}}{\text{m}^2\text{s}}$. Different numbers N_{att} of 25 μm thin silicon wavers were installed as absorbers to attenuate the incident beam. The transmission values T can be found in table 4.1. The USAXS setup is shown in Figure 4.4.

N_{att}	$d(\mu\text{m})$	$T(\%)$
0	0	100
2	50	55.2
4	100	30.5
6	150	16.8
8	200	9.3
9	225	6.9
12	300	2.8

Table 4.1.: Silicon attenuator transmission values for $E = 8.54\,\text{keV}$ in dependence of the attenuator thickness d.

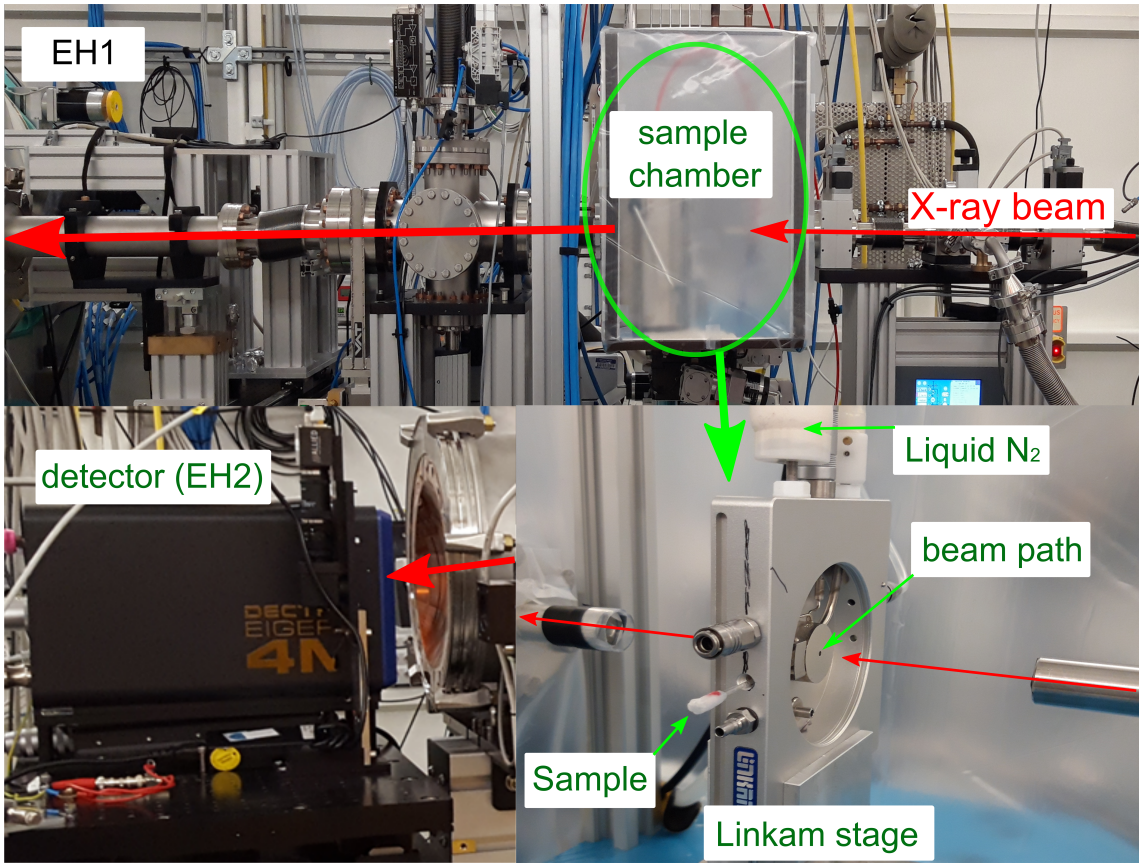

Figure 4.4.: USAXS setup at P10 Coherence Applications Beamline.
top: sample chamber in the first experimental hutch.
bottom left: EIGER 4M detector installed at the end of the 21 m evacuated flight tube in the second experimental hutch.
botton right: Linkam stage with liquid nitrogen connection and sample slot inside the sample chamber.

4.2.2. The SAXS setup

The measurements in SAXS setup were performed using a photon energy of $E = 13\,\mathrm{keV}$ and an incident coherent flux of $F_c = 4 \cdot 10^{10}\,\frac{\mathrm{photons}}{\mathrm{s}}$. In SAXS setup the sample to detector distance was 5.05 m and the accessible q range was

$$0.03\,\mathrm{nm}^{-1} < q < 1.5\,\mathrm{nm}^{-1}. \tag{4.8}$$

A beamsize of $30 \times 30\,\mu\mathrm{m}^2$ was used, which yields to a photon density on the sample of $4.44 \cdot 10^{19}\,\frac{\mathrm{photons}}{\mathrm{m}^2\mathrm{s}}$. Different numbers N_{att} of silver foils were installed to attenuate the incident beam. The transmission values T are shown in table 4.2. Figure 4.4 shows the SAXS setup.

N_{att}	$d(\mu\mathrm{m})$	$T(\%)$
0	0	100
1	25	48
2	50	23
4	100	11
5	125	5.5
6	150	1.2

Table 4.2.: Silver attenuator transmission values for $E = 13\,\mathrm{keV}$ in dependence of the attenuator thickness d.

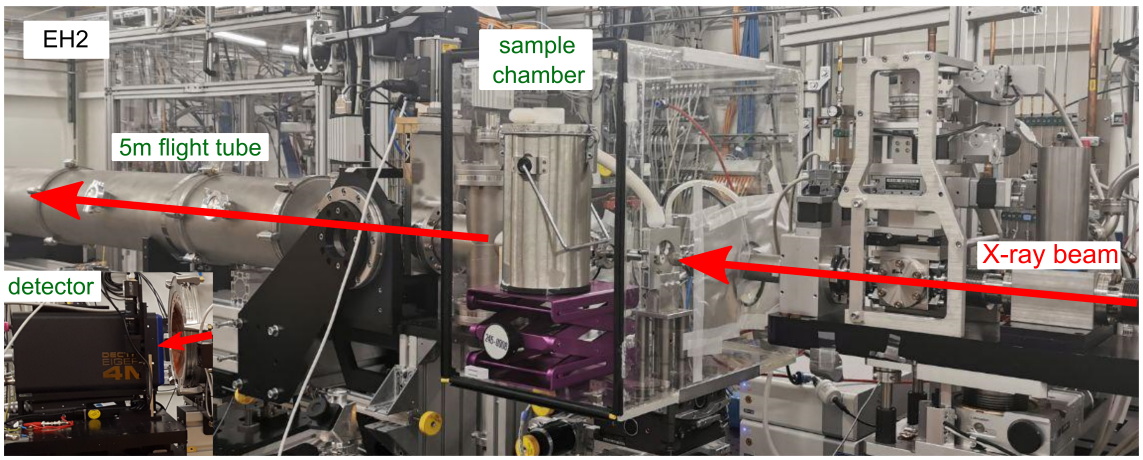

Figure 4.5.: SAXS setup at P10 Coherence Applications Beamline. The setup within the sample chamber corresponds to the USAXS setup.

4.3. Data treatment using Eiger 4M detector

An EIGER 4M detector from Dectris was used to collect the X-ray scattering series [54]. The pixel size of the detector is $75\,\mu\text{m} \times 75\,\mu\text{m}$ and the fastest frequency to collect images is 750 kHz. The horizontal pixel number is 2070 and the vertical pixel number is 2160. The EIGER 4M detector is able to record X-ray scattering series with the parameters number of images N_{im} and single image exposure time t_{exp}. Optionally a shutter delay time t_{fs} between the images can be inserted. During this delay time the fast shutter is closed. Due to the fastest frequency of the fast shutter is 10 Hz, the smallest shutter delay time feasible is 0.1 s. The readout time of the EIGER 4M is $t_r = 10\,\mu\text{s}$. The delay time between the images is given by

$$t_{delay} = t_{exp} + t_{fs} + t_r. \tag{4.9}$$

The values for t_{exp} and t_{fs} are presented in section 4.5. The total measurement series time,

$$T_{measurement} = t_{delay} \cdot N_{im}. \tag{4.10}$$

defines the timescale of dynamics, which can be analysed.

4.4. IgG sample preparation

To prepare the protein samples Bovine γ-globulin (IgG) with an indicated purity of $\geq$ 99% (product number: SRE0011) was purchased by Sigma-Aldrich and used as received. An IgG stock solution was prepared by dissolving IgG in ultrapure degassed water ($18.2\,\text{M}\Omega \cdot \text{cm}$, Merck Millipore Water Purification System) in a buffer, which composes 20 mM HEPES (empirical formula $C_8H_{18}N_2O_4S$, pH = 7.0) purchased by Roth (HN78) and 2 mM NaN3 purchased by Sigma-Aldrich (S8032). The exact IgG concentration of the stock solution was determined by UV absorption spectroscopy at a UV wavelength of



Figure 4.6.: 200 $\frac{\text{mg}}{\text{ml}}$ IgG, 9% w/v PEG 1000, 150 mM NaCl dense phase sample capillary.

280 nm using a Cary 50 UV-Vis spectrophotometer. Afterwards the parent solution containing 200 $\frac{\text{mg}}{\text{ml}}$ IgG, 9% w/v PEG 1000 and 150 mM NaCl was produced [40]. PEG 1000 (81188) purchased by Sigma-Aldrich and NaCl (106404) purchased by Merck were used as received. After equilibrating at 21 °C for 24 hours the parent solution was briefly centrifuged. A phase separation into a dilute and dense phase became visible [40]. The phase diagram of this model system was shown in section 3.6 in Figure 3.9. The dense phase was filled inside of 1.5 mm diameter quartz glass capillaries and measured by USAXS(-XPCS) and SAXS(-XPCS). The IgG model system sample is shown in Figure 4.6.

4.5. IgG sample measurement protocol

The IgG sample capillary was mounted inside of the sample holder of the Linkam stage (Figure 4.4). The Linkam stage is used to control the sample temperature. The experiment started in both the USAXS and the SAXS setup with the determination of the sample radiation damage threshold. Therefore the sample temperature was set to 37 °C, where the sample shows no phase separation (Figure 3.9). The thresholds of maximum photon densities and X-ray exposure times were defined by studying X-ray induced changes to the static SAXS patterns of the homogeneous sample as described in section 2.6. Therefore X-ray scattering series with different numbers of images and different attenuators were collected. The results are presented in section 5.2. After determining these radiation damage threshold an XPCS measurement protocol in compliance with the maximum tolerable dose was established. Both, the USAXS and SAXS measurements were collected at sample spots around 1 cm from the bottom of the capillary to avoid avalanche events caused by elastic rearrangements inside the sample.

4.5.1. USAXS-XPCS measurements

T_q(°C)	N_{im}	t_{exp}(s)	t_{fs}(s)	N_{att}	D(kGy)
15	4000	0.02	0.1	9	5.11
12	4000	0.02	0.1	9	5.11
10	4000	0.02	0.1	9	5.11
8	4000	0.02	0.1	9	5.11
6	4000	0.02	0.1	9	5.11
4	4000	0.02	0.1	9	5.11

Table 4.3.: USAXS-XPCS measurements

The aim of the USAXS-XPCS measurements was to understand the dynamics during the spinodal phase transition of the IgG model systems on macromolecular length scales. The IgG model system sample was measured during quenches from the homogeneous phase at 37 °C to different temperatures below the binodal line. The quench temperatures T_q

were 15 °C, 12 °C, 10 °C, 8 °C, 6 °C and 4 °C. Before the measurements were started the sample was equilibrated at 37 °C for 600 s. Each measurement was recorded at a different fresh sample spot. An overview of the USAXS-XPCS measurements is given by table 4.3. The USAXS-XPCS results are presented in section 5.3.

4.5.2. SAXS-XPCS measurements

In SAXS setup the aim was to measure dynamics on the single protein length scale. The main challenge was that the scattering intensity at large q values ($1\,\mathrm{nm}^{-1}$) drops by four orders of magnitude compared to the intensity of the q values, which were observed by the USAXS measurements. Therefore, it was not feasible to extract an analysable correlation function from one single X-ray scattering series. Hence, the number of repetitions N_{rep} was increased to gain an acceptable SNR and the correlation functions of several series were merged. Every single repetition was recorded at a different fresh sample spot. In SAXS setup the quench temperature T_q was $-5\,°\mathrm{C}$. The measurements were started after a waiting time of 600 s after the quenching process was finished to be sure that the sample reached the arrested state. Table 4.4 shows the parameter of the collected SAXS-XPCS measurements. The SAXS-XPCS results are presented in section 5.4.

T_q(°C)	N_{im}	t_{exp}(s)	t_{fs}(s)	N_{rep}	N_{att}	D(kGy)
-5	800	0.005	0	120	0	10.23
-5	600	0.1	0.4	42	4	8.43

Table 4.4.: SAXS-XPCS measurements

5. Data Analysis and Discussion

In this chapter the analysis of X-ray scattering data is presented. First, in section 5.1 the preparation of the raw data for the analysis is presented. In section 5.2 a radiation damage threshold dose is defined by analysing the static signal for both, the USAXS and the SAXS measurements. In section 5.3 the USAXS measurements are analysed to investigate the kinetics and dynamics of the IgG model system on micrometer length scales. Finally in section 5.4 the SAXS measurements are presented to obtain dynamical information on the length scale of single proteins. The SAXS scattering intensity and the two-time correlation functions were extracted from the data using the python software package Xana [79] written by Mario Reiser. Further analysis was done using MATLAB [67].

5.1. Raw data preparation

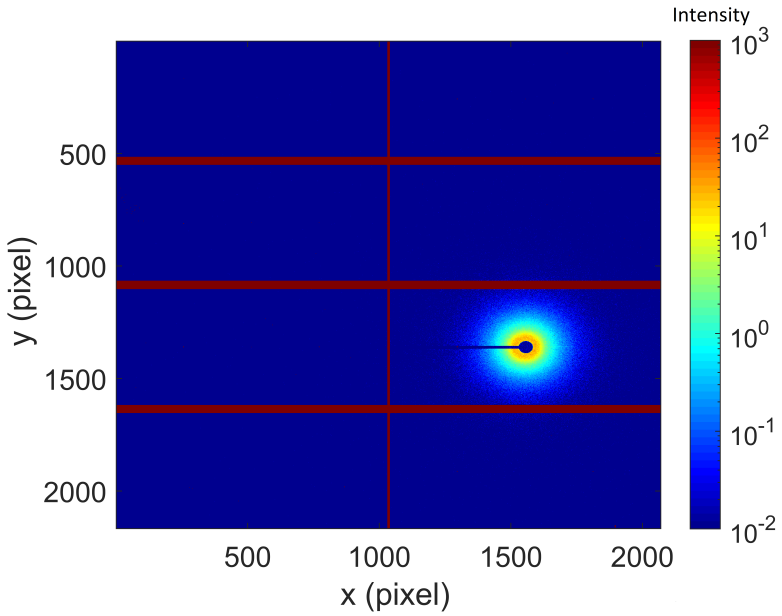

Figure 5.1.: Full scattering pattern recorded by the Eiger 4M detector. The image shows the average of hundred single exposures of 0.02 s during a quench of the IgG model system from 37 °C to $T_q = 6$ °C.

The Eiger 4M detector acquires series of raw X-ray scattering images, which contain scattering by the protein sample as well as scattering caused by the setup. Figure 5.1 shows a 2D scattering pattern recorded in USAXS setup by the Eiger 4M detector during an XPCS measurement of the IgG model system. The Eiger 4M detector consists of eight single detector modules which becomes visible in Figure 5.1. In Figure 5.2 the detector section containing the beam centre is shown in detail. On the right side of the image a parasitic streak caused by some setup component is visible. The beam centre is covered by the beamstop up to values corresponding to a scattering vector of $q = 0.004\,\mathrm{nm}^{-1}$. Before analysing the raw data, the detector area containing signals from another origin than the scattering of the protein sample must be set to zero. Therefore, a mask is created which eliminates the signal from the beamstop as well as the area between the detector modules and parasitic scattering. In addition, the detector has some hot pixels that have also been masked. In Figure 5.3 the scattering pattern is shown after using the mask.

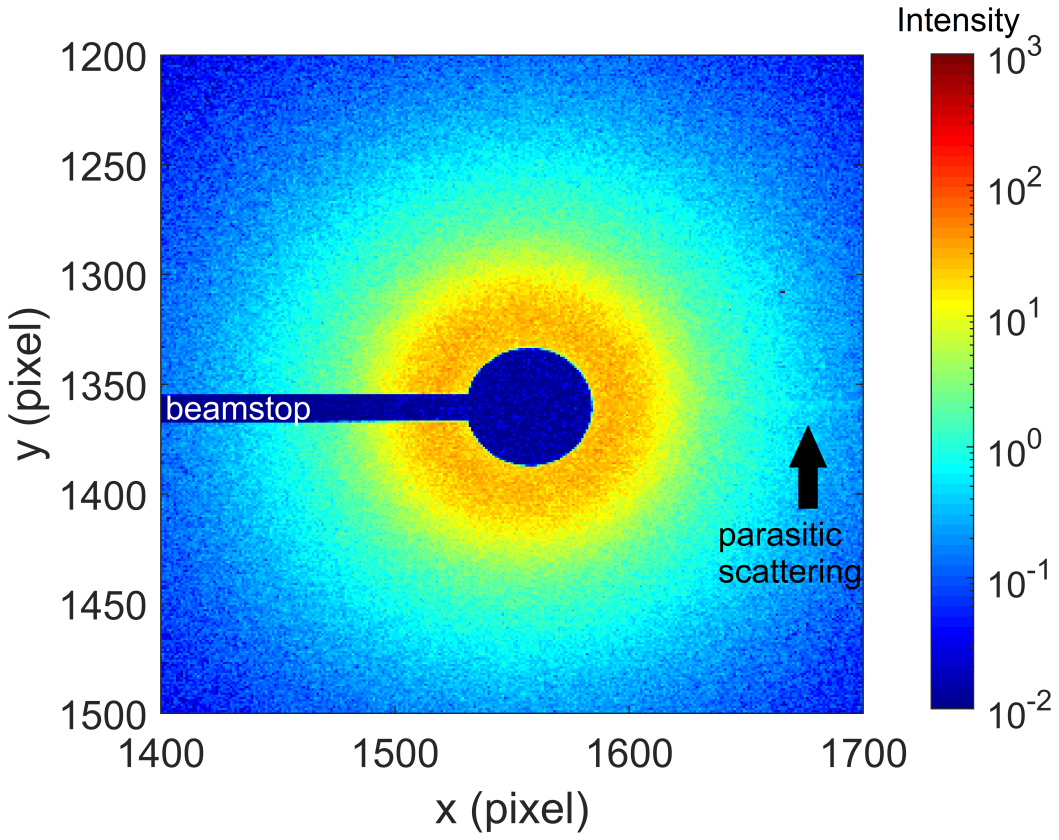

Figure 5.2.: Detail of the scattering pattern shown in Figure 5.1.

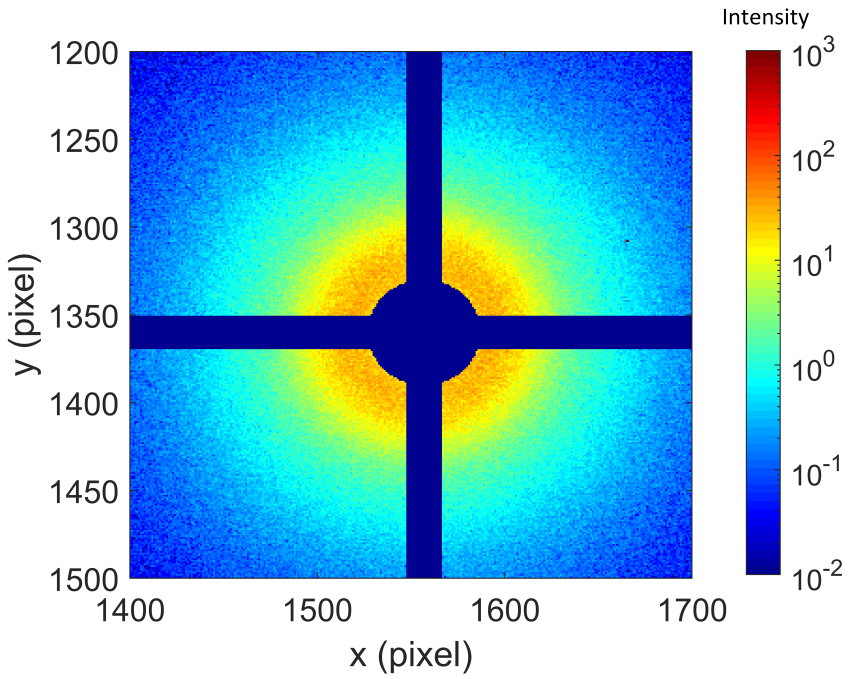

Figure 5.3.: Scattering pattern after applying the mask.

In Figure 5.4a a two-time correlation recorded in the middle of the capillary is shown. Here, the correlation was lost caused by avalanches events due to elastic rearrangements in the sample. The measurement in Figure 5.4b was recorded 1 cm from the bottom of the capillary, where no avalanche events are visible.

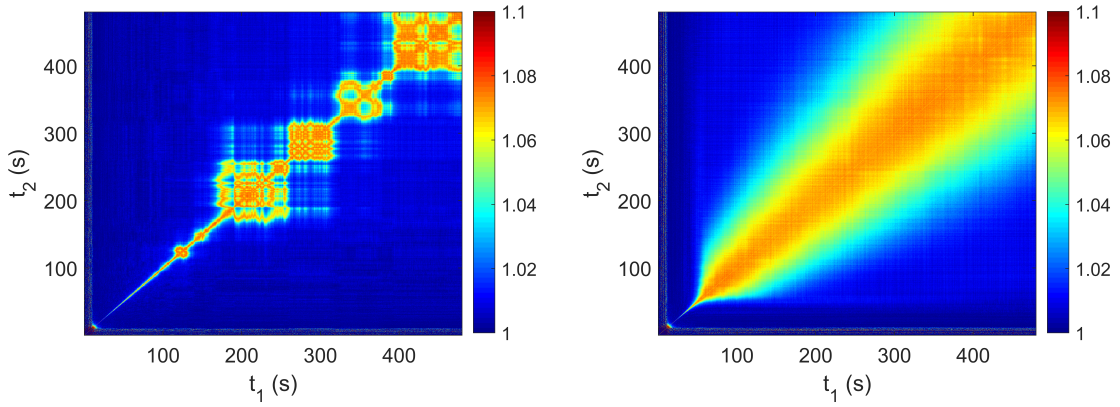

(a) Measurement recorded in the middle of the capillary.

(b) Measurement recorded in 1 cm distance from the bottom of the capillary.

Figure 5.4.: Two time correlation functions at $q = 0.01\,\mathrm{nm}^{-1}$ for quenches from 37 °C to $T_q = 4\,°\mathrm{C}$.

5.2. Radiation damage to IgG proteins

As discussed in section 2.6 biological samples like the IgG-PEG model system are sensitive to radiation damage. Thus, a radiation damage critical dose D_c has to be defined. All USAXS measurement series to investigate the quench process presented later in this thesis are collected below D_c. Radiation induced changes in the structure of the IgG-PEG model system sample were investigated at 37 °C, where the sample shows a stable single phase (Figure 3.9). Therefore, series of X-ray scattering images with varying attenuators were collected.

5.2.1. Radiation damage measurements in USAXS setup

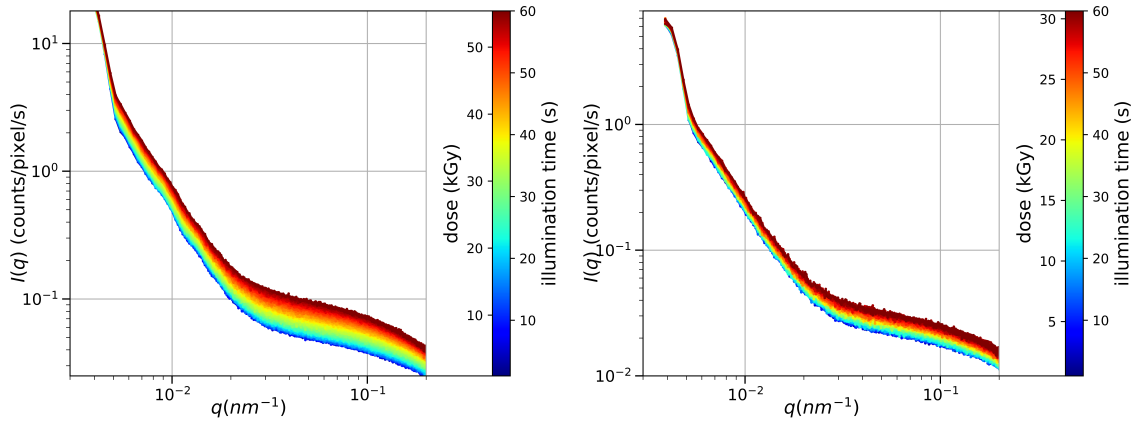

(a) Abs 0

(b) Abs 2

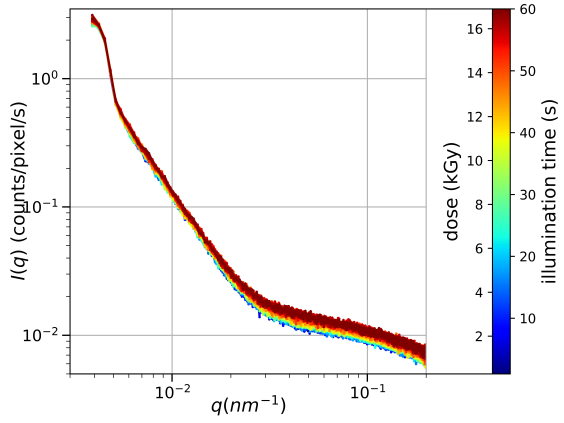

(c) Abs 4

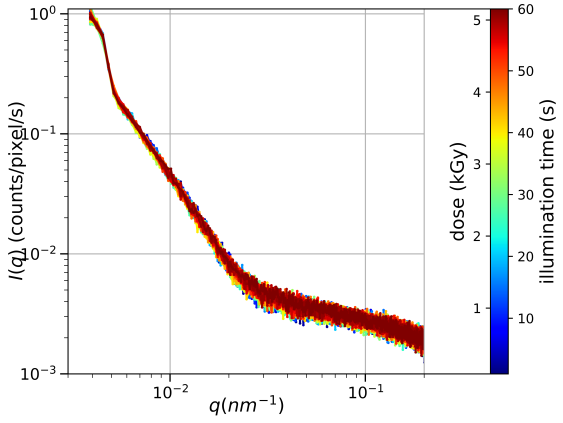

(d) Abs 8

Figure 5.5.: The X-ray scattering intensity for 60 s total exposure and different numbers of attenuators in USAXS setup.

The X-ray dose can be calculated using eq. (2.49) and the measurement parameters of the USAXS setup $F_0 = 10^{11}\,\frac{\text{Photons}}{\text{s}}$, $E_{ph} = 8.54\,\text{keV}$ and $\rho_{IgG} = 1350\,\frac{\text{g}}{\text{l}}$. The irradiated sample volume is received by the beam size of $100\times100\,\mu\text{m}^2$ and the sample thickness of $d = 1.5\,\text{mm}$. The volume fraction ϕ of the IgG dense phase was estimated to be $\phi = 19\,\%$. The X-ray transmission of 1.5 mm water at 8.54 keV was assumed as the sample transmission $A(E, d) = 0.289$. Using these parameters lead to an absorbed X-ray dose by the protein sample of 0.923 kGy per second. In order to reduce the dose per second different numbers of 25 μm thick silicon attenuators were mounted. The attenuator transmission values can be taken from table 4.1. In Figure 5.5 the time dependent X-ray scattering intensity for measurements with 60 s total exposure time and different numbers of attenuators are shown. The colorbar shows both the illumination time and the accumulated X-ray dose. An increase of intensity with the accumulated dose indicates a change in the sample structure due to radiation damage. In Figure 5.5a and Figure 5.5b an increase of intensity is visible by eyes. For 60 s total exposure using attenuator eight, which correspond to an accumulated dose of 5.15 kGy, no increase of intensity is visible in Figure 5.5d. To quantify the effect of radiation damage the scattering intensity was normalized by calculating the ratio of the intensity F_{I0} using eq. (2.54). F_{I0} in dependence of the accumulated X-ray dose is shown in Figure 5.6. For doses larger than 5 kGy an increase in F_{I0} becomes visible. Below this critical dose of $D_c \approx 5\,\text{kGy}$ no influence of absorbed dose on the static

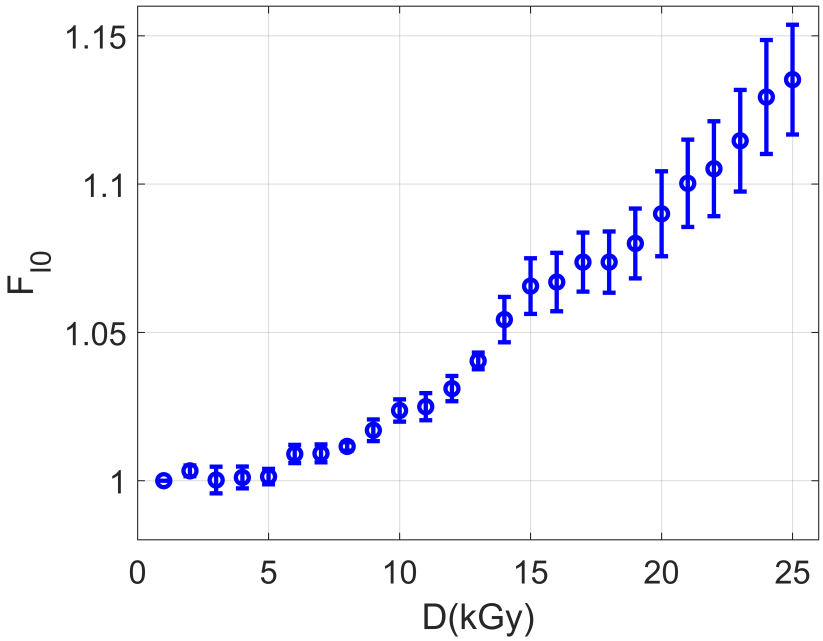

Figure 5.6.: F_{I0} shows the dependence of the scattered X-ray intensity on the accumulated dose. The increase of F_{I0} above 5 kGy indicates radiation-induced aggregation.

structure of the IgG model system was observed. All USAXS measurements to investigate the sample dynamics, which are presented later in this thesis, were collected below D_c. In Figure 5.7 the time dependent X-ray scattering intensity for illumination times up to 80 s and attenuator nine is presented, which shows no radiation damage. This illumination time and attenuator choice is equal to the XPCS series (table 4.3) to investigate the sample dynamics.

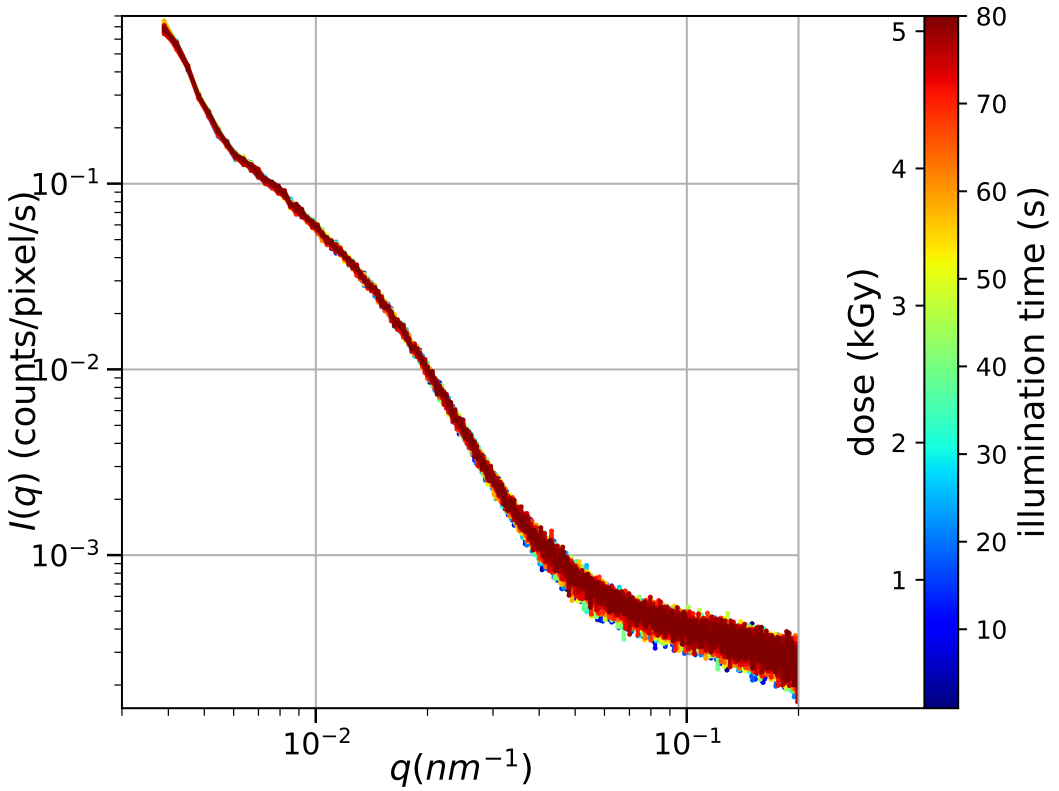

Figure 5.7.: The X-ray scattering intensity for 60 s total exposure and attenuator nine.

5.2.2. Radiation damage measurements in SAXS setup

To calculate the accumulated X-ray dose in the SAXS setup the measurement parameters in SAXS setup $F_0 = 4 \cdot 10^{10} \frac{\text{Photons}}{\text{s}}$, $E_{ph} = 13\,\text{keV}$ and $\rho_{IgG} = 1350\,\frac{\text{g}}{\text{l}}$ were inserted into eq. (2.49). The irradiated sample volume is received by the beam size of $30 \times 30\,\mu\text{m}^2$ and the sample thickness of $d = 1.5\,\text{mm}$ as known from the USAXS setup. The volume fraction ϕ of the IgG dense phase was estimated to be $\phi = 19\,\%$. The X-ray transmission of 1.5 mm water at 13 keV was assumed as the sample transmission $A(E, d) = 0.709$. These setup parameters result in an accumulated X-ray dose of 2.56 kGy per second by the protein sample in the SAXS setup. Table 4.2 shows silver attenuator transmission values. The dose and time dependent X-ray scattering intensity for a measurement at constant temperature $T = 37\,^\circ\text{C}$ without attenuator is depicted in Figure 5.8. The increasing intensity at low q and the intensity shift to lower q values indicates radiation damage due to radiation-induced aggregation.

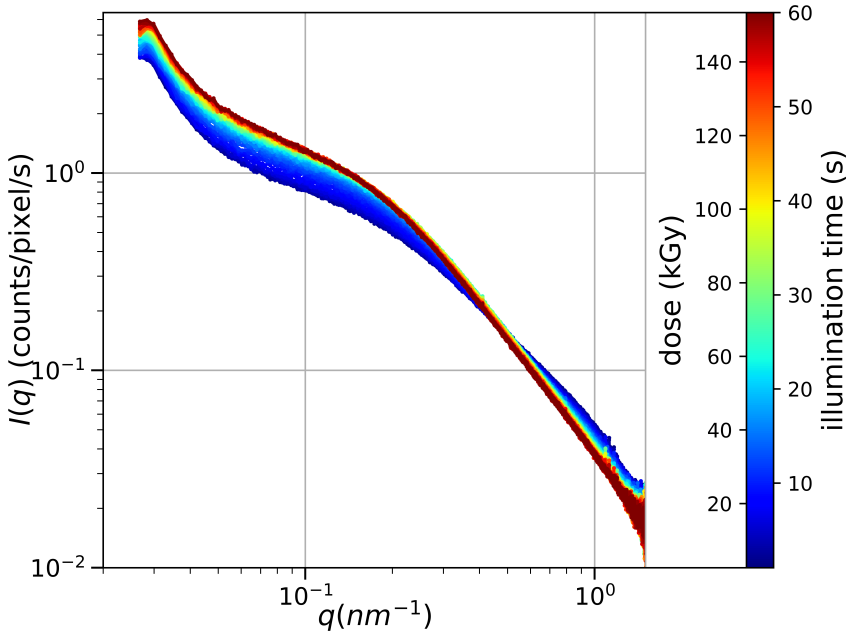

Figure 5.8.: The X-ray scattering intensity for 60 s total exposure and zero attenuators in SAXS setup.

Figure 5.9 shows the time dependent X-ray scattering intensity for series recorded using the SAXS-XPCS measurement parameters (table 4.4). Within the illumination times and attenuation settings used, no change in scattering intensity over time is visible by eye.

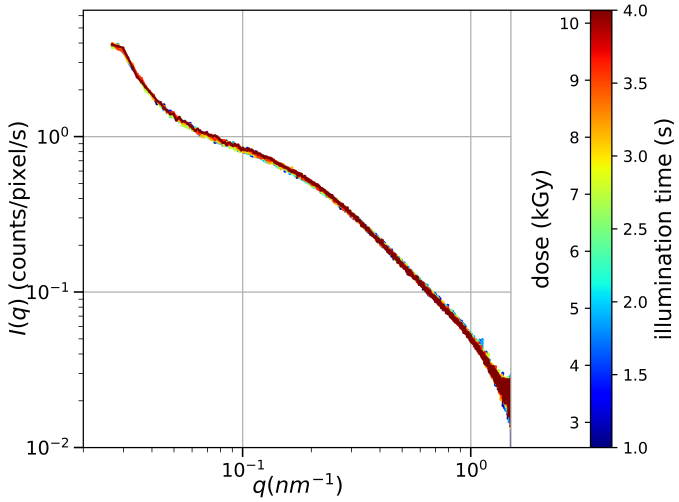

(a) X-ray scattering intensity for 4 s exposure and zero silver attenuators.

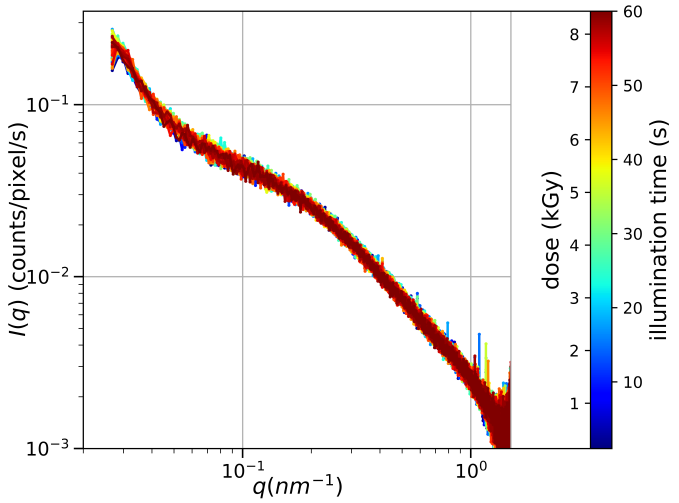

(b) X-ray scattering intensity for 60 s exposure and four silver attenuators.

Figure 5.9.: Radiation damage test measurements using the SAXS-XPCS measurement parameters.

The ratio of the intensity F_{I0} was also calculated for the SAXS measurements to quantify the effect of radiation damage. F_{I0} as a function of the accumulated X-ray dose is shown in Figure 5.6. For doses larger than 7.5 kGy an slightly increase in F_{I0} becomes visible. We decided to record XPCS measurements up to a dose of 10 kGy.

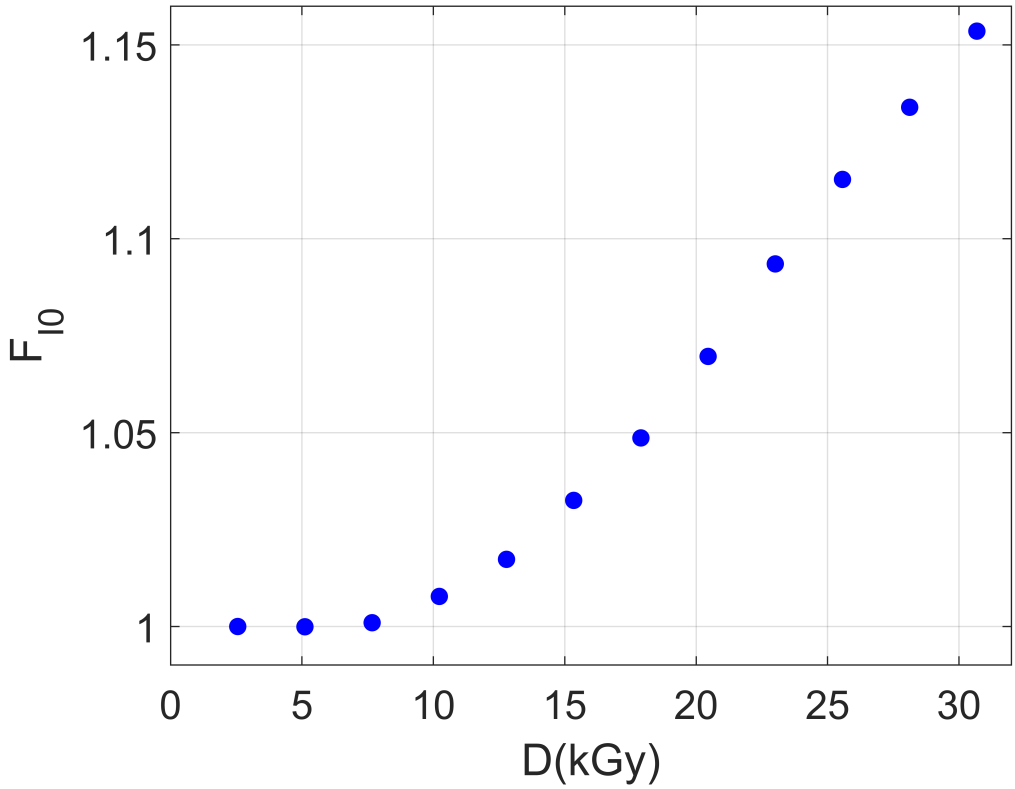

Figure 5.10.: F_{I0} shows the dependence of the scattered X-ray intensity on the accumulated dose.

5.3. USAXS analysis of the quenched IgG model system

In this section the results of the kinetic and dynamic analysis of the USAXS data are presented. The USAXS data correspond to protein droplets with a characteristic length in the micrometer range. First the sample kinetics are investigated. Thereby the temporal evolution of the characteristic length of the IgG domains in dependence of the quench temperature T_q is analysed. Later the sample dynamics will be characterized.

5.3.1. Kinetics

To investigate the kinetics and dynamics of the IgG model system, the system was quenched from the equilibrated homogenous phase at 37 °C to different temperatures below the binodal. The USAXS X-ray scattering profile was recorded as a function of the waiting time t_w after the quench temperature was reached. For the initial time range ($t_w < 20\,\mathrm{s}$) USAXS scattering profiles were analysed every 3 s. For larger t_w the time steps were 10 s. The scattering profiles for all qunech temperatures show a peak in the structure factor, which is shifting to smaller q with increasing t_w. This shift of the peak in the structure factor is connected to the growth kinetic of the system (section 3.6). The peak position q_{max} can be determined using the scaling function

$$S(q) = a\frac{\left(\frac{q}{q_{max}}\right)^2}{2+\left(\frac{q}{q_{max}}\right)^7}, \tag{5.1}$$

according to Furukawa[34].

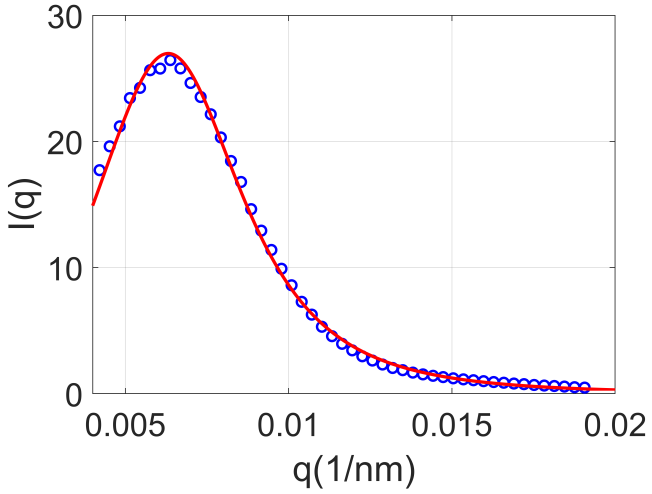

Figure 5.11.: Scaling function fit to determine q_{max} for the quench temperature 4 °C and $t_w = 13.5\,\mathrm{s}$.

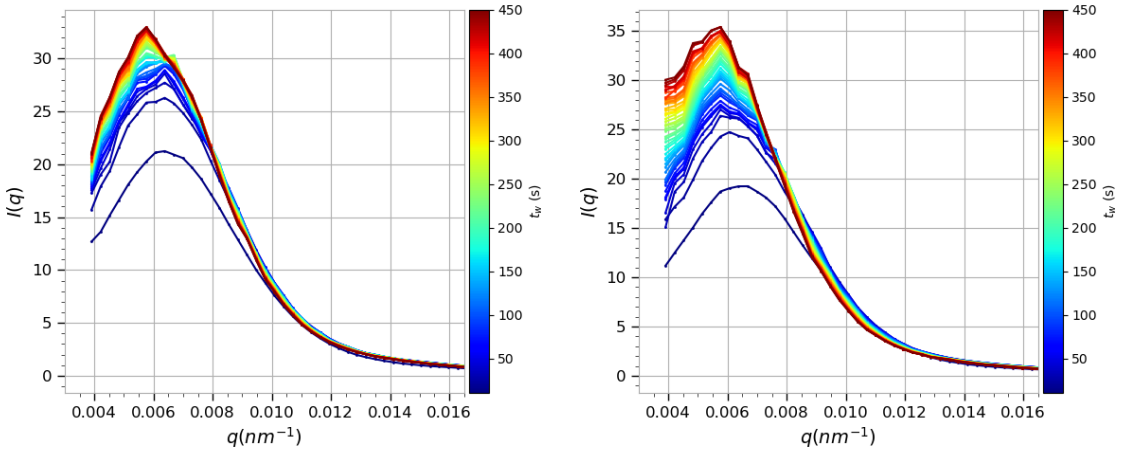

(a) $T_q = 4\,^{\circ}\mathrm{C}$ (b) $T_q = 6\,^{\circ}\mathrm{C}$

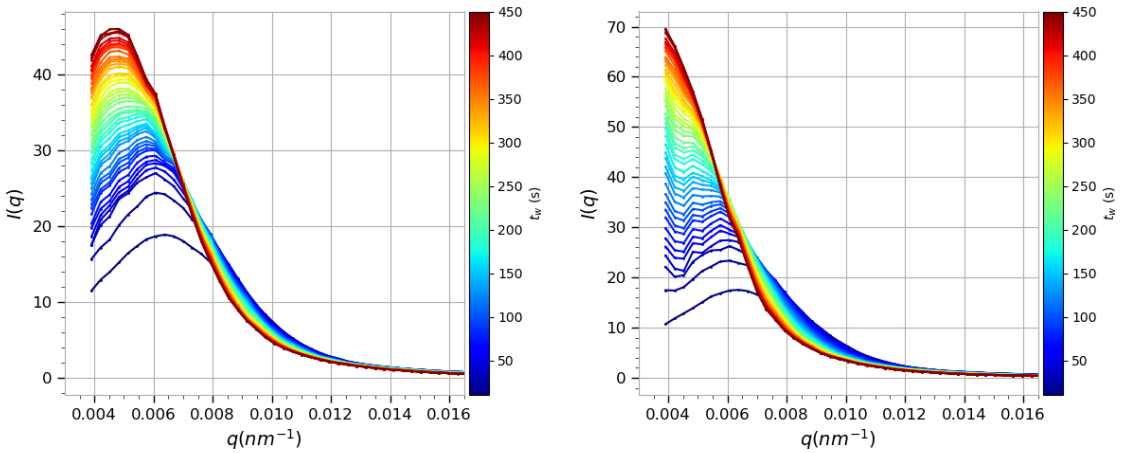

(c) $T_q = 8\,^{\circ}\mathrm{C}$ (d) $T_q = 10\,^{\circ}\mathrm{C}$

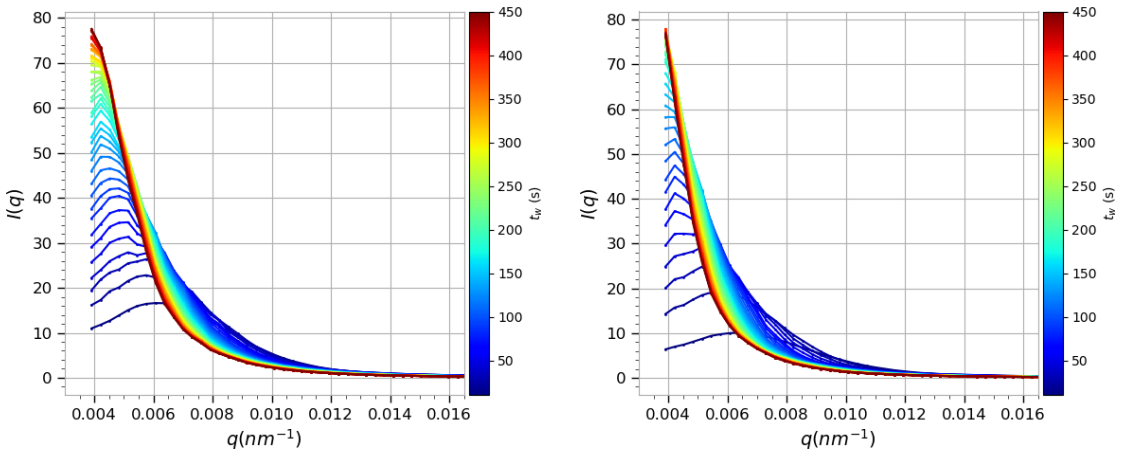

(e) $T_q = 12\,^{\circ}\mathrm{C}$ (f) $T_q = 15\,^{\circ}\mathrm{C}$

Figure 5.12.: Temporal evolution of the USAXS profile after a quench from 37 °C to different temperatures T_q.

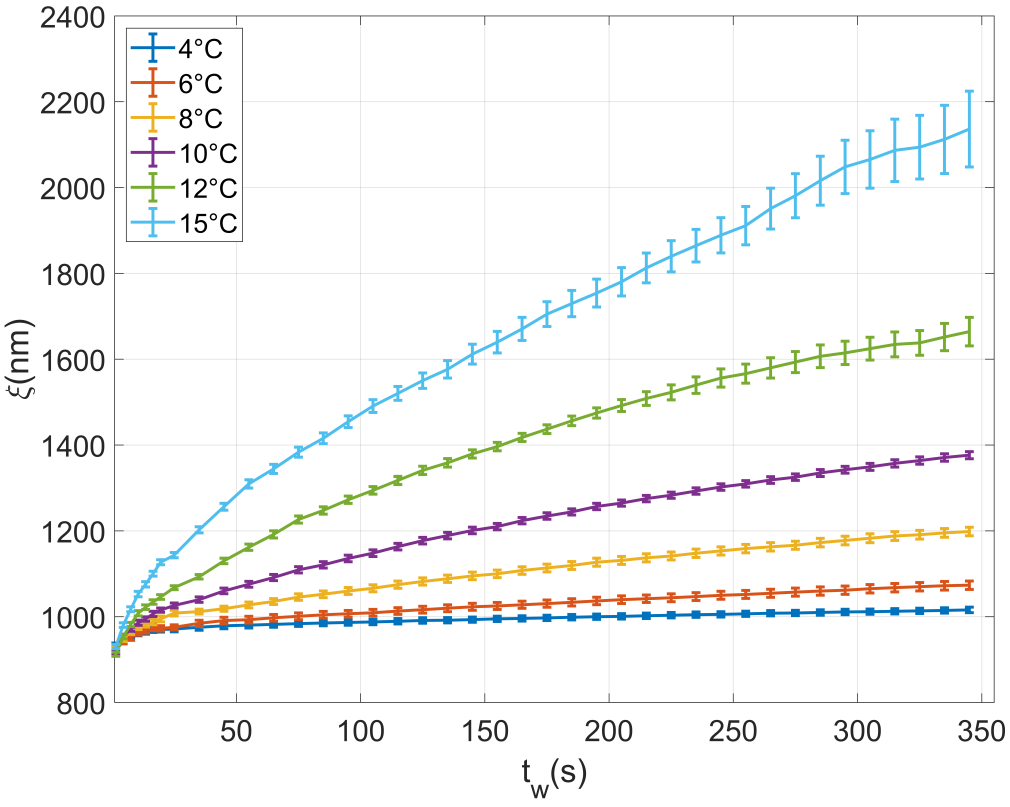

Figure 5.13.: Temporal evolution of the characteristic length ξ after a quench from 37 °C to different temperatures T_q.

Figure 5.11 shows the scaling function to determine q_{max} for the quench temperature 4 °C and $t_w = 13.5$ s exemplary. In Figure 5.12 the temporal evolution of the USAXS profile after a quench from 37 °C to different temperatures is presented. For shallow quenches to temperatures $T_q \geq 10$ °C the peak position q_{max} is shifting behind the beamstop. With deeper quench depth in the phase diagram to lower temperatures the peak evolution slows down. For the deep quench to $T_q = 4$ °C the peak position q_{max} becomes almost stationary. Using eq. (3.35) the characteristic length scale ξ of the protein droplet can be calculated from q_{max}. Figure 5.13 shows the temporal evolution of ξ for quenches to different T_q. The temporal evolution of ξ can be described by the power law equation

$$\xi = C \cdot t^b. \tag{5.2}$$

The power law for diffusive growth

$$\xi \propto t^{\frac{1}{d}}, \tag{5.3}$$

where $d = 3$ is the dimensionality of the system, is expected in the case of a classical spinodal decomposition. The exponential fits of the temporal evolution of ξ using eq. (5.2)

are shown in Figure 5.14a. In Figure 5.14b the exponent b is dependence of the quench temperature T_q is presented. For $T_q = 15\,^{\circ}\mathrm{C}$ the exponent $b = 0.33 \pm 0.01$ meets the condition for the diffusive growth in the case of a classical spinodal decomposition. With decreasing T_q and increasing quench depth the growth exponent b decreases. Finally for a deep quench to $T_q = 4\,^{\circ}\mathrm{C}$ the kinetics become arrested.

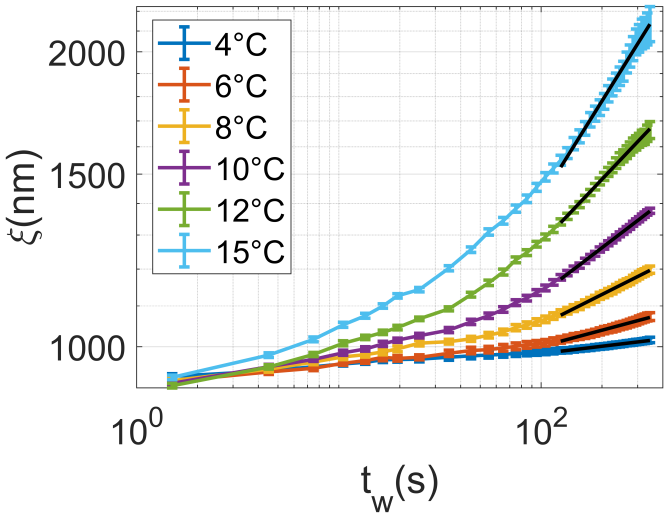

(a) Temporal evolution of the characteristic length ξ after a quench from 37 °C to different temperatures T_q. The exponetial fits are marked by black lines.

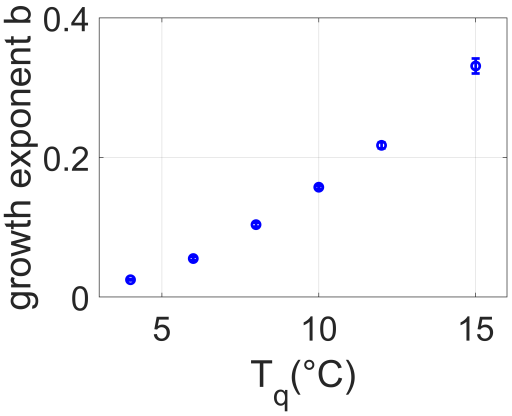

(b) Growth exponent b in dependence of T_q. The error bars are within the cirlce symbol size, if they are not visible.

Figure 5.14.: Growth kinetics of the IgG model system.

5.3.2. Aging dynamics at small q

The dynamics of protein droplets during phase separation of the IgG model system were measured the first time. To investigate the dynamics of the IgG model system the measurements presented in table 4.3 were analysed. First, two-time correlation functions (TTC) were calculated using Xana. As an example, Figure 5.15 shows the TTC for the first 60 s of the measurement during a quench from $T = 37\,^{\circ}\mathrm{C}$ to $T_q = 4\,^{\circ}\mathrm{C}$. During the quench process the temperature was recorded by the Linkam heating stage. Figure 5.16 shows the temporal evolution of the temperature T of the Linkam stage during the first 20 s of the measurement, which was started 10 s after the Linkam stage started the quench process. In the beginning of the measurement the IgG model system is still in the homogenous state and the intensity for the considered q is negligibly low, so that only noise correlation is measured. The region of high correlation after 10 s is an artefact and belongs also to noise correlation.

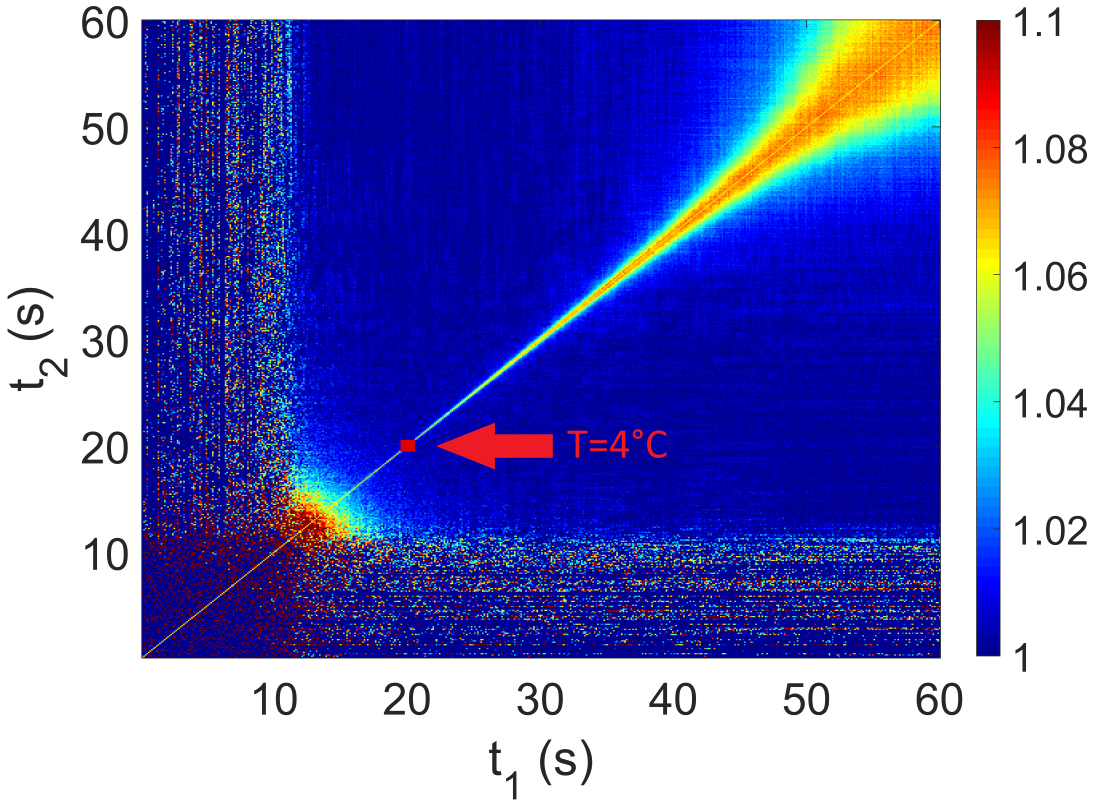

Figure 5.15.: Two-time correlation function of the measurement during a quench from $T = 37\,^{\circ}\mathrm{C}$ to $T_q = 4\,^{\circ}\mathrm{C}$. The red square marks the time $t = 20\,\mathrm{s}$ when $T_q = 4\,^{\circ}\mathrm{C}$ is reached. For the further analysis this point determines the waiting time $t_w = 0$.

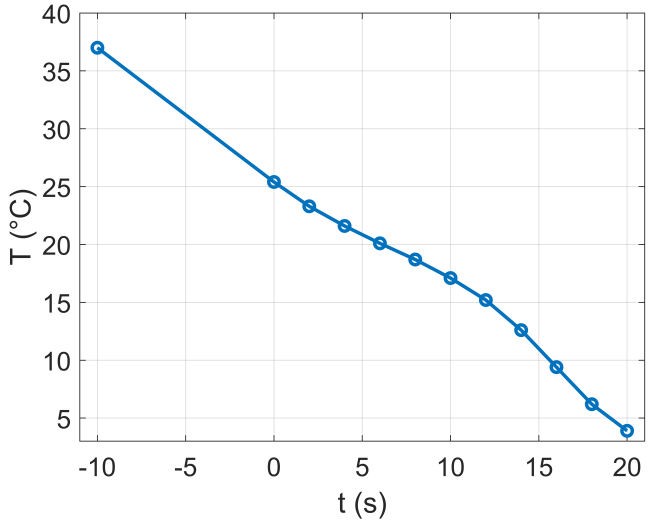

$t(s)$	$T(°C)$
-10	37
0	25.4
2	23.3
4	21.6
6	20.1
8	18.7
10	17.1
12	15.2
14	12.6
16	9.4
18	6.2
20	3.9

Figure 5.16.: Temporal evolution of the temperature T during the quench to $T_q = 4\,°\mathrm{C}$. The data points show that the quench process was started 10 s before the XPCS measurement.

The dynamics are analysed as a function of the waiting time t_w after the quench temperature was reached. The time $t_w = 0$ is defined as the time after T_q was reached, which is marked by the red square in Figure 5.16. At this point the high correlation area begins to widen along the diagonal of the TTC, which indicates that the sample dynamics start to slow down. The TTC for the initial 60 s as well as the temporal evolution of the temperature for the quench to other T_q are shown in the appendix. For the early ageing the TTC become faster with increasing quench depth. Figure 5.17 shows the two-time correlation functions at $q = 0.01\,\mathrm{nm}^{-1}$ for a quench from 37 °C to different temperatures T_q for the whole measurements up to 480 s. Generally, for all quenches the early dynamics are on the scale of seconds before a slowdown is observed. At larger time scales the dynamics become slower with increasing quench depth.
To investigate the dynamics horizontal cuts starting on the TTC diagonal were extracted from the TTCs to get correlation functions in dependence of the waiting time t_w as presented in section 2.4. The extracted correlation functions were modeled by MATLAB using an exponential function with two dynamical relaxations

$$g_2(\vec{q},\tau) = a + \beta_1 \exp\left(-2\left(\Gamma\tau\right)^{\gamma_1}\right) + \beta_2 \exp\left(-2\left(\Gamma_2\tau\right)^{\gamma_2}\right). \tag{5.4}$$

where β_1, Γ_1 and γ_1 are the contrast, decay rate and KWW exponent of the fast relaxation and β_2, Γ_2 and γ_2 are the corresponding parameters for the slow relaxation. For the shallow quenches to 10 °C, 12 °C and 15 °C a small third exponential decay with a maximum contrast of 0.02 and a minimum decorrelation time of 150 s was needed to fit a tail on long time scales.

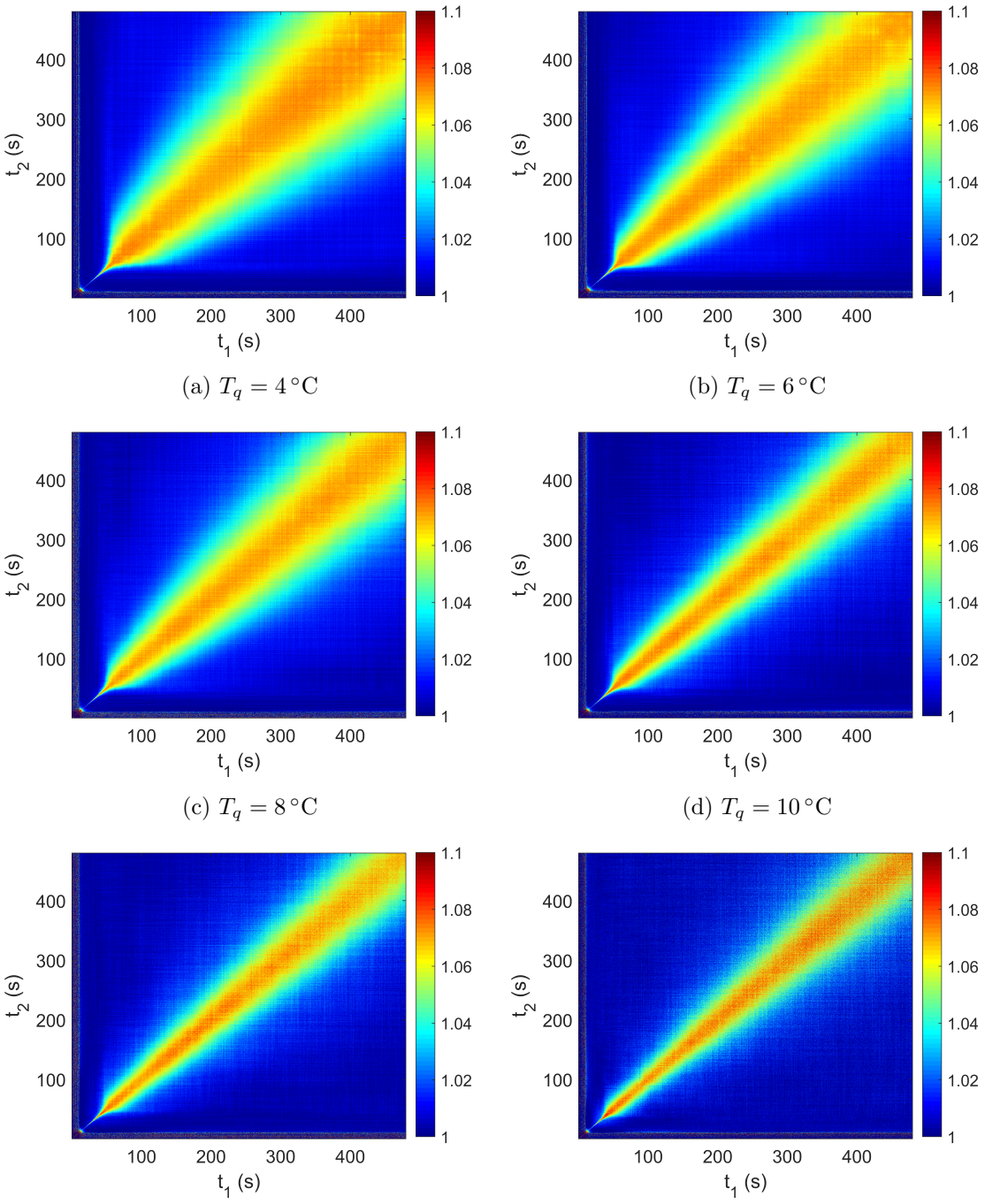

(a) $T_q = 4\,^\circ\mathrm{C}$ (b) $T_q = 6\,^\circ\mathrm{C}$

(c) $T_q = 8\,^\circ\mathrm{C}$ (d) $T_q = 10\,^\circ\mathrm{C}$

(e) $T_q = 12\,^\circ\mathrm{C}$ (f) $T_q = 15\,^\circ\mathrm{C}$

Figure 5.17.: Two-time correlation functions at $q = 0.01\,\mathrm{nm}^{-1}$ for a quench from $37\,^\circ\mathrm{C}$ to different temperatures T_q.

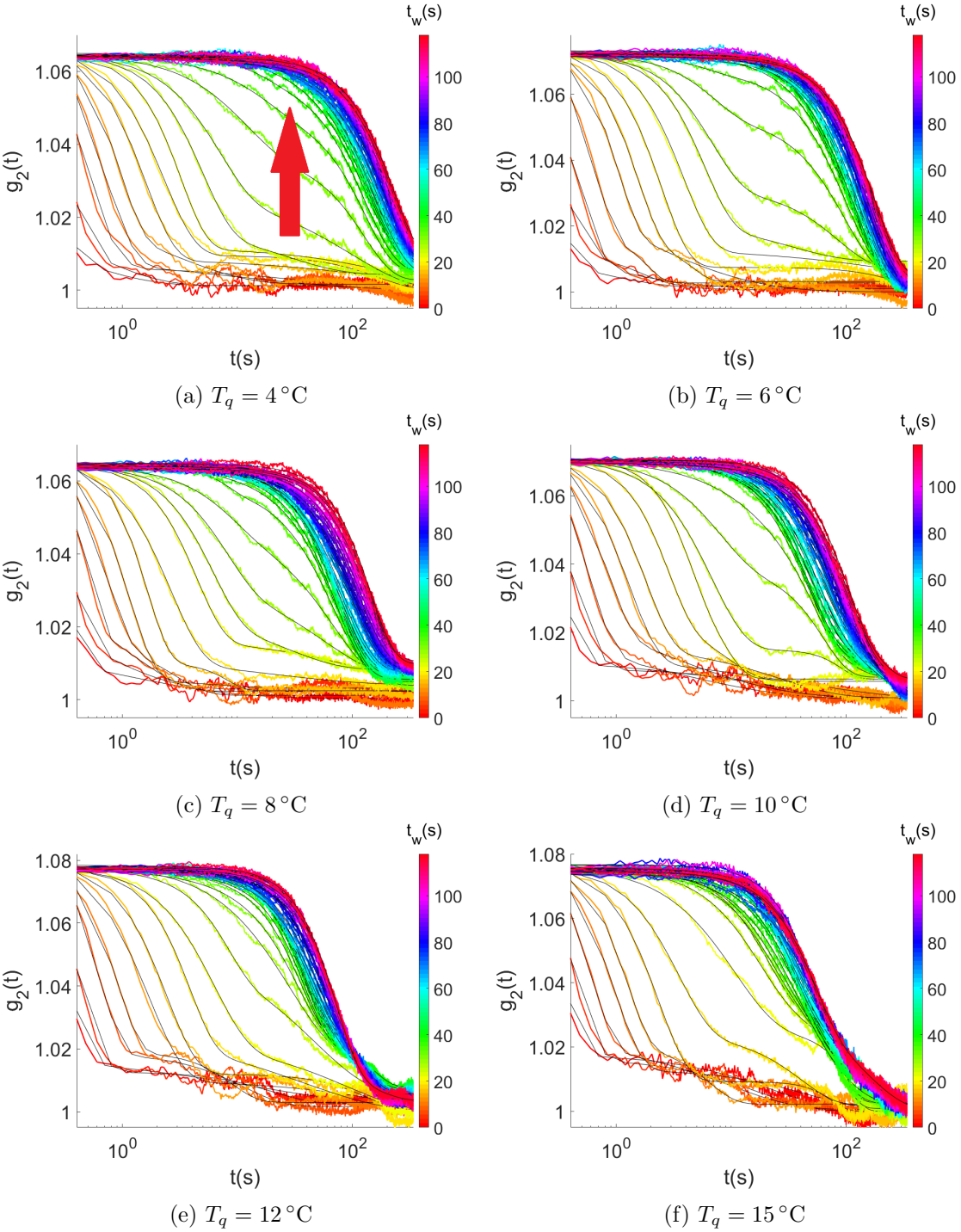

(a) $T_q = 4\,^{\circ}\mathrm{C}$ (b) $T_q = 6\,^{\circ}\mathrm{C}$

(c) $T_q = 8\,^{\circ}\mathrm{C}$ (d) $T_q = 10\,^{\circ}\mathrm{C}$

(e) $T_q = 12\,^{\circ}\mathrm{C}$ (f) $T_q = 15\,^{\circ}\mathrm{C}$

Figure 5.18.: Correlation functions depending on the waiting time t_w for the different T_q. The exponential fits are displayed by black lines. The red arrow in (a) shows the increasing second relaxation mode.

The waiting time dependent correlation functions at $q = 0.0065\,\mathrm{nm}^{-1}$ for the quenches to the different T_q are shown in Figure 5.18. During the early ageing a fast relaxation process is dominant. A slower second relaxation decay appears at $t_w \approx 20\,\mathrm{s}$, which is marked by a red arrow in Figure 5.18a. The contribution of the slow process increases with time until the fast process vanishes during the time period between $t_w \approx 40\,\mathrm{s}$ and $50\,\mathrm{s}$.
To understand the dynamics in detail the fit parameters for all T_q are considered. Figure 5.19 gives an overview about the fit parameter for the quench to $T_q = 4\,^\circ\mathrm{C}$. The fit parameter for the other T_q are shown in the appendix. First, the contrast of both relaxation processes as a function of t_w for $T_q = 4\,^\circ\mathrm{C}$ is shown in Figure 5.19a. For very early times after $T_q = 4\,^\circ\mathrm{C}$ was reached the dynamics are so fast that only the final stage of the decay is measured and fitted, which explains the large errorbars for small t_w. Between $t_w \approx 20\,\mathrm{s}$ and $40\,\mathrm{s}$ the β_1 decreases and β_2 increases indicating that the slow process becomes dominant.

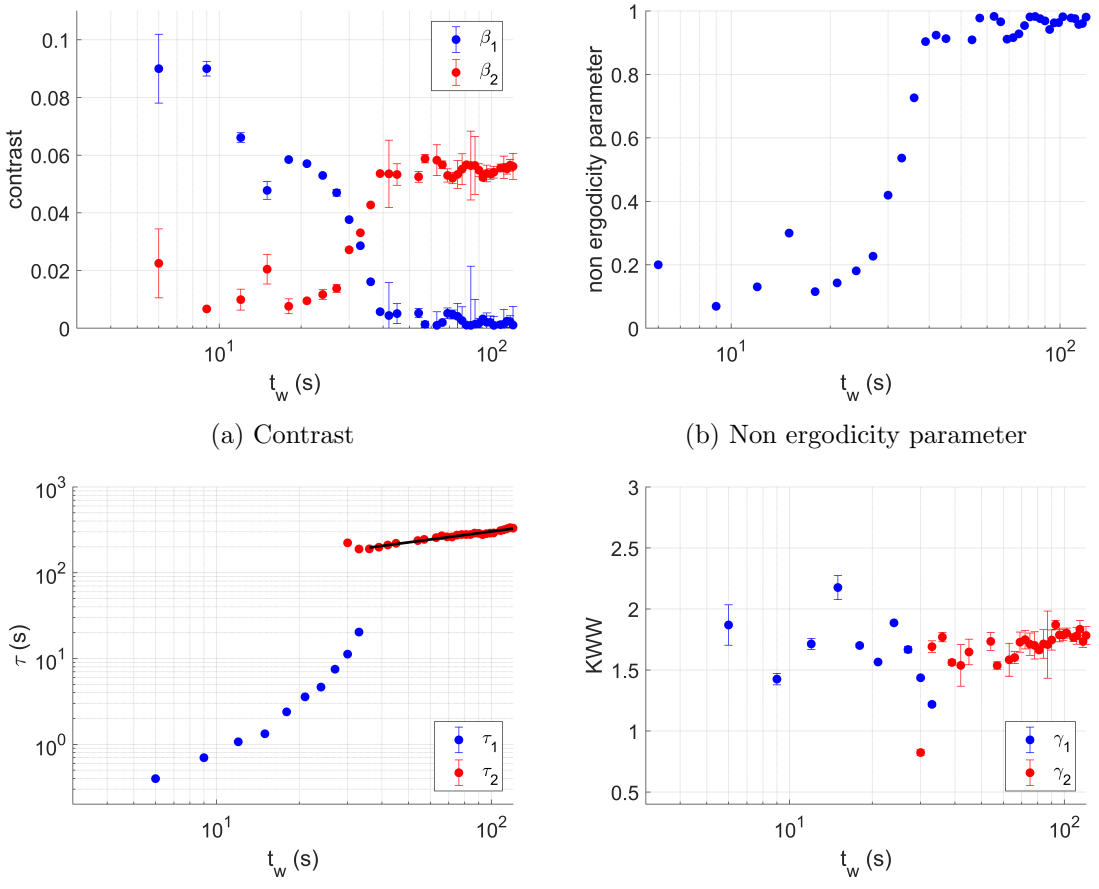

(a) Contrast

(b) Non ergodicity parameter

(c) Decorrelation time

(d) KWW

Figure 5.19.: Exponential fit parameter with two dynamical relaxations for the quench to $T_q = 4\,^\circ\mathrm{C}$.

In Figure 5.19b the non-ergodicity parameter [68] calculated as $\frac{\beta_2}{\beta_1+\beta_2}$ is presented, which is increasing rapidly when the slow relaxation appears. In Figure 5.19c and Figure 5.19d the decorrelation time

$$\tau = 1/\Gamma \tag{5.5}$$

and the KWW exponent γ in dependence of t_w are shown. Only values for relaxation with a contrast $\beta > 0.022$ are displayed to eliminate a noisy second datapoint. The decorrelation time for the fast process increases showing an exponential behaviour until $t_w = 35\,\mathrm{s}$. When the slow relaxation becomes dominant the decorrelation time τ follows a power law

$$\tau(t_w) = a \cdot t_w^b. \tag{5.6}$$

For the quench to $T_q = 4\,^\circ\mathrm{C}$ the parameter $a = 43 \pm 5$ and $b = 0.42 \pm 0.03$ were determined. This power law behaviour is displayed by the black line in Figure 5.19c. The decorrelation time of the slow process assumes values larger than 100 s, which is referred to be the threshold for the glassy phase [102].
The KWW exponent shows values between 1.5 and 2 for all temperatures.

The temporal evolution of the decorrelation time τ for all quenches is presented in Figure 5.20. In general, for all quench temperatures three stages of ageing dynamics are observed. During the early stage until $t_w \approx 35\,\mathrm{s}$ fast dynamics are observed and the decorrelation time slows down with an exponential behaviour. At early t_w the decorrelation time decreases with the quench depth, i. e. the dynamics become faster with deeper quenches to lower temperatures. In Figure 5.21a the temperature dependent decorrelation time at $t_w = 15\,\mathrm{s}$ is shown exemplarily. Here, the dynamics of the spinodal decomposition are driven by the curvature of the free energy $\frac{\partial^2}{\partial c^2}F$. With deeper quench depths the magnitude of $\frac{\partial^2}{\partial c^2}F$ increases and the dynamics become faster.
During the second stage the slower relaxation mode appears and becomes dominant for all temperatures. The non-ergodicity parameter is increasing on this time scale.
In the third stage coarsening dynamics are observed and the IgG model system shows an ageing with power-law behaviour. Here, the inverted temperature behaviour between early and late ageing becomes clearly visible. For large t_w the dynamics become slower with increasing quench depth, which is presented in Figure 5.21b for the temperature dependent decorrelation time after $t_w = 99\,\mathrm{s}$. This temperature dependence of the coarsening dynamics is caused by the reduced mobility of the arrested phase for deep quenches at low temperatures.

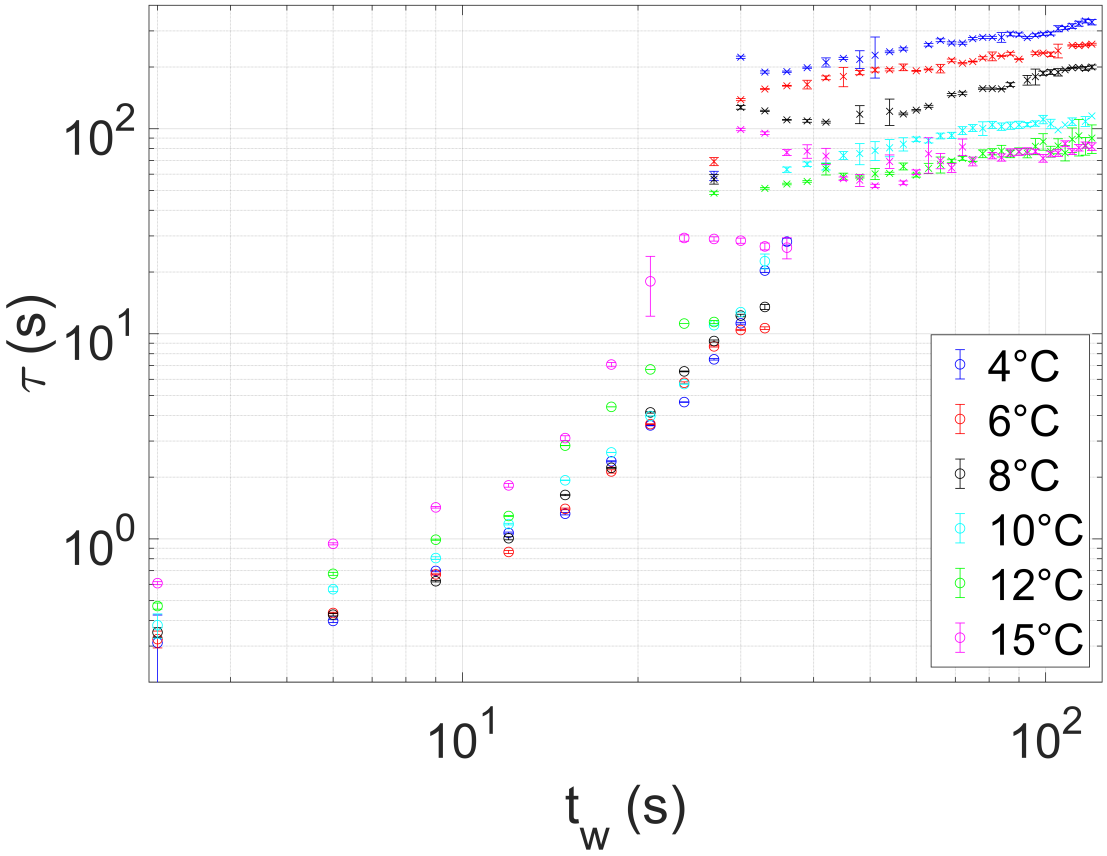

Figure 5.20.: Decorrelation time as a function of the waiting time t_w for quenches to different temperatures T_q. The cirlces mark the fast relaxation and the crosses mark the slow relaxation.

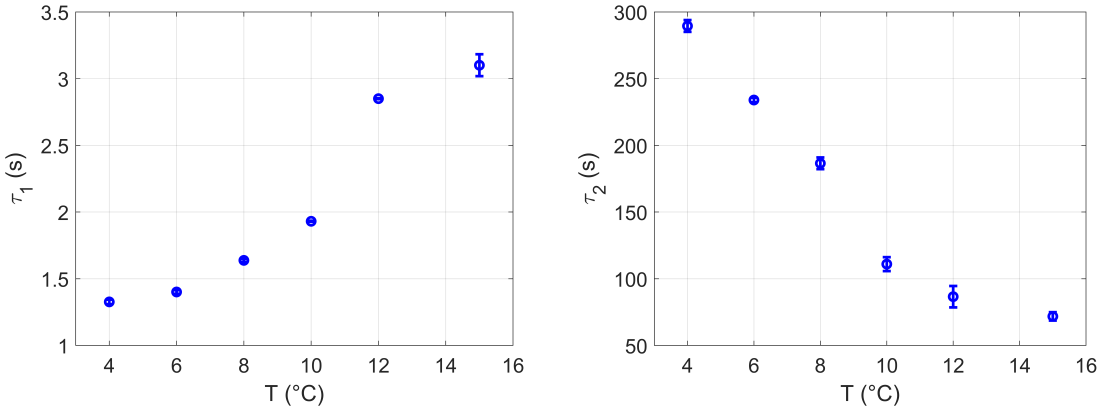

(a) $t_w = 15\,\mathrm{s}$ (b) $t_w = 99\,\mathrm{s}$

Figure 5.21.: The IgG model system shows a reserve temperature dependence of the decorrelation time during early and late ageing dynamics.

The behaviour of the dynamical parameters in dependence of q was investigated to characterize the sample dynamics of the IgG model system. The decay rate Γ and the KWW exponent γ as well as their q dependence were analysed to evaluate the dynamics during the LLPS (see section 2.4 and [64]). To analyse the ageing dynamics fourteen q values between $q = 0.0055\,\mathrm{nm}^{-1}$ and $q = 0.0120\,\mathrm{nm}^{-1}$ for the quench to $T_q = 4\,^{\circ}\mathrm{C}$ were selected and TTC were calculated using Xana. In Figure 5.22 the TTC at $q = 0.0055\,\mathrm{nm}^{-1}$ and $q = 0.0120\,\mathrm{nm}^{-1}$ are shown. The TTCs at the q values in between are presented in the appendix in Figure A.16 and Figure A.17.

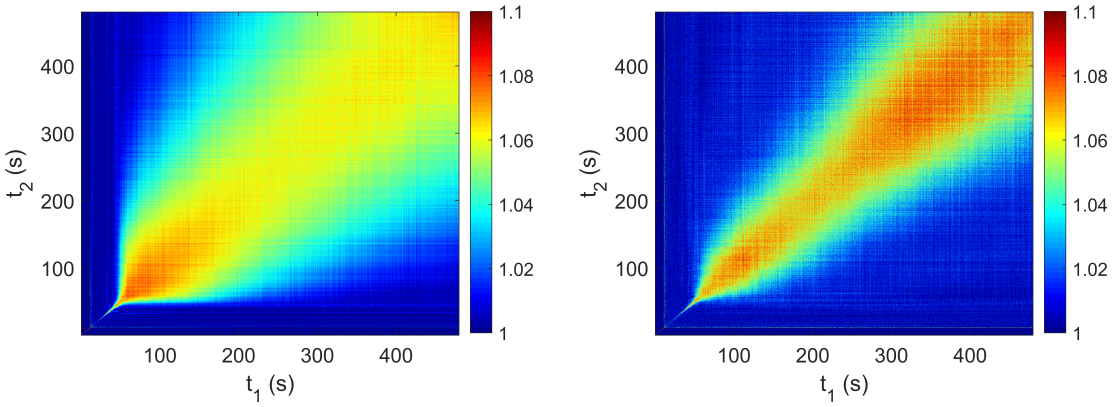

(a) $q = 0.0055\,\mathrm{nm}^{-1}$ (b) $q = 0.0120\,\mathrm{nm}^{-1}$

Figure 5.22.: TTC at different q values for the quench of the IgG model system to $T_q = 4\,^{\circ}\mathrm{C}$.

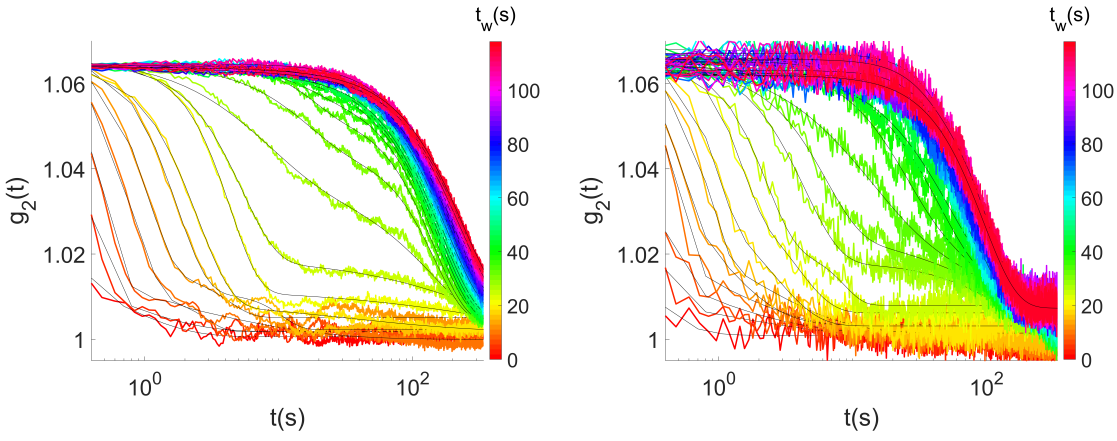

(a) $q = 0.0055\,\mathrm{nm}^{-1}$ (b) $q = 0.0120\,\mathrm{nm}^{-1}$

Figure 5.23.: Correlation functions at different q values for the quench of the IgG model system to $T_q = 4\,^{\circ}\mathrm{C}$.

With increasing q the dynamics become faster indicated by a smaller area of high correlation around the diagonal of the TTC. Waiting time dependent correlation functions have also been determined for these 14 q values using eq. (5.4). Figure 5.23 shows the correlation functions as a function of t_w for $q = 0.0055\,\mathrm{nm}^{-1}$ and $q = 0.0120\,\mathrm{nm}^{-1}$. The characteristic ageing dynamics with three stages are visible at all q values. The correlation functions at the q values in between are also presented in the appendix in Figure A.18 and Figure A.19. Due to the lower scattering intensity at higher q beside the peak (see Figure 5.12a), the correlation functions become more noisy with increasing q. The q dependent decorrelation time calculated using eq. (5.5) of the dominant relaxation process is shown in Figure 5.24. The relationship between the decay rate Γ and q is determined using the fit function

$$\Gamma = a \cdot q^b. \tag{5.7}$$

Figure 5.25a shows the q dependent decay rate Γ_1 of the fast relaxation at $t_w = 27\,\mathrm{s}$. The Γ vs q relationship is described by the exponent $b = 1.25 \pm 0.33$. For the slow relaxation at $t_w = 120\,\mathrm{s}$ the q dependent decay rate Γ_1 is presented in Figure 5.25b and $b = 1.17 \pm 0.22$ was found. In Figure 5.25c and Figure 5.25d the KWW exponents in dependence of q at $t_w = 27\,\mathrm{s}$ and $t_w = 120\,\mathrm{s}$ are shown. For the early phase of the liquid-liquid phase separation of the IgG model system γ_1 between 1.4 and 2 were found.

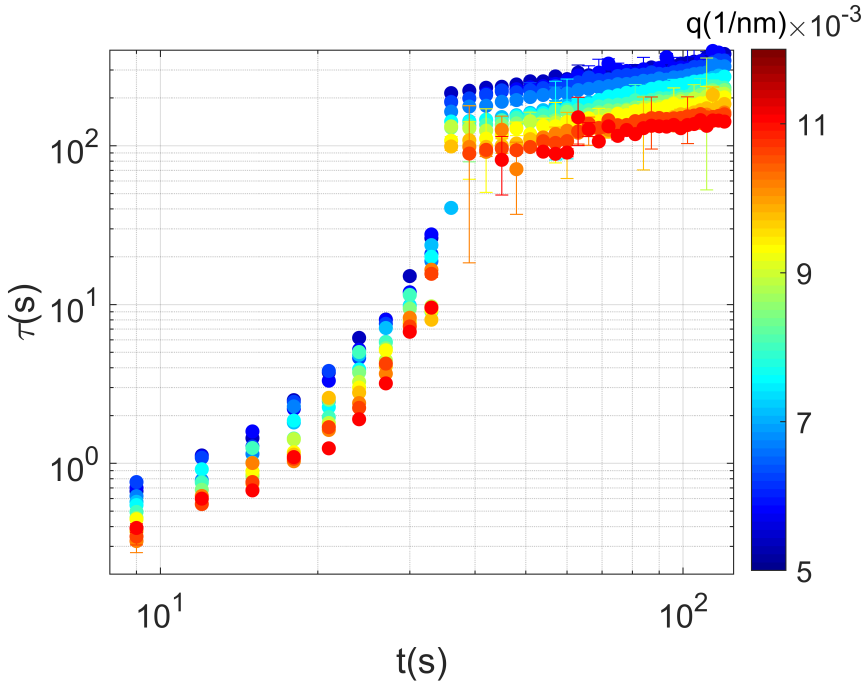

Figure 5.24.: Decorrelation time τ as a function of t_w for different q values for the quench to $T_q = 4\,^\circ\mathrm{C}$.

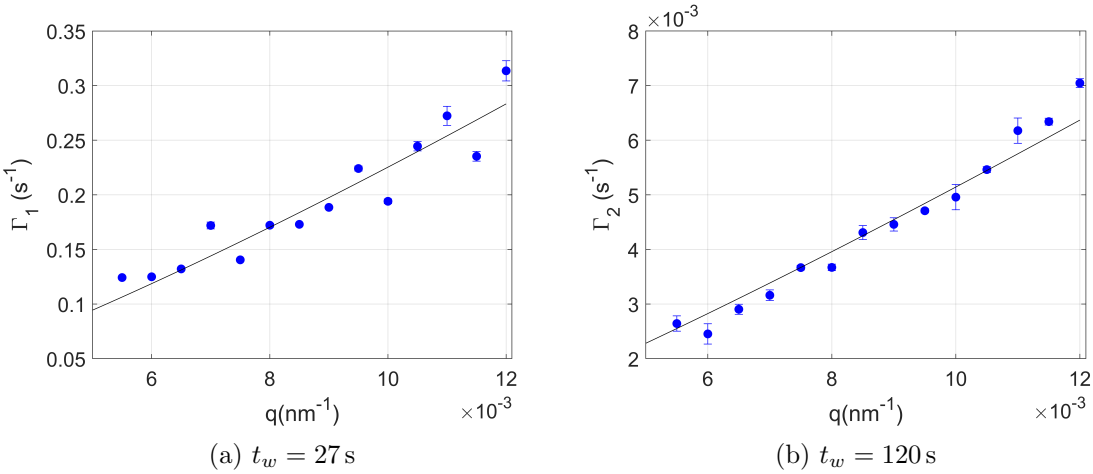

(a) $t_w = 27\,\mathrm{s}$ (b) $t_w = 120\,\mathrm{s}$

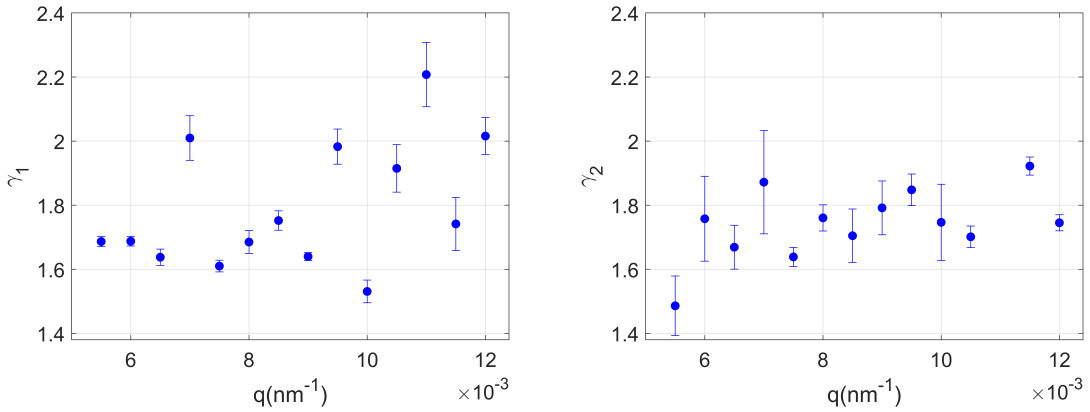

(c) $t_w = 27\,\mathrm{s}$ (d) $t_w = 120\,\mathrm{s}$

Figure 5.25.: Decorrelation time and KWW exponent of the early and late dynamics for the quench to $T_q = 4\,^{\circ}\mathrm{C}$. The black lines in (a) and (b) mark the Γ vs q fit function.

The slow relaxation caused by coarsening dynamics were investigated up to $q = 0.03\,\mathrm{nm}^{-1}$ in the USAXS setup. In order to compensate the low statistics due to the dropping intensity with increasing q correlation functions were calculated by averaging on a time window from $t_w = 220\,\mathrm{s}$ to $t_w = 460\,\mathrm{s}$. This corresponds to the second half of the TTCs shown in Figure 5.17. During this time interval the slow relaxation is predominant, therefore a single exponential Kohlrausch-Williams-Watts [99] fit

$$g_2(\vec{q},\tau) = a + \beta_2 \exp\left(-2\left(\Gamma_2\tau\right)^{\gamma_2}\right) \tag{5.8}$$

is sufficient to determine the decay rate Γ_2 and the KWW exponent γ_2. In Figure 5.26 the correlation functions up to $q = 0.03\,\mathrm{nm}^{-1}$ for the different quenches are shown. The correlation functions at $q = 0.03\,\mathrm{nm}^{-1}$ show noise despite of time averaging. For larger q values in SAXS setup several measurements were collected and averaged to increase the

SNR (see section 5.4).

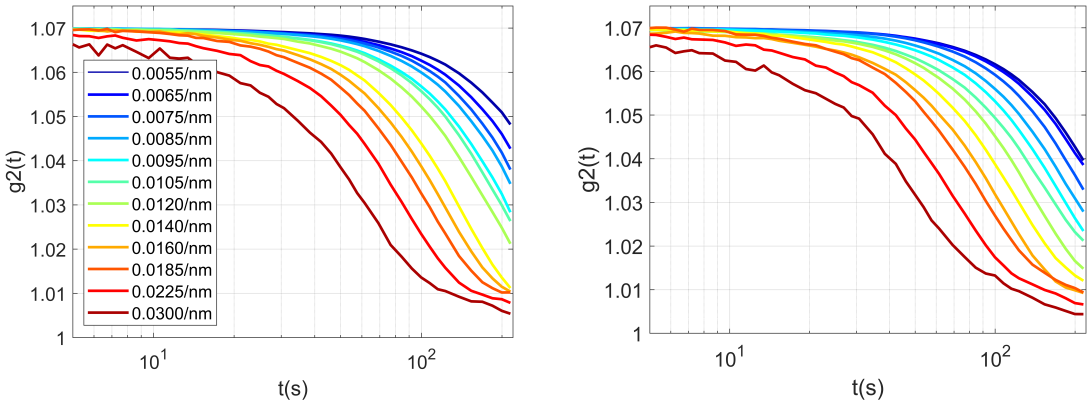

(a) $T_q = 4\,°\mathrm{C}$ (b) $T_q = 6\,°\mathrm{C}$

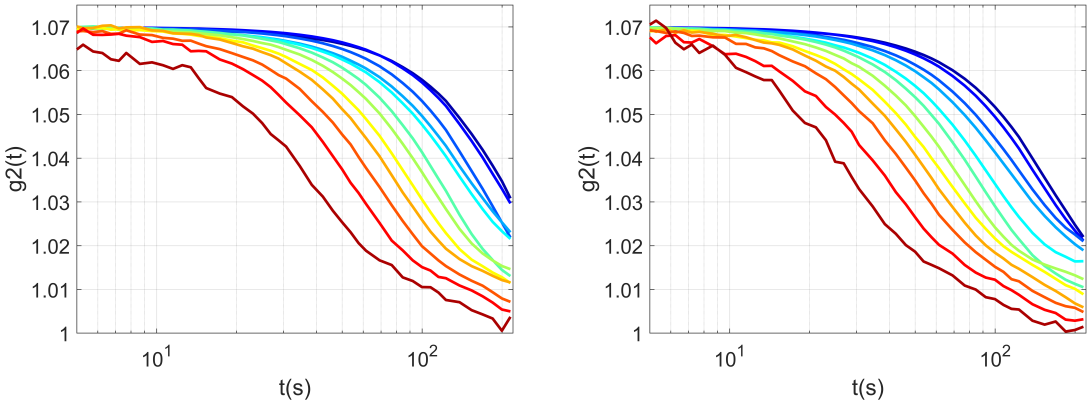

(c) $T_q = 8\,°\mathrm{C}$ (d) $T_q = 10\,°\mathrm{C}$

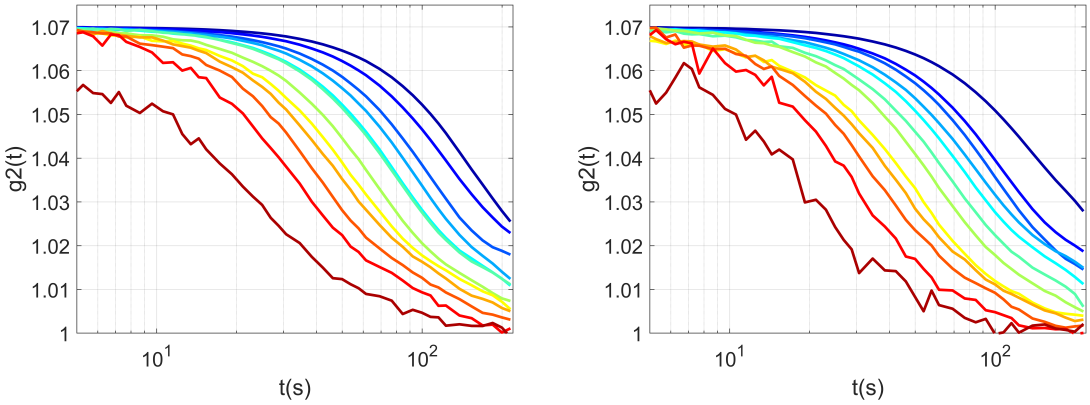

(e) $T_q = 12\,°\mathrm{C}$ (f) $T_q = 15\,°\mathrm{C}$

Figure 5.26.: q dependent correlation functions on a time interval from $t_w = 220\,\mathrm{s}$ to $t_w = 460\,\mathrm{s}$ for the quenches to different T_q.

In Figure 5.27 the decay rate Γ_2 as a function of q for the time interval from $t_w = 220\,\mathrm{s}$ to $t_w = 460\,\mathrm{s}$ is shown. Here also the clear temperature dependence for the coarsening dynamics becomes visible by the decreasing decay rate Γ_2 with increasing quench depth to lower T_q. The exponent b of the relationship $\Gamma_2 = a \cdot q^b$ is shown in Figure 5.28. The coarsening process of the spinodal decomposition of the IgG model system shows an approximately linear $\Gamma_2 \propto q$ relationship for all T_q.

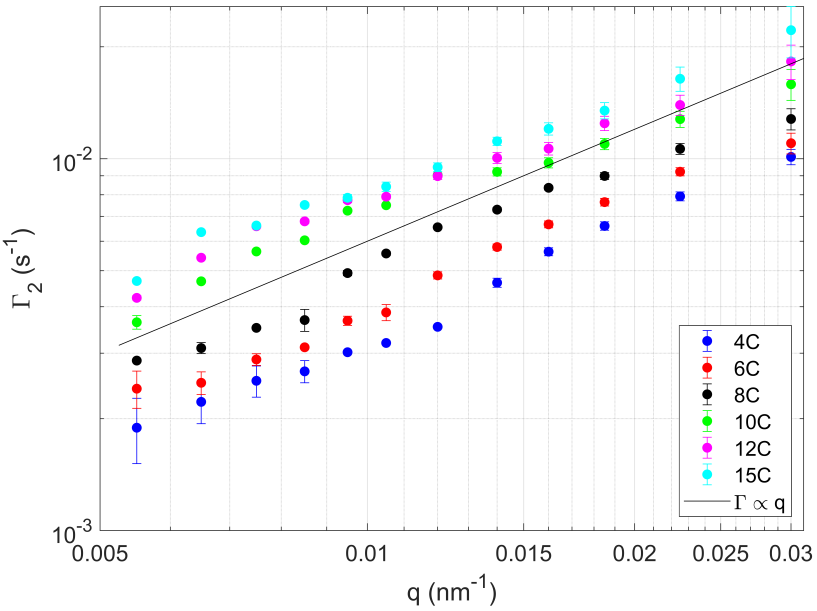

Figure 5.27.: Decay rate Γ_2 in dependence of q for the time interval from $t_w = 220\,\mathrm{s}$ to $t_w = 460\,\mathrm{s}$. The black line marks a linear $\Gamma_2 \propto q$ relationship.

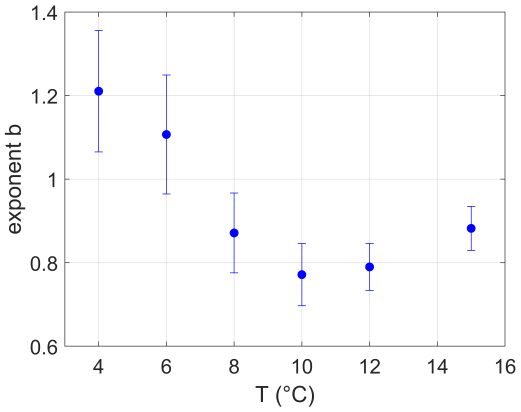

Figure 5.28.: Exponent b describing the relationship $\Gamma_2 = a \cdot q^b$ for the different quench temperatures T_q.

Figure 5.29 shows the KWW exponent γ_2 of the correlation function averaged over the time interval from $t_w = 220\,\mathrm{s}$ to $t_w = 460\,\mathrm{s}$. During this coarsening stage γ_2 shows a clear

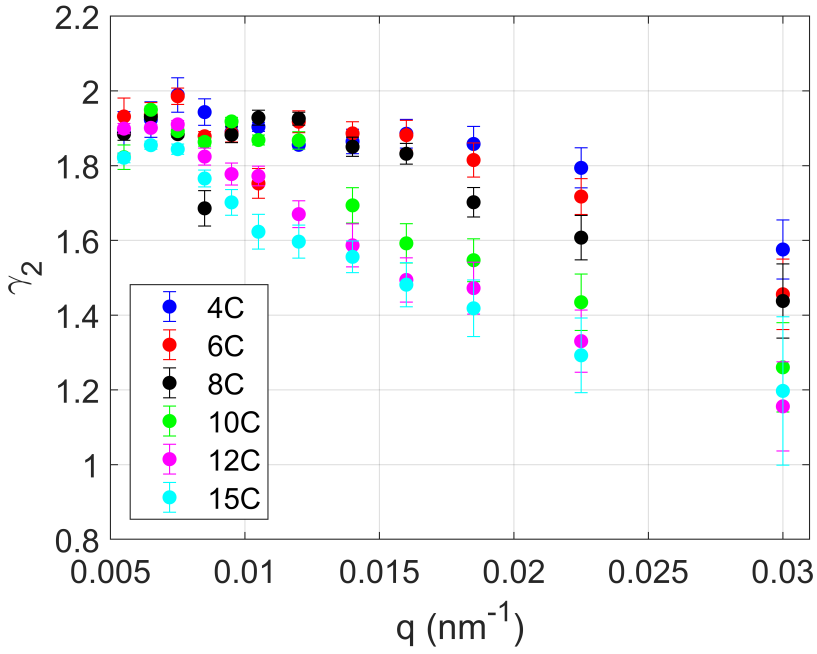

Figure 5.29.: KWW exponent γ_2 as a function of q for the time interval from $t_w = 220\,\mathrm{s}$ to $t_w = 460\,\mathrm{s}$.

q relationship, decreasing from values arround $\gamma_2 = 2$ at $q = 0.0055\,\mathrm{nm}^{-1}$ to $\gamma_2 = 1.2$ at $q = 0.03\,\mathrm{nm}^{-1}$.

5.3.3. USAXS data discussion

The discussion of the USAXS measurement results is divided into three sections. First, the kinetic results are discussed. Afterwards the three stages of LLPS dynamics are presented. Finally, the results are discussed in the context of gel transition and spinodal decomposition.

When considering the sample kinetics for all quench temperatures T_q a peak in the USAXS profile was observed which starts to grow with the beginning of the LLPS process. This characteristic peak increases in height and shifts to lower q showing the growth of the protein domains [21]. From the peak position the characteristic length ξ of the protein domains can be calculated. This characteristic length ξ shows a power law behaviour for growth which is given by

$$\xi \propto t^{\frac{1}{d}}, \tag{5.9}$$

where d is the dimensionality of the system. For $T_q = 15\,^{\circ}\mathrm{C}$ the exponent $b = 0.33 \pm 0.01$ was calculated corresponding to the dimensionality $d = 3$, which is known from diffusive growth in the three-dimensional space in the case of a classical spinodal decomposition [23]. For deeper quenches the determined exponent is decreasing.

Also the peak intensity is decreasing with increasing quench depth due to the scattering contrast between the two phases becomes lower [37]. In Figure 5.30 the binodal of the system is presented showing a glass line which is moving to lower concentrations for deeper quench temperatures. Reaching this glass line the sample shows viscoelastic properties [93], which decrease the movement of the particles.

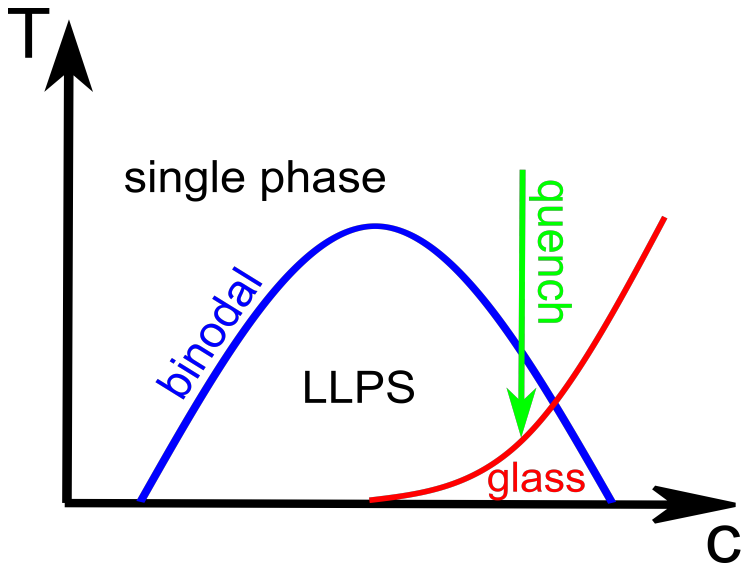

Figure 5.30.: Binodal of the system as a function of the Temperature T and the concentration c. The green arrow marks the quench process.

For the quench to $T_q = 4\,^\circ\mathrm{C}$ the characteristic length ξ increases during the initial stage and remains almost constant with a small growth exponent of $b = 0.024 \pm 0.001$. Here, the domains grow to some finite size where they stop to grow by gelation [86].

Three stages of dynamics during the LLPS of the IgG model system are identified:

- During the early stage of the LLPS up to $t_w \approx 20\,\mathrm{s}$ a fast relaxation mode was observed. These early dynamics of the IgG model system LLPS show an exponential increase of the decorrelation time τ_1 and become faster with deeper quenches. This process can be identified as the interface formation during the LLPS process [35] and is triggered by the density fluctuations of wavelength Λ around the initial volume fraction ϕ_0 [37]. The dynamics are driven by the second derivative of the free energy $\frac{\partial^2}{\partial c^2} F$, which increases in magnitude with increasing quench depth. This temperature behaviour showing faster dynamics for deeper quenches is in agreement with the ordinary linearized Cahn-Hillard equation (CHE) [86]. However, in contrast to the predictions of the linearized CHE a linear

  $$\Gamma_1 \propto q \tag{5.10}$$

  relationship and KKW exponents $\gamma_1 > 1$ were found. These observations correspond to superdiffusive ballistic motion and show that the system is not ruled by thermal diffusion. This behaviour is not achieved by ordinary CHE, since viscoelastic properties are neglected in the Cahn-Hillard equation.

- The intermediate stage of the LLPS starts after $t_w \approx 20\,\mathrm{s}$ when a second slower relaxation process is arising. During this time interval between $t_w \approx 20\,\mathrm{s}$ to $40\,\mathrm{s}$ the final interface formation driven by the curvature of the free energy and the coarsening process due to an increasing viscosity are observed simultaneously. The increasing non-ergodicity parameter shows that the contribution of this slow coarsening mode becomes dominant with time.

- During the late dynamics after $t_w \approx 40\,\mathrm{s}$ the coarsening process is predominant. For deep quenches the dynamics become very slow with decorrelation times $\tau > 100\,\mathrm{s}$. This slow process can be identified as heterogeneous ballistic motion of the domains themselves due to interfacial coarsening [35]. The dynamics show a reverse temperature behaviour compared to the early dynamics. Due to influence of the glass line the viscosity increases for low temperatures which lead to a slowdown of the dynamics. For coarsening dynamics a linear $\Gamma_1 \propto q$ relationship and KKW exponents $\gamma_2 > 1$ were observed. Thus, this stage is also ruled by superdiffusive ballistic motion.

The dynamics of the IgG model system show several properties which were also observed during investigations of colloidal gel transitions. Cipiletti et al. [21] propose a suitable model of gel formation by aggregation of colloids in which the gel contracts in a heterogeneous way:
They propose that the gel shrinks locally and its inhomogeneities result in random regions of higher deformation. Because the gel is elastic a displacement field around each of these deformations is formed. Each inhomogeneity due to localized microcollapses of the structure appearing randomly in space and time acts as a force dipole creating an elastic long-range deformation field. The displacement field ΔR in a distance r from an inhomogeneity is given by

$$\Delta R \propto \frac{\alpha t}{r^2}, \tag{5.11}$$

where α is the strain rate. Due to the force dipole behaviour of the inhomogeneities the displacement field ΔR decreases with $\frac{1}{r^2}$. The effect of ΔR on the correlation function can be determined from the fraction of particles in the gel for which the displacement ΔR is less than q^{-1} leading to the dynamic structure factor

$$f(q,t) \propto \exp(-\Gamma t)^{1.5}, \tag{5.12}$$

which shows a linear

$$\Gamma \propto q \tag{5.13}$$

relationship and a compressed KWW exponent $\gamma = 1.5$ [21].
This gel like dynamics with a linear $\Gamma \propto q$ relationship and compressed KWW $\gamma \approx 1.5$ were also found in other soft matter systems [3, 7] for example in laponite [60], colloidal silica nanoparticles in propanediol [19] and metallic glasses [100]. For the late gel transition a power law behaviour of the decorrelation time τ was observed justified by the fact that the energy barrier for rearrangement events bringing the particles closer together in a strained region is increased and these regions find it harder to collapse subsequently [13]. The local sample environment becomes stiffer with time making subsequent rearrangement events harder [52]. Duri et al. [30] reported that these rearrangement events correspond to the breaking of bonds and the formation of new bonds along the gel network.

This knowledge about the gel transition shall now be brought into the context of spinodal decomposition:
Gao et al. demonstrated an arrested spinodal decomposition as the mechanism of gelation in an oil-in-water nanoemulsion colloidal system [35]. The resulting gel state shows dynamics on two distinct length scales: A slow correlation corresponding to dynamics of phase separated domains and fast dynamics caused by motion of nearest neighbour particles (see SAXS data in Section 5.4). Gao et al. also found a linear $\Gamma \propto q$ relationship

indicating ballistic dynamics and compressed KWW exponents asymptoting to $\gamma \approx 2$ for small q and decaying to $\gamma \approx 1$ for larger q. These observations are in agreement with the coarsening dynamics of the IgG model system which show a KWW exponent as a function of q, decreasing from values around $\gamma_2 = 2$ at $q = 0.0055\,\mathrm{nm}^{-1}$ to $\gamma_2 = 1.2$ at $q = 0.03\,\mathrm{nm}^{-1}$.

To understand the reserved temperature dependence of the coarsening mode the ordinary Cahn-Hillard equation is not sufficient. Here the concept of an arrested phase transition is required, where an attractive glass transition intersects the colloid-rich side of the binodal [35]. This glass transition can be modelled by a rapid decrease of the mobility coefficient with increasing concentration of the glass-forming component [81].
Sciortino et al. [86] coupled phase separation and gelation in their model. The evolution of the concentration during a classical spinodal decomposition is described by the Cahn-Hillard equation [16, 17]

$$\frac{\partial \psi}{\partial t} = \nabla \cdot M_\psi \nabla \left(\nabla^2 \psi + \epsilon \psi - \psi^3 \right), \tag{5.14}$$

where ψ is the order parameter related to the local concentration $\phi = \frac{\psi+1}{2}$, $\epsilon = \frac{T_c - T}{T_c}$ is the reduced temperature with the critical temperature T_c and M_ψ is the mobility, which assumed to be constant in conventional treatments [11]. The gel transition is described by

$$\frac{\partial c}{\partial t} = M_c \left(gc - c^2 \right) \tag{5.15}$$

where $c = c(T, \phi)$ is the gel concentration and the parameter g defines the gel line. The gelation mobility M_c is assumed to decrease dramatically in those regions where the gel concentration c becomes nonzero. Finally, the coupling of gelation and phase transition can be implemented [86] by a gel concentration c dependent mobility

$$M_\psi(c) = \exp\left(-\frac{c}{c_0} \right) \tag{5.16}$$

with $c_0 << 1$.

Anita Girelli performed numerical simulations for the IgG model system using the Cahn-Hillard equation with a concentration dependent mobility. Her simulations show the characteristic reserved temperature dependence of the coarsening stage. She will publish the results in detail in her PhD thesis and in [40].

5.4. SAXS data

Measurements in SAXS geometry were performed to investigate the IgG model system LLPS at large q values up to $q = 1\,\mathrm{nm}^{-1}$ on single protein length scale. Figure 5.31 shows the q dependent X-ray scattering intensity I_{saxs} in counts per pixel per second. The area on the detector corresponding to $q < 0.025\,\mathrm{nm}^{-1}$ is covered by the beamstop. For the lowest q accessible in SAXS setup 100 counts per pixel per second were collected. The SAXS analysis starts at the q value, where the results of a single measurement in USAXS setup became noisy (see Figure 5.26). As shown in Figure 5.31 I_{saxs} is dropping by four orders of magnitude with increasing q up to $q = 1\,\mathrm{nm}^{-1}$. This intensity is not sufficient to obtain correlation functions with an sufficient SNR by measuring one XPCS series respecting the critical X-ray dose D_c. To improve the SNR the number of repetitions N_{rep} can be increased (see eq. (2.34)).

Therefore 120 measurements were collected and merged to reach an sufficient high SNR.

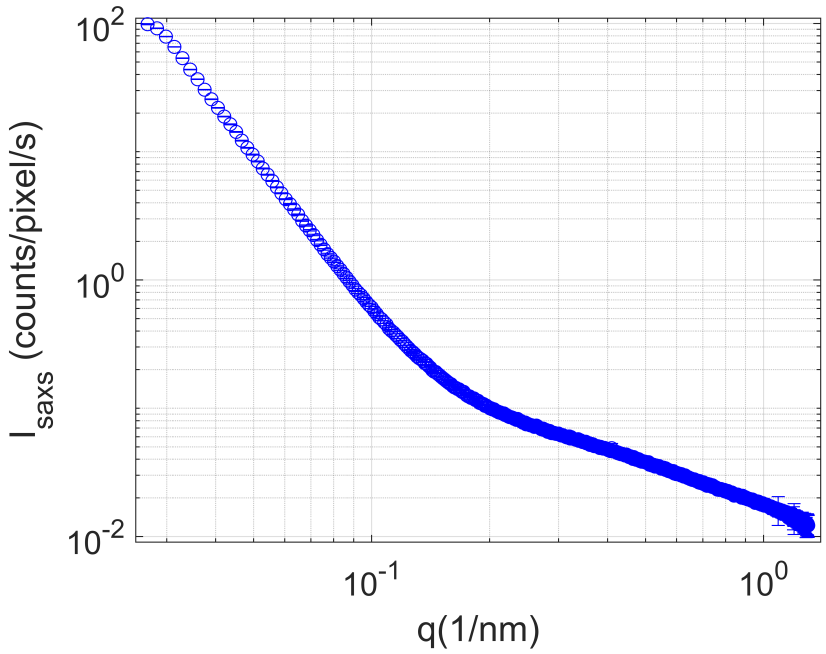

Figure 5.31.: SAXS intensity I_{saxs} in dependence of q after a quench of the IgG model system from $T_q = 37\,^\circ\mathrm{C}$ to $T_q = -5\,^\circ\mathrm{C}$.

The IgG model system was quenched to $T_q = -5\,^\circ\mathrm{C}$ and the measurements were started after $t_w = 10\,\mathrm{min}$ to be sure that the arrested state is reached. Each measurement was recorded at a fresh sample spot. To obtain correlation functions over several orders of magnitude in time, measurements were collected with a total measurement time of 4 s and 300 s. The measurement parameters are presented in table 4.3. The correlation functions for 17 q values were calculated and merged using Xana.

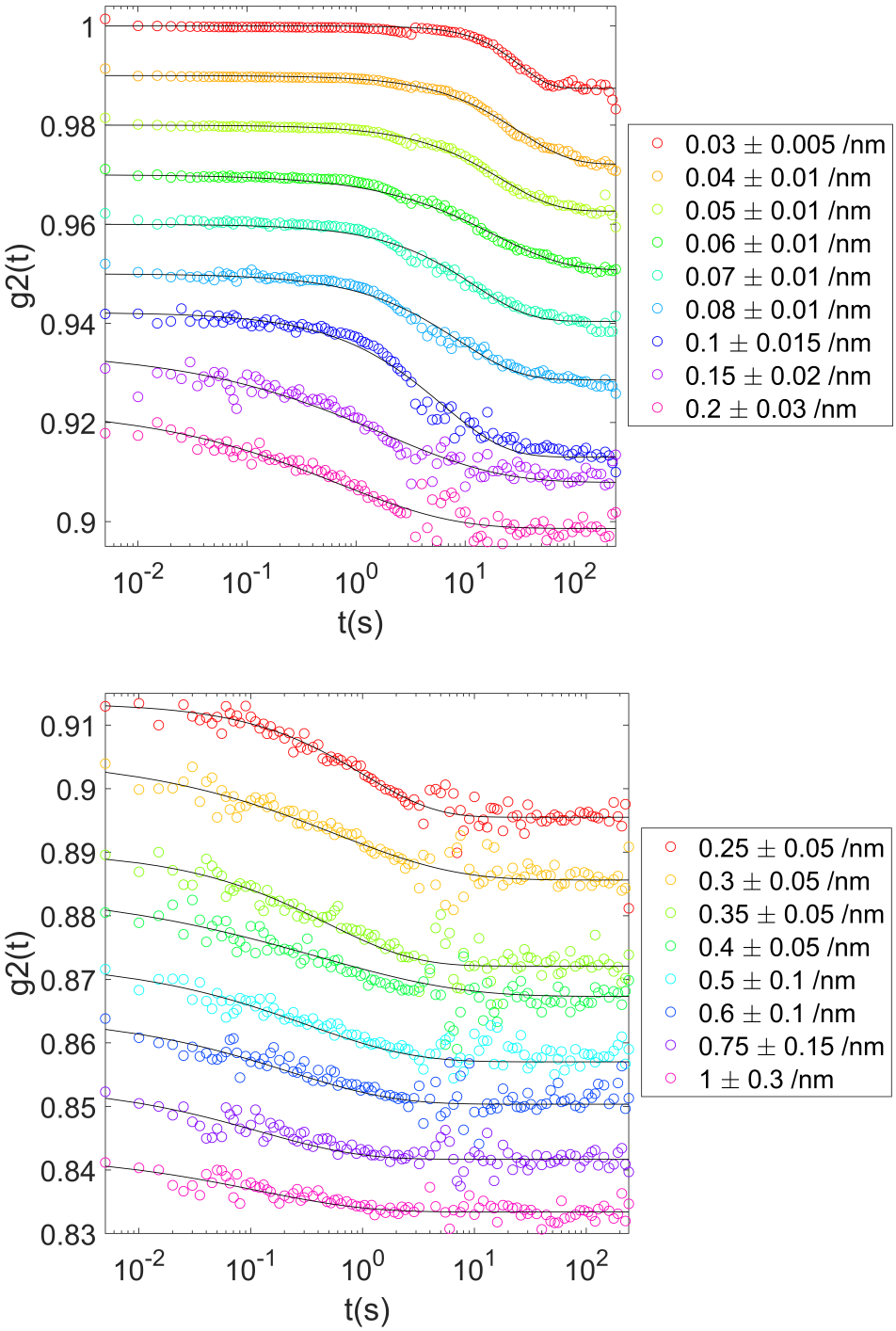

Figure 5.32.: Correlation functions after a quench of the IgG model system from $T = 37\,^{\circ}\mathrm{C}$ to $T_q = -5\,^{\circ}\mathrm{C}$. For clarity of the figure, the individual correlation functions were shifted. The black lines mark the fitted g2 functions.

Then the correlation functions measured on both time scales were stitched together. In Figure 5.32 the merged correlation functions up to $q = 1\,\mathrm{nm}^{-1}$ are shown. Due to recording the data after $t_w = 10\,\mathrm{min}$ only the slow coarsening process is visible and the dynamical parameter can be determined using one exponential fits

$$g_2(\vec{q},\tau) = a + \beta_2 \exp\left(-2\left(\Gamma_2\tau\right)^{\gamma_2}\right), \tag{5.17}$$

which are marked by black lines in Figure 5.32. At $q > 0.1\,\mathrm{nm}^{-1}$ the decorrelation starts on a time scale faster than 10 ms. This means that the upper baseline of the correlation function is not displayed by the XPCS measurements, making it difficult to fit the contrast β_2. Therefore, a theoretical contrast (see [72]) depending on the q value and the setup parameter was determined and used to fit the correlation functions.

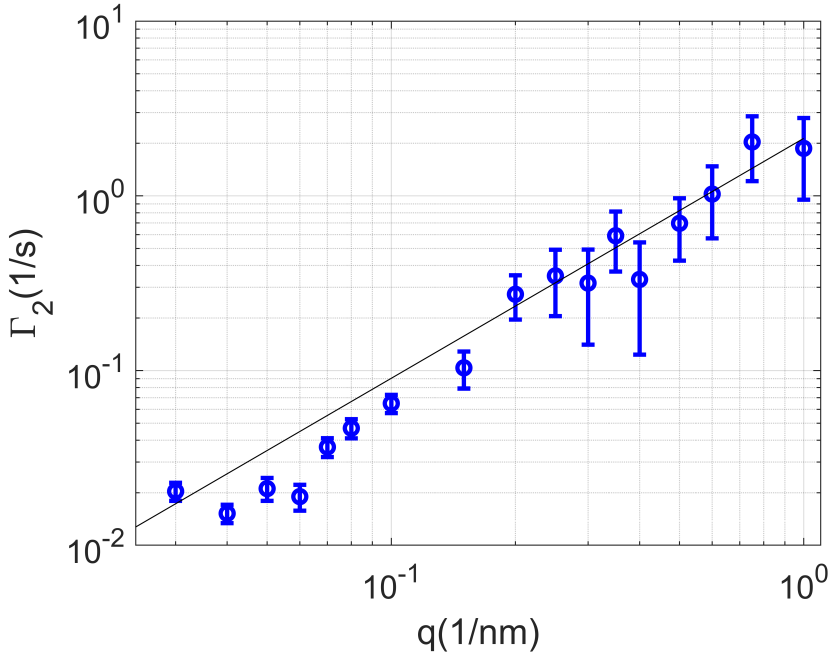

Figure 5.33.: Decay rate Γ_2 in dependence of q measured after a quench of the IgG model system from $T = 37\,^\circ\mathrm{C}$ to $T_q = -5\,^\circ\mathrm{C}$.

The fitted decay rate Γ_2 as a function of q is shown in Figure 5.33. The black line corresponds to the determined

$$\Gamma = (2.13 \pm 0.36) \cdot q^{1.37\pm0.34}. \tag{5.18}$$

relationship. While the dynamics are arrested on the protein droplet length scale, however on single protein length scale $\Gamma_2 > 1$ were determined, which correspond to decorrelation times faster than 1 s.

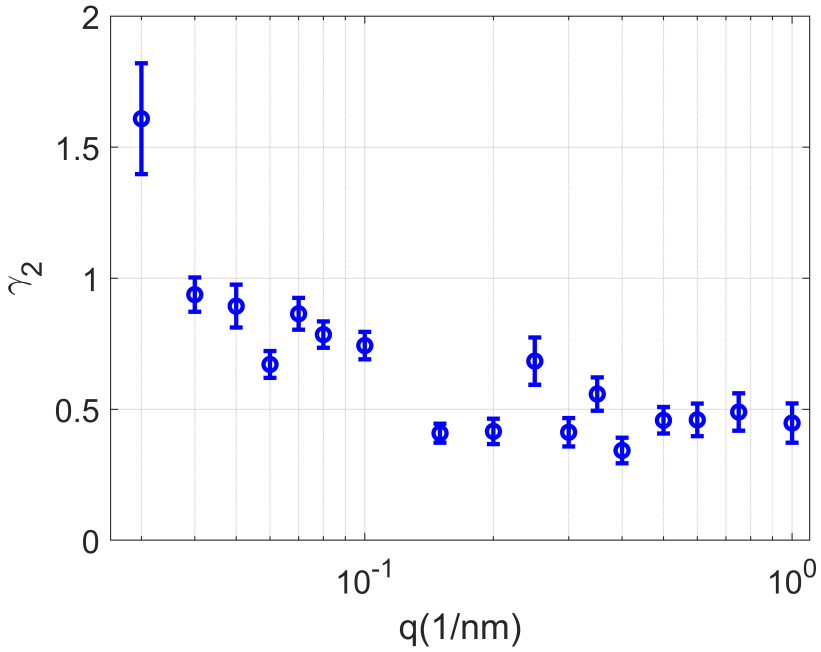

Figure 5.34.: KWW exponent γ_2 in dependence of q measured after a quench of the IgG model system from $T = 37\,°\mathrm{C}$ to $T_q = -5\,°\mathrm{C}$.

As shown in Figure 5.33, the KKW exponent is decreasing with q to values around 0.5.

5.4.1. SAXS data discussion

The feasibility to reach a sufficient high SNR for the calculation of correlation functions up to $q = 1\,\mathrm{nm}^{-1}$ which correspond to the length scale of single proteins was demonstrated. Therefore, several XPCS measurements recorded at different sample spots were merged. For the IgG model system dynamics with a decorrelation time τ faster than 1 s were measured, even though the sample is arrested on the length scale of protein droplets. This fast process can be identified as the fluctuations of particle clusters within the protein rich domains.

Considering the decay rate Γ_2 as a function of q, a subquadratic relationship was determined also on the nanometer length scale. Consequently, the dynamics on the length scale of single proteins are not ruled by Brownian motion. Ruta et al. found a similar anomalous mechanism of diffusion in supercooled metallic liquids [80]. This anomalous behaviour has an impact on the transport mechanism in the cell. The mean squared displacement Δx^2 is given by

$$\Delta x^2 \propto \Gamma_t t^{\alpha}, \tag{5.19}$$

where Γ_t is the transport coefficient and α is the anomalous diffusion exponent. For Brownian motion the particles are moving independent of each other leading to $\alpha = 1$. In the assumption of spatial restrictions the mean squared displacement (MSD) decreases and the time to achieve a diffusion distance becomes longer [41]. In this case, which is applicable for a crowded environment in the cell the anomalous diffusion exponent decreases to $\alpha < 1$ reducing the time dependence of the MSD.

The measured correlation functions at large q show stretched KWW exponents $\gamma_2 \approx 0.5$ indicating highly heterogeneous dynamics [39]. The gel network of protein rich domains can be considered as a cage which restricts the protein dynamics [4]. To understand these highly heterogeneous dynamics the limit of the colloid approach to protein solutions has to be considered [92].
Bucciarelli et al. performed simulations for the eye lens protein γ_B-crystallin including thermal fluctuations and hydrodynamic interactions. Considering the effect of anisotropic interactions they modelled patch-patch interactions with a short-range attractive pair potential. In the crowded environment of the cell patchy attractions lead to the formation of temporary protein clusters which strongly differ in their size and structure. The lifetime of the bonds creating the temporary protein clusters was estimated with 200 ns [14]. From their simulations Bucciarelli et al. calculated intermediate scattering functions with a stretched exponential behaviour corresponding to highly heterogeneous dynamics of the temporary protein clusters with different dynamical properties.

Thus, we conclude that details of the protein interaction are important for understanding and predicting the dynamic properties at large q values. Our results can serve as experimental benchmark for future theory and simulation efforts in describing interactions and dynamics in crowded environments.

6. Conclusion and Outlook

This thesis demonstrated the feasibility of Bio-XPCS measurements to investigate protein dynamics during a liquid-liquid phase separation on a hierarchy of length scales from droplet sizes in the region of micrometers down to the single protein on the nanometer scale.

For the realization of the Bio-XPCS measurements, experimental parameters and the measurement protocol were optimized with the idea to reduce the photon density while keeping a high signal-to-noise ratio. Therefore, in the USAXS setup at the P10 coherence application beamline the beam size was increased to $100 \times 100\,\mu\mathrm{m}^2$ and a large sample-to-detector distance of 21.2 m was used to resolve the speckles. A protein model system composed of γ-globulin (IgG) in presence of polyethylene glycol (PEG) was chosen to study the dynamics during the LLPS. First, static USAXS and SAXS measurements were recorded to determine the critical dose D_c after which the IgG model system starts to degrade due to radiation damage. Therefore, the ratio of the intensity F_{I0} was calculated which shows no increase until D_c is reached. In the USAXS setup the the critical dose was determined to be $D_c \approx 5\,\mathrm{kGy}$ and in the SAXS setup $D_c \approx 7.5$ to 10 kGy was determined.

The following challenge was to reach a sufficient high SNR to record correlation functions using XPCS while keeping D_c. In the USAXS setup the approach using a large beam size led to XPCS series recorded with a dose of 5 kGy which were appropriate to extract dynamical information. In the SAXS setup the low speckle contrast at high q and the four orders of magnitude lower scattering intensity required another measurement protocol to reveal the dynamics. Several correlation functions were collected at different sample spots. Merging these correlation functions led to a sufficiently high SNR to extract the dynamics. This was the first successful XPCS experiment investigating the protein dynamics on the nanometer length scales.

During measuring the LLPS of the IgG model system different stages of dynamics were identified.
On the protein domain length scale a fast relaxation during the early stage of the phase separation up to a waiting time $t_w \approx 40\,\mathrm{s}$ was found. This relaxation was identified as the interface formation driven by the curvature of the free energy, which is increasing with the

quench depth resulting in faster dynamics at lower quench temperatures. After $t_w \approx 20\,\mathrm{s}$ a second slow relaxation sets in which corresponds to heterogeneous ballistic motion of the protein domains due to interfacial coarsening. Both processes are observed simultaneously between $t_w \approx 20\,\mathrm{s}$ to $40\,\mathrm{s}$ with an increasing non-ergodicity parameter. Superdiffusive ballistic dynamics known from a gel transition were identified by measuring a linear $\Gamma \propto q$ relationship and compressed KWW exponents. For the coarsening relaxation mode a reserve temperature behaviour was observed showing an increase of the decorrelation time for deeper quenches.

On the length scale of single proteins the sample shows highly heterogeneous dynamics indicated by stretched KWW exponents which correspond to fluctuations of particle clusters within the protein rich domains. Furthermore a subquadratic $\Gamma \propto q$ relationship was found identifying an anomalous diffusion transport on this nanometer length scale.

The methods developed in this thesis are the entry for more research on the field of crowded proteins by XPCS. The measurement strategies can be used for Bio-XPCS measurements at new X-ray sources to reveal dynamics on time scales from femtoseconds to hours and a hierarchy of length scales from droplet size down to the nanometer scale. The IgG model system was chosen because the kinetics were already known and the samples were relatively inexpensive to produce. In the next step, biologically more relevant but also more expensive samples can be investigated. Monoclonal antibodies (mAb) are considered as a major platform for potential drug candidates [92]. Currently a key problem in antibody formulation is that mAbs can exhibit enhanced self-association, causing viscosities too high for administering the drug. Monoclonal antibodies are also known to exhibit high turbidity due to the presence of liquid–liquid phase separation [92]. Thus, XPCS is a suitable method to investigate this type of proteins. Furthermore, Bio-XPCS at the new X-ray sources can be a major step in the investigation of protein condensation diseases.

A. Appendix

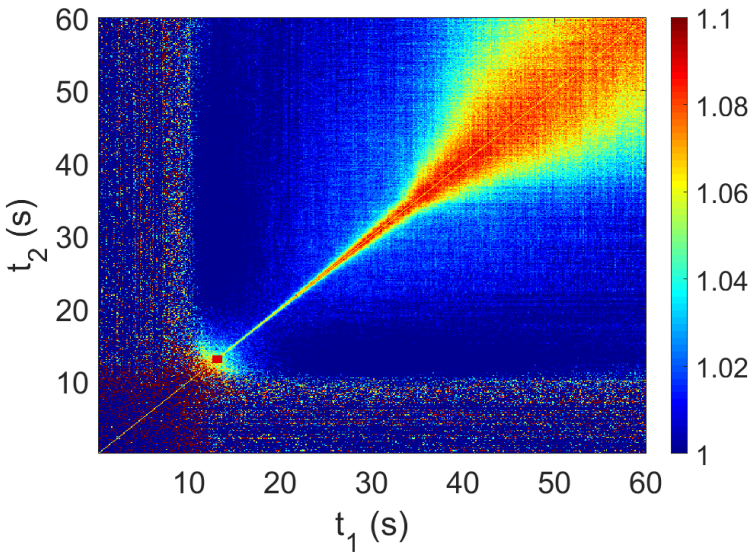

Figure A.1.: Two time correlation function of the measurement during a quench from $T = 37\,°\mathrm{C}$ to $T_q = 15\,°\mathrm{C}$. The red square marks the time $t = 13\,\mathrm{s}$ when $T_q = 15\,°\mathrm{C}$ is reached.

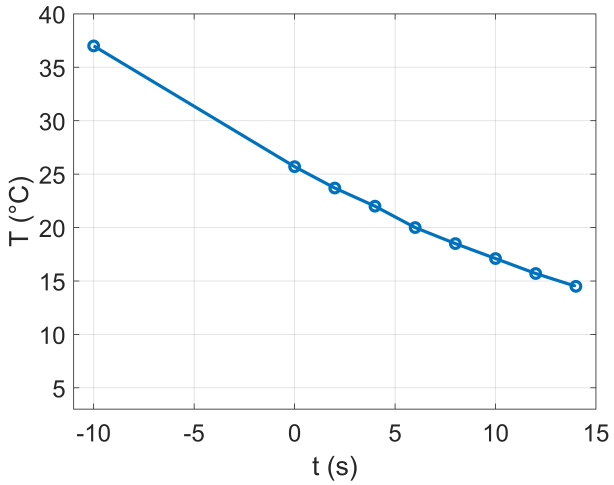

$t(s)$	$T(°C)$
-10	37
0	25.7
2	23.7
4	22
6	20
8	18.5
10	17.1
12	15.7
14	14.5

Figure A.2.: Temporal evolution of the temperature T during the quench to $T_q = 15\,°\mathrm{C}$. The data points show that the quench process was started $10\,\mathrm{s}$ before the XPCS measurement.

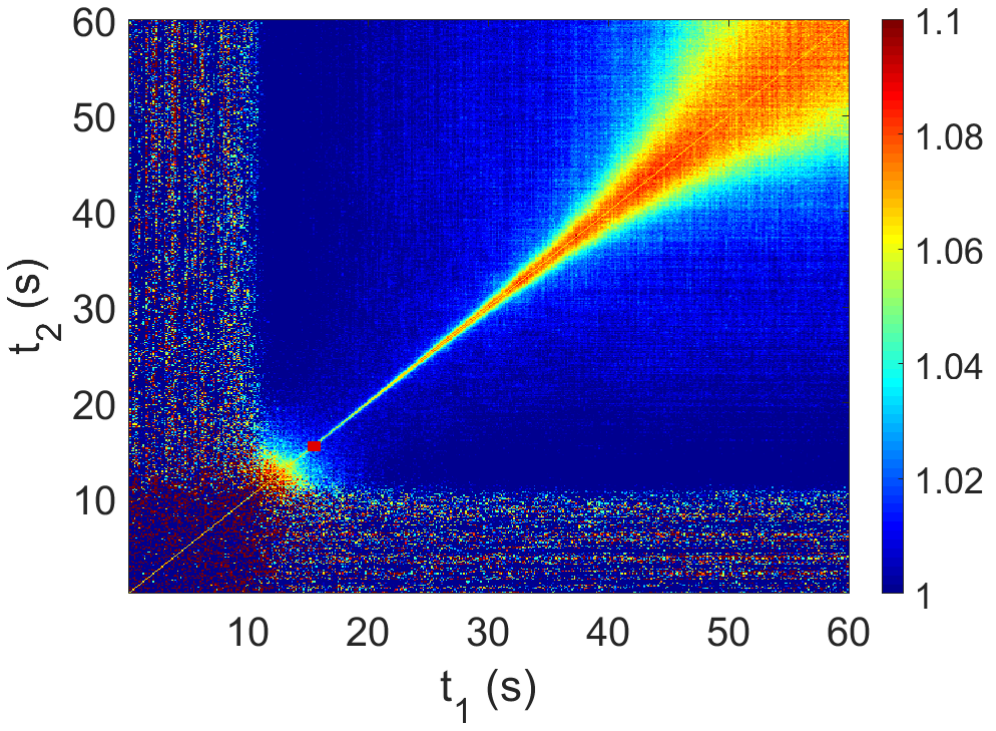

Figure A.3.: Two time correlation function of the measurement during a quench from $T = 37\,°\mathrm{C}$ to $T_q = 12\,°\mathrm{C}$. The red square marks the time $t = 15.5\,\mathrm{s}$ when $T_q = 12\,°\mathrm{C}$ is reached.

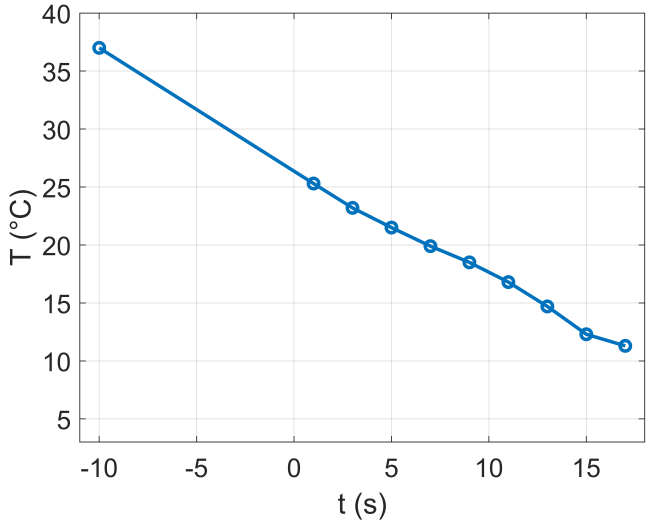

$t(s)$	$T(°C)$
-10	37
1	25.3
3	23.2
5	21.5
7	19.9
9	18.5
11	16.8
13	14.7
15	12.3
17	11.3

Figure A.4.: Temporal evolution of the temperature T during the quench to $T_q = 12\,°\mathrm{C}$. The data points show that the quench process was started 10 s before the XPCS measurement.

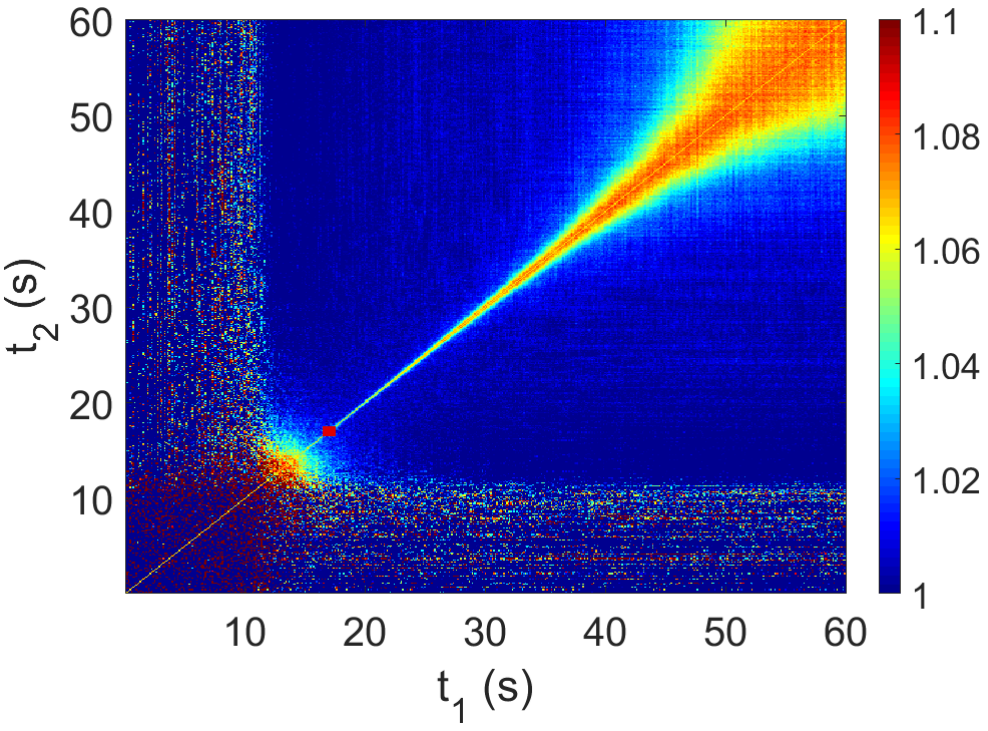

Figure A.5.: Two time correlation function of the measurement during a quench from $T = 37\,°\mathrm{C}$ to $T_q = 10\,°\mathrm{C}$. The red square marks the time $t = 17\,\mathrm{s}$ when $T_q = 10\,°\mathrm{C}$ is reached.

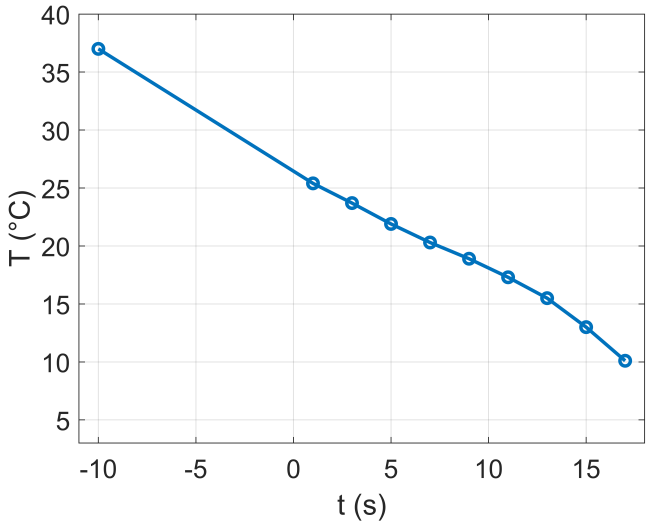

$t(s)$	$T(°C)$
-10	37
1	25.4
3	23.7
5	21.9
7	20.3
9	18.9
11	17.3
13	15.5
15	13
17	10.1

Figure A.6.: Temporal evolution of the temperature T during the quench to $T_q = 10\,°\mathrm{C}$. The data points show that the quench process was started 10 s before the XPCS measurement.

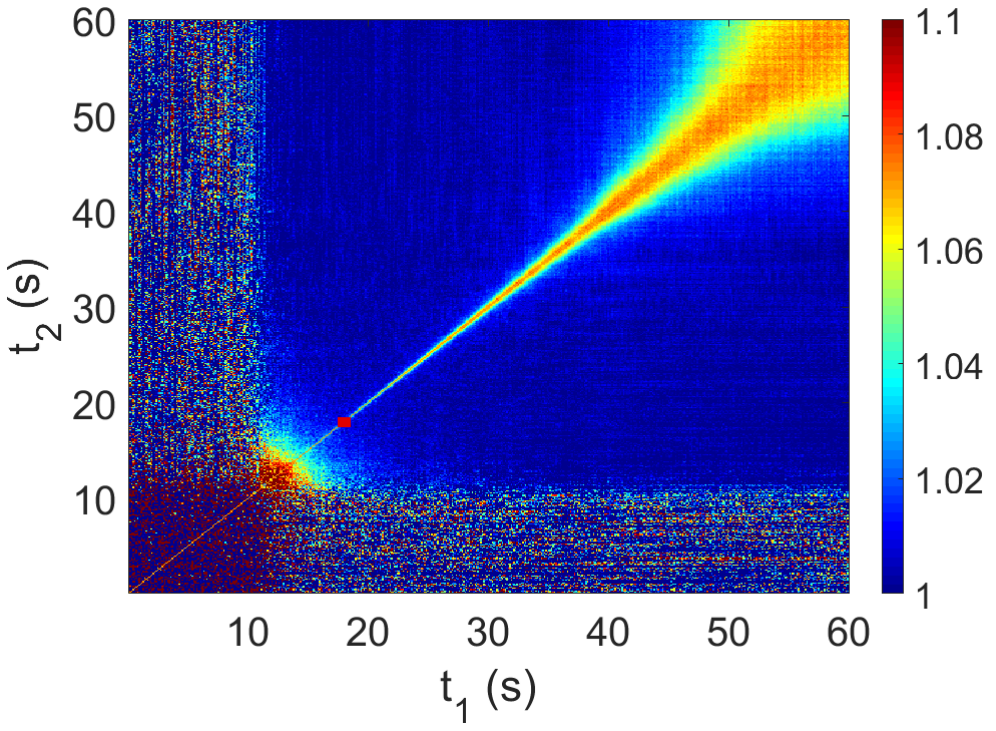

Figure A.7.: Two time correlation function of the measurement during a quench from $T = 37\,°\mathrm{C}$ to $T_q = 8\,°\mathrm{C}$. The red square marks the time $t = 18\,\mathrm{s}$ when $T_q = 8\,°\mathrm{C}$ is reached.

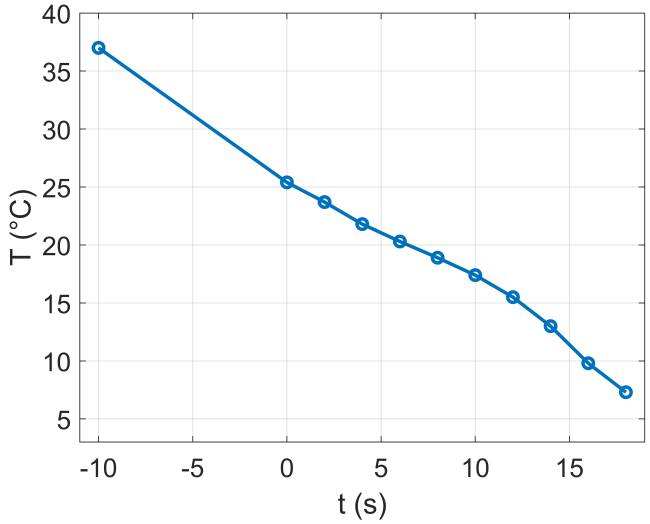

$t(s)$	$T(°C)$
-10	37
0	25.4
2	23.7
4	21.8
6	20.3
8	18.9
10	17.4
12	15.5
14	13
16	9.8
18	7.3

Figure A.8.: Temporal evolution of the temperature T during the quench to $T_q = 8\,°\mathrm{C}$. The data points show that the quench process was started 10 s before the XPCS measurement.

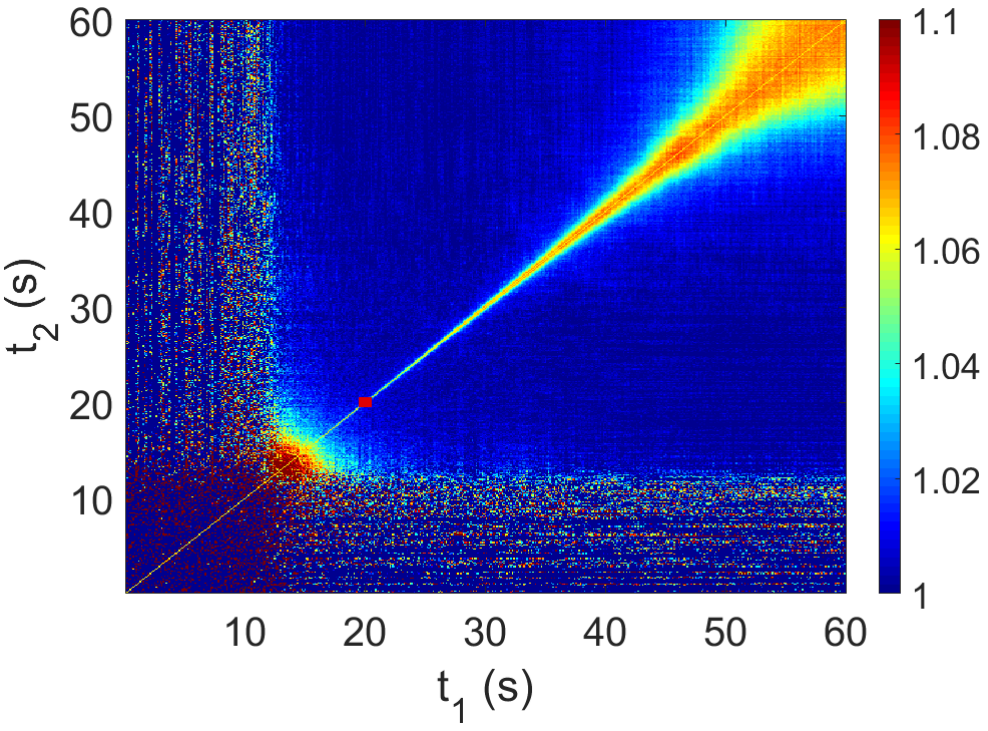

Figure A.9.: Two time correlation function of the measurement during a quench from $T = 37\,°\mathrm{C}$ to $T_q = 6\,°\mathrm{C}$. The red square marks the time $t = 20\,\mathrm{s}$ when $T_q = 6\,°\mathrm{C}$ is reached.

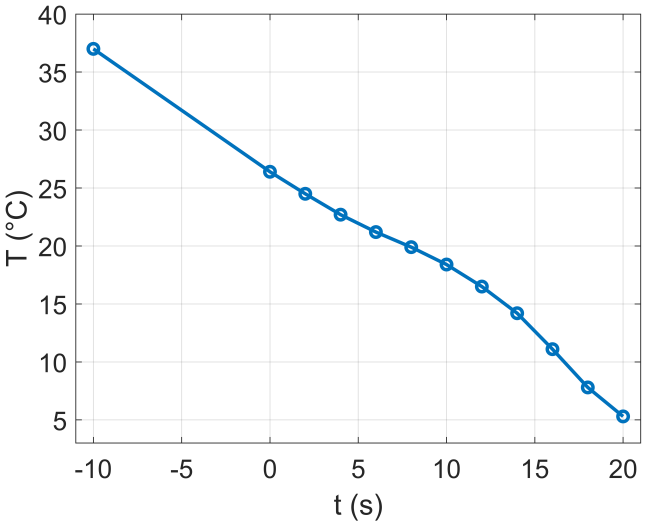

$t(s)$	$T(°C)$
-10	37
0	26.4
2	24.5
4	22.7
6	21.2
8	19.9
10	18.4
12	16.5
14	14.2
16	11.1
18	7.8
20	5.3

Figure A.10.: Temporal evolution of the temperature T during the quench to $T_q = 6\,°\mathrm{C}$. The data points show that the quench process was started 10 s before the XPCS measurement.

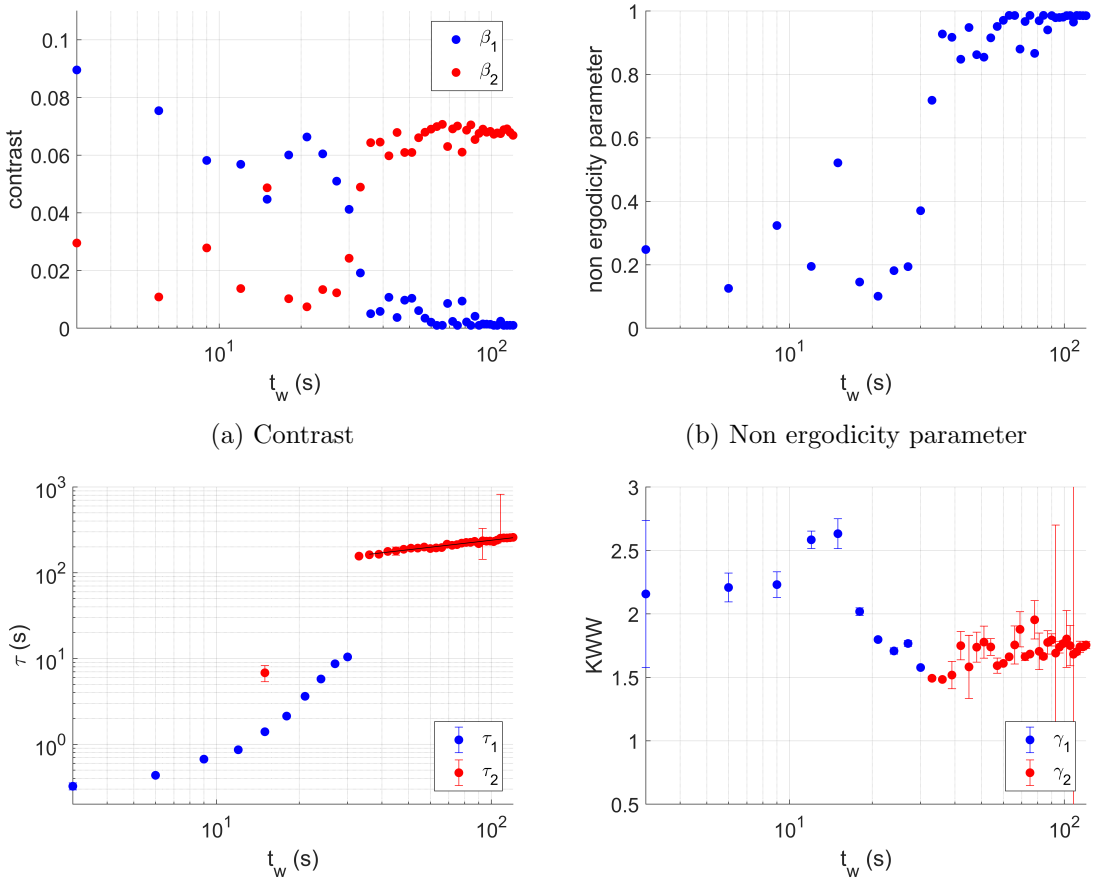

(a) Contrast

(b) Non ergodicity parameter

(c) Decorrelation time

(d) KWW

Figure A.11.: Exponential fit parameter with two dynamical relaxations for the quench to $T_q = 6\,^{\circ}\mathrm{C}$.

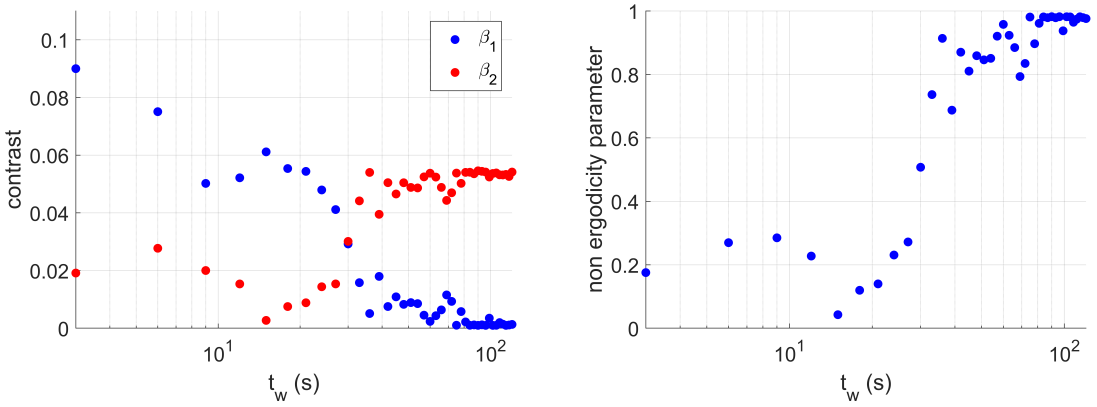

(a) Contrast

(b) Non ergodicity parameter

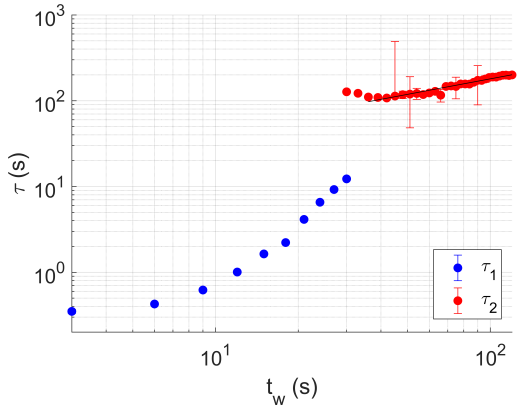

(c) Decorrelation time

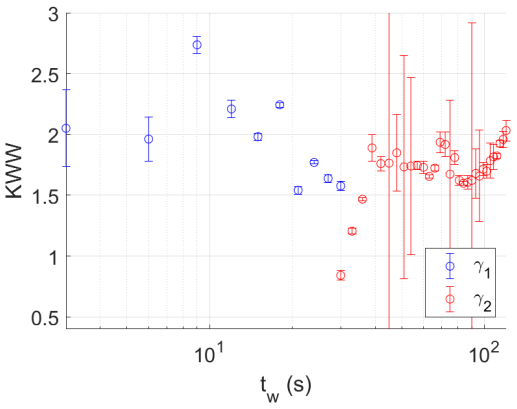

(d) KWW

Figure A.12.: Exponential fit parameter with two dynamical relaxations for the quench to $T_q = 8\,^\circ\mathrm{C}$.

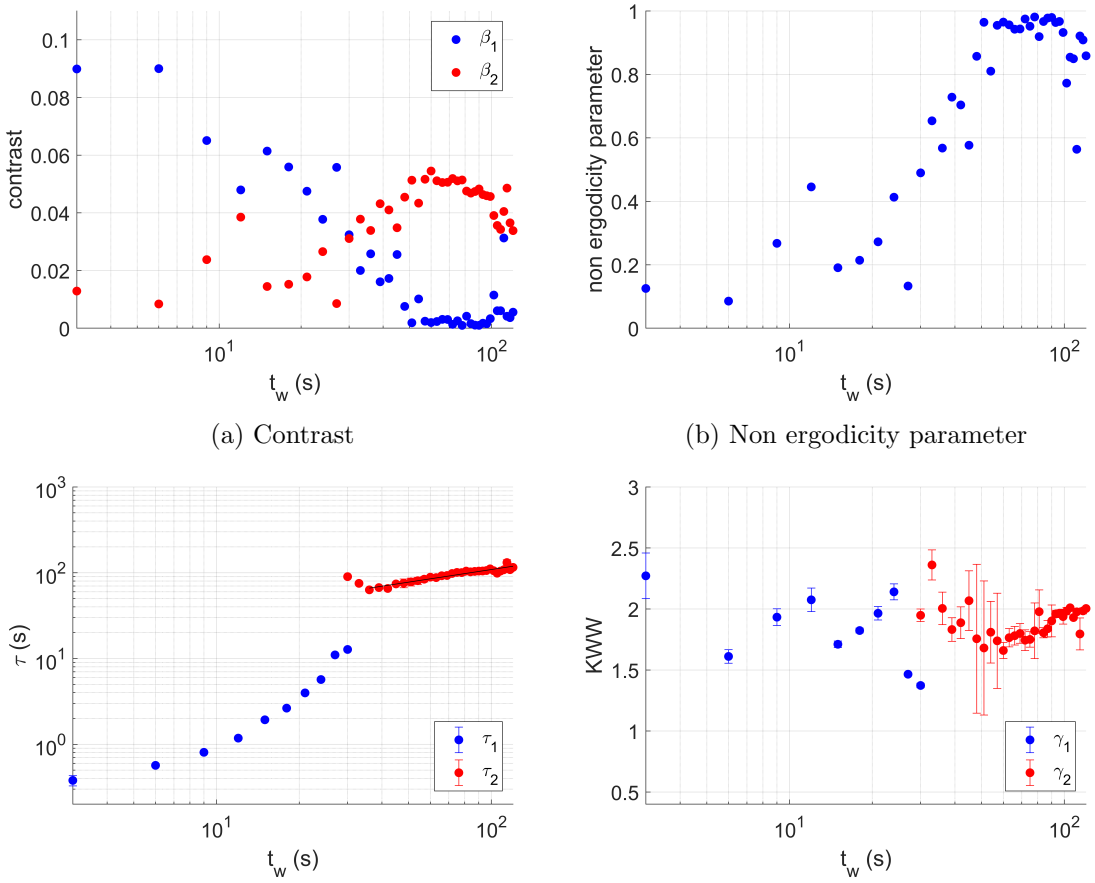

(a) Contrast

(b) Non ergodicity parameter

(c) Decorrelation time

(d) KWW

Figure A.13.: Exponential fit parameter with two dynamical relaxations for the quench to $T_q = 10\,^{\circ}\mathrm{C}$.

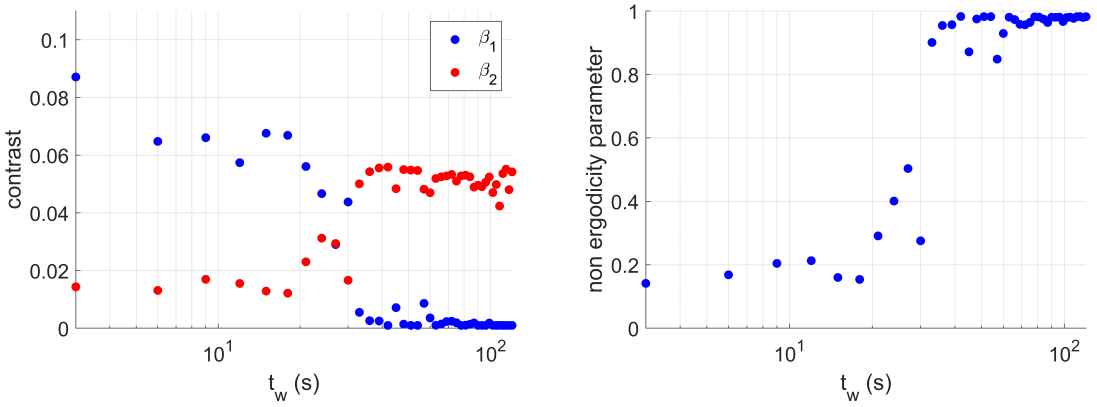

(a) Contrast

(b) Non ergodicity parameter

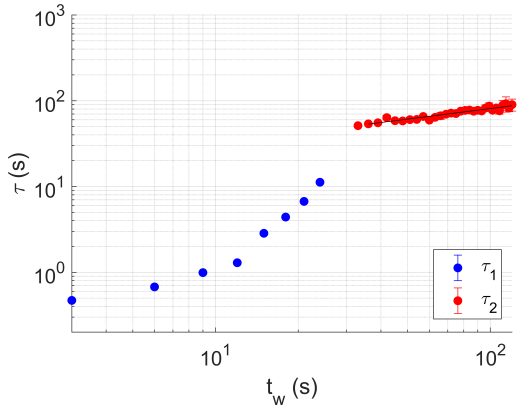

(c) Decorrelation time

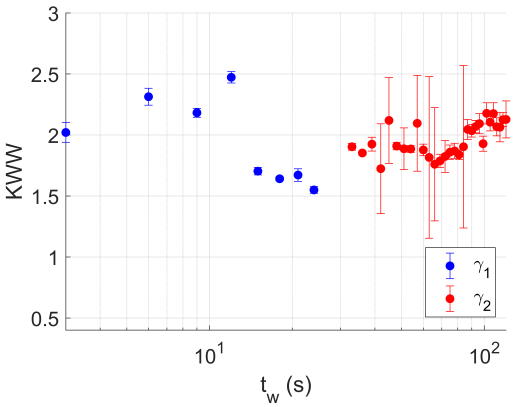

(d) KWW

Figure A.14.: Exponential fit parameter with two dynamical relaxations for the quench to $T_q = 12\,^{\circ}\mathrm{C}$.

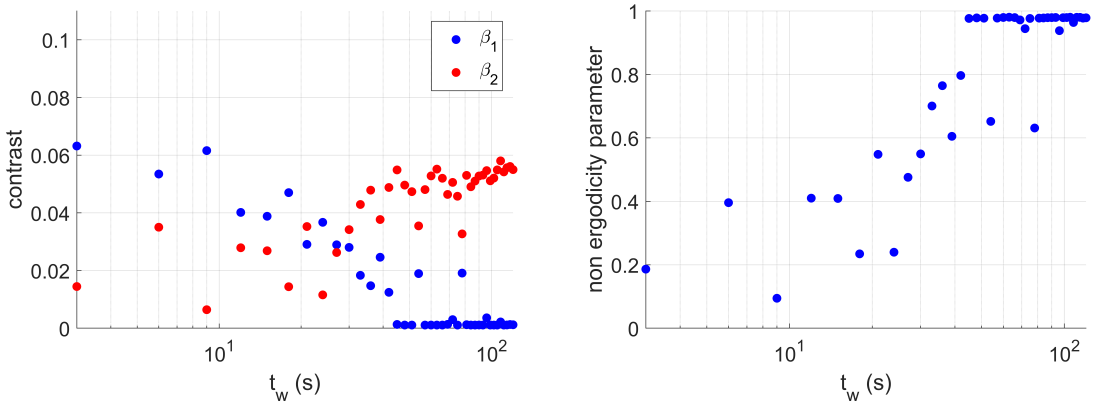

(a) Contrast

(b) Non ergodicity parameter

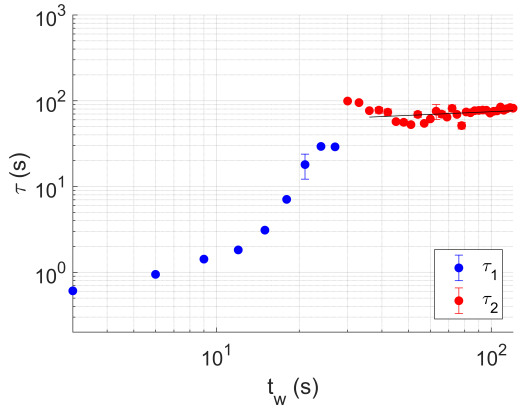

(c) Decorrelation time

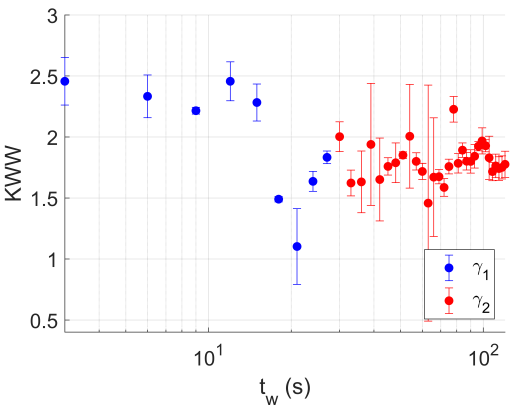

(d) KWW

Figure A.15.: Exponential fit parameter with two dynamical relaxations for the quench to $T_q = 15\,^{\circ}\mathrm{C}$.

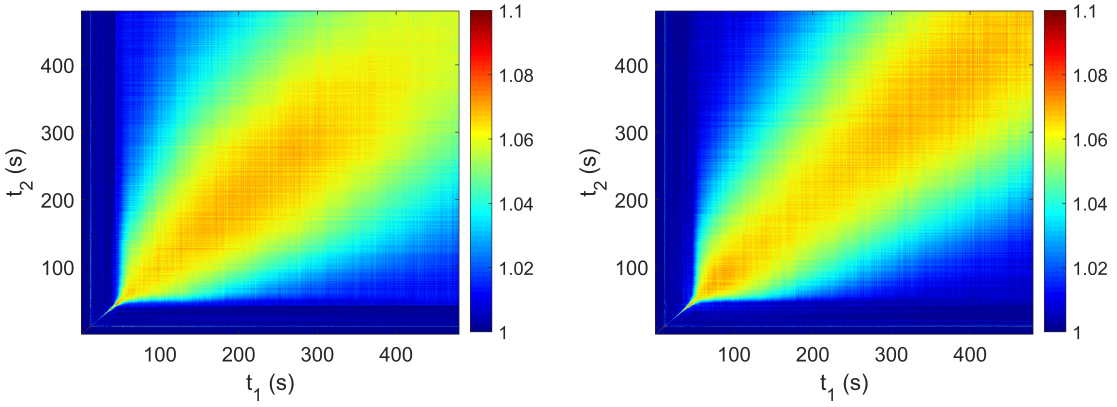

(a) $q = 0.0060\,\mathrm{nm}^{-1}$

(b) $q = 0.0065\,\mathrm{nm}^{-1}$

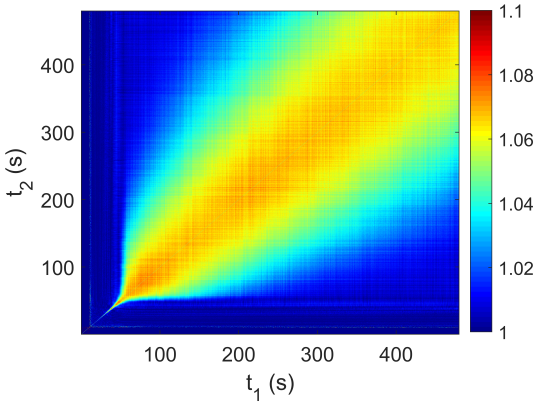

(c) $q = 0.0070\,\mathrm{nm}^{-1}$

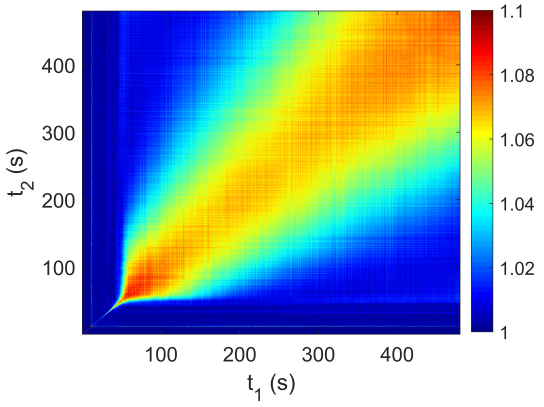

(d) $q = 0.0075\,\mathrm{nm}^{-1}$

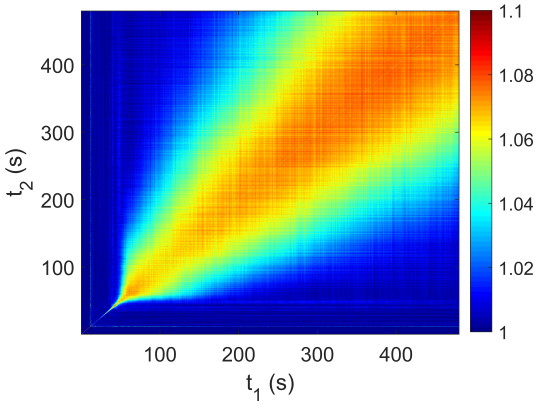

(e) $q = 0.0080\,\mathrm{nm}^{-1}$

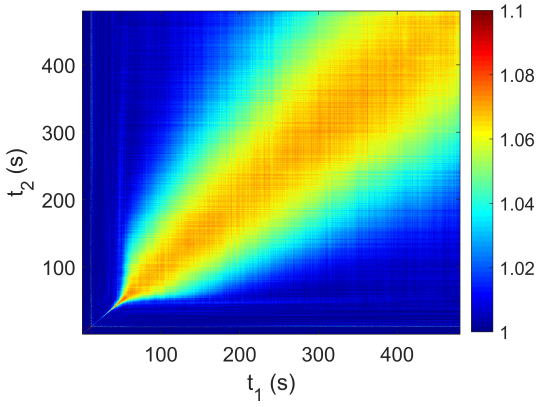

(f) $q = 0.0085\,\mathrm{nm}^{-1}$

Figure A.16.: TTC at different q values for the quench of the IgG model system to $T_q = 4\,^{\circ}\mathrm{C}$.

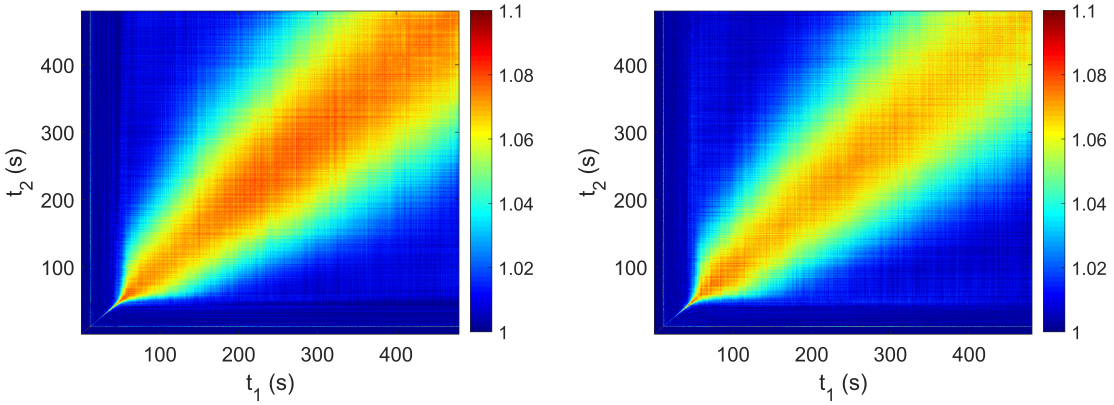

(a) $q = 0.0090\,\mathrm{nm}^{-1}$

(b) $q = 0.0095\,\mathrm{nm}^{-1}$

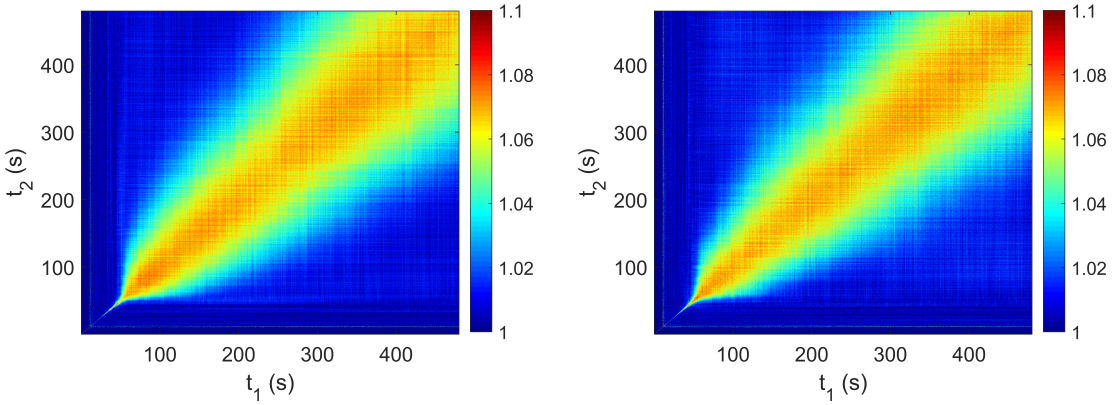

(c) $q = 0.0100\,\mathrm{nm}^{-1}$

(d) $q = 0.0105\,\mathrm{nm}^{-1}$

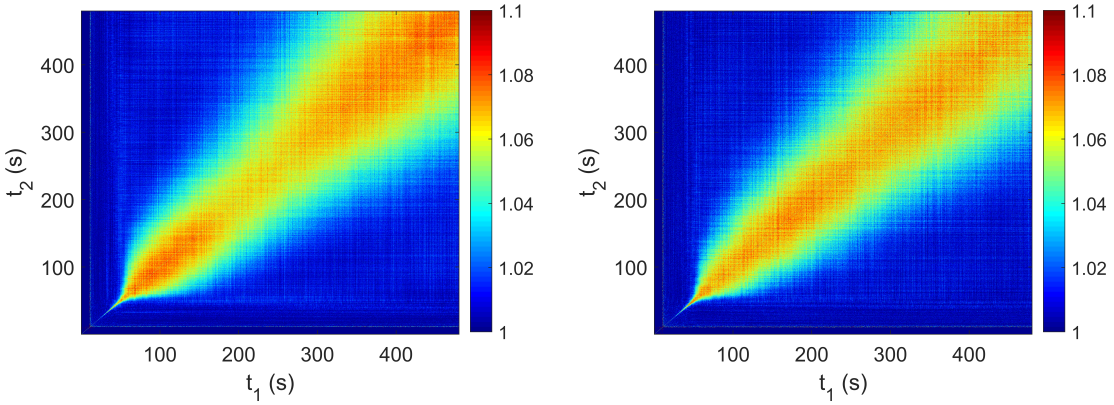

(e) $q = 0.0110\,\mathrm{nm}^{-1}$

(f) $q = 0.0115\,\mathrm{nm}^{-1}$

Figure A.17.: TTC at different q values for the quench of the IgG model system to $T_q = 4\,^{\circ}\mathrm{C}$.

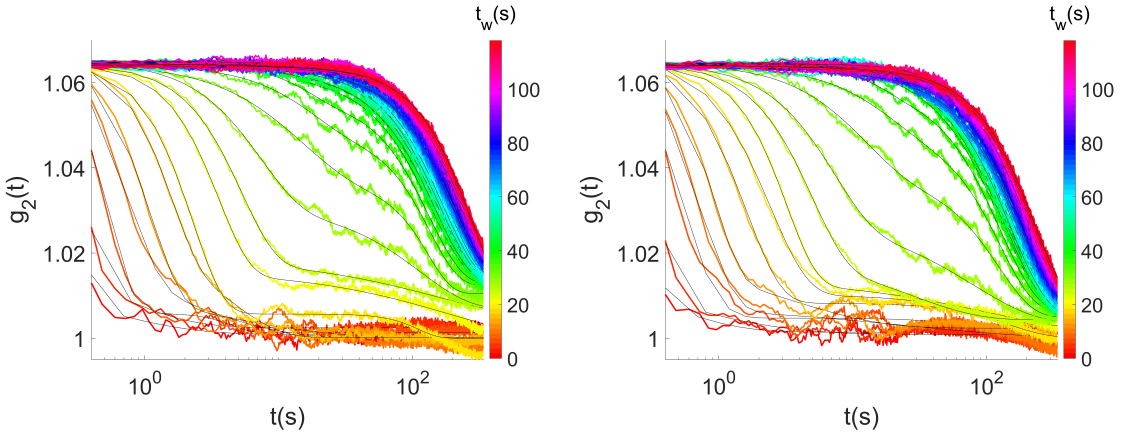

(a) $q = 0.0060\,\mathrm{nm}^{-1}$

(b) $q = 0.0065\,\mathrm{nm}^{-1}$

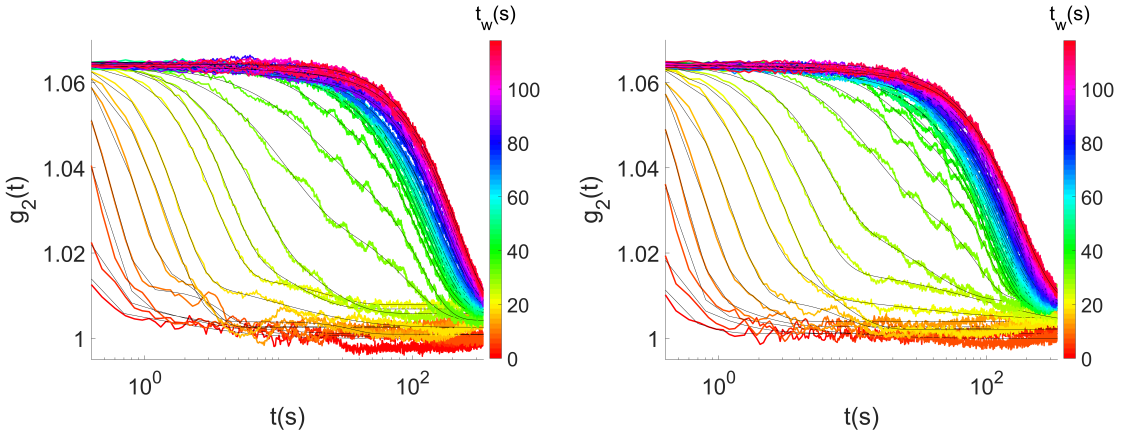

(c) $q = 0.0070\,\mathrm{nm}^{-1}$

(d) $q = 0.0075\,\mathrm{nm}^{-1}$

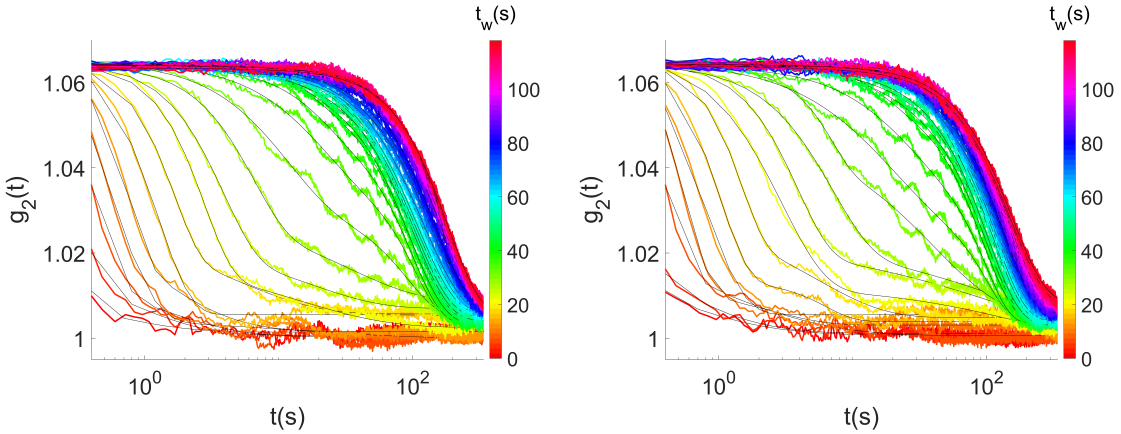

(e) $q = 0.0080\,\mathrm{nm}^{-1}$

(f) $q = 0.0085\,\mathrm{nm}^{-1}$

Figure A.18.: Correlation functions at different q values for the quench of the IgG model system to $T_q = 4\,^{\circ}\mathrm{C}$.

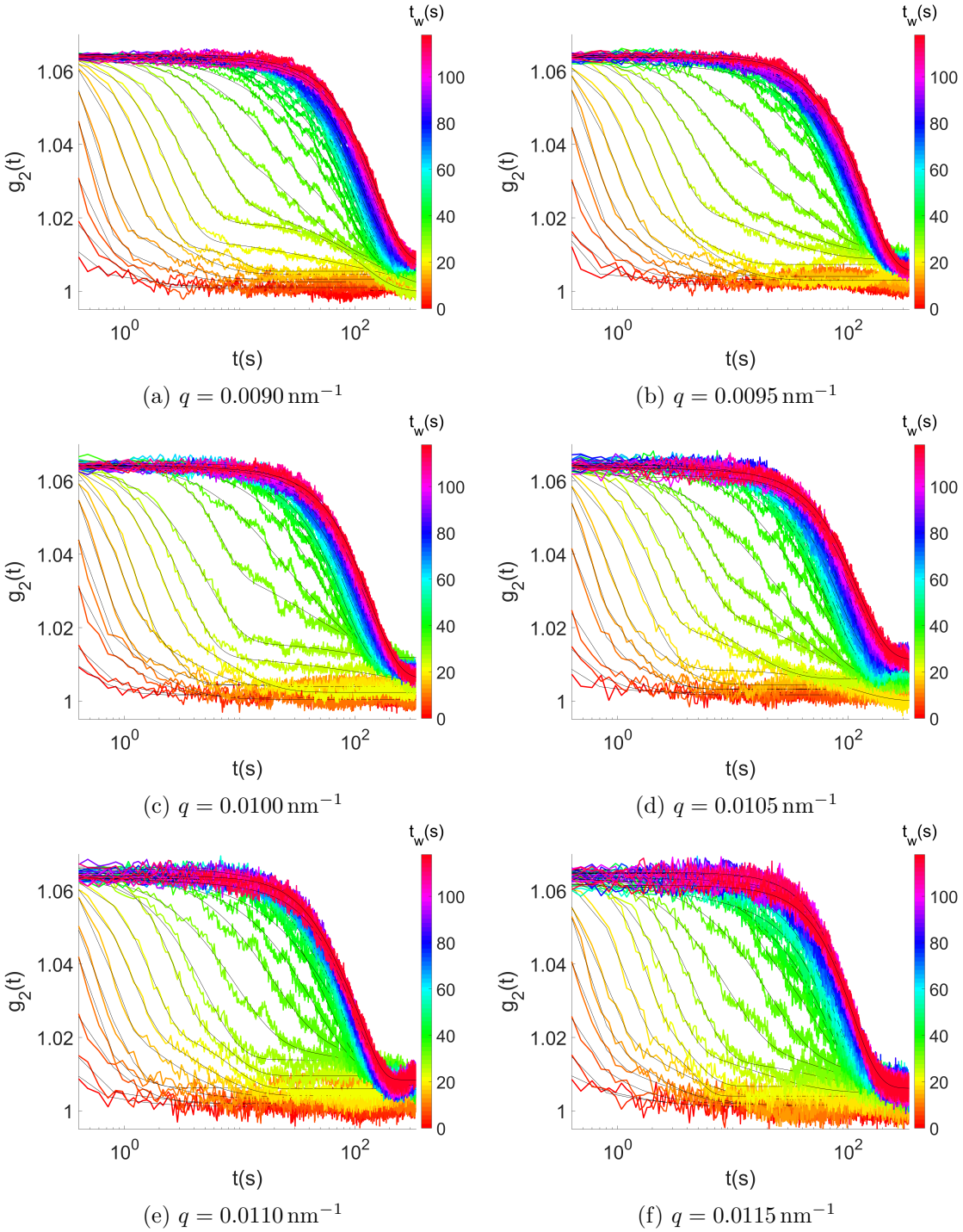

(a) $q = 0.0090\,\mathrm{nm}^{-1}$ (b) $q = 0.0095\,\mathrm{nm}^{-1}$

(c) $q = 0.0100\,\mathrm{nm}^{-1}$ (d) $q = 0.0105\,\mathrm{nm}^{-1}$

(e) $q = 0.0110\,\mathrm{nm}^{-1}$ (f) $q = 0.0115\,\mathrm{nm}^{-1}$

Figure A.19.: Correlation functions at different q values for the quench of the IgG model system to $T_q = 4\,^{\circ}\mathrm{C}$.

Bibliography

[1] Simon Alberti and Anthony A. Hyman. "Are aberrant phase transitions a driver of cellular aging?" In: *BioEssays* 38.10 (2016), pp. 959–968.

[2] Jens Als-Nielsen and Des McMorrow. *Elements of Modern X-Ray Physics*. John Wiley & Sons, Ltd, 2001.

[3] P. Ballesta, A. Duri, and L. Cipelletti. "Unexpected drop of dynamical heterogeneities in colloidal suspensions approaching the jamming transition." In: *Nature Phys* 4 (2008), 550–554.

[4] Adolfo J. Banchio and Gerhard Nägele. "Short-time transport properties in dense suspensions: From neutral to charge-stabilized colloidal spheres". In: *The Journal of Chemical Physics* 128.10 (2008), p. 104903.

[5] R. Bandyopadhyay et al. "Speckle-visibility spectroscopy: A tool to study time-varying dynamics". In: *Review of Scientific Instruments* 76.9 (2005), p. 093110.

[6] Ranjini Bandyopadhyay et al. "Slow dynamics, aging, and glassy rheology in soft and living matter". In: *Solid State Communications* 139.11 (2006). Soft Condensed Matter, pp. 589 –598. ISSN: 0038-1098.

[7] Ranjini Bandyopadhyay et al. "Slow dynamics, aging, and glassy rheology in soft and living matter". In: *Solid State Communications* 139.11 (2006). Soft Condensed Matter, pp. 589 –598. ISSN: 0038-1098.

[8] GB Benedek. "Cataract as a protein condensation disease: the Proctor Lecture." In: *Invest Ophthalmol Vis Sci.* 38 (10 1997), pp. 1911–1921.

[9] Joel Berry, Clifford P Brangwynne, and Mikko Haataja. "Physical principles of intracellular organization via active and passive phase transitions". In: 81.4 (2018), p. 046601.

[10] Oier Bikondoa. "On the use of two-time correlation functions for X-ray photon correlation spectroscopy data analysis". In: *Journal of Applied Crystallography* 50.2 (2017), pp. 357–368.

[11] K. Binder. "Collective diffusion, nucleation, and spinodal decomposition in polymer mixtures". In: *The Journal of Chemical Physics* 79.12 (1983), pp. 6387–6409.

[12] K. Binder. "Spinodal decomposition". In: *Systems Far from Equilibrium: Sitges Conference on Statistical Mechanics*. Ed. by Luis Garrido. Vol. 132. 1980, pp. 76–90.

[13] J. P. Bouchaud and E. Pitard. "Anomalous dynamical light scattering in soft glassy gels." In: *Eur. Phys. J. E* 6 (2001), pp. 231 –236.

[14] Saskia Bucciarelli et al. "Dramatic influence of patchy attractions on short-time protein diffusion under crowded conditions". In: *Science Advances* 2.12 (2016).

[15] John Alfred Valentine Butler, A. B. Robins, and Joseph Rotblat. "The inactivation of α-chymotrypsin by ionizing radiations". In: *Proceedings of the Royal Society of London. Series A. Mathematical and Physical Sciences* 256.1284 (1960), pp. 1–14.

[16] John W. Cahn. "Phase Separation by Spinodal Decomposition in Isotropic Systems". In: *The Journal of Chemical Physics* 42.1 (1965), pp. 93–99.

[17] John W. Cahn and John E. Hilliard. "Free Energy of a Nonuniform System. I. Interfacial Free Energy". In: *The Journal of Chemical Physics* 28.2 (1958), pp. 258–267.

[18] Frédéric Cardinaux et al. "Interplay between Spinodal Decomposition and Glass Formation in Proteins Exhibiting Short-Range Attractions". In: *Phys. Rev. Lett.* 99 (11 2007), p. 118301.

[19] Chiara Caronna et al. "Dynamics of Nanoparticles in a Supercooled Liquid". In: *Phys. Rev. Lett.* 100 (5 2008), p. 055702.

[20] Pinaki Chaudhuri and Jürgen Horbach. "Phase separation in dense glassy liquids: effect of quenching protocols". In: *Journal of Statistical Mechanics: Theory and Experiment* 2016.8 (2016), p. 084005.

[21] Luca Cipelletti et al. "Universal Aging Features in the Restructuring of Fractal Colloidal Gels". In: *Phys. Rev. Lett.* 84 (10 2000), pp. 2275–2278.

[22] R. A. Curtis, J. M. Prausnitz, and H. W. Blanch. "Protein-protein and protein-salt interactions in aqueous protein solutions containing concentrated electrolytes". In: *Biotechnology and Bioengineering* 57.1 (1998), pp. 11–21.

[23] Stefano Da Vela et al. "Arrested and temporarily arrested states in a protein–polymer mixture studied by USAXS and VSANS". In: *Soft Matter* 13 (46 2017), pp. 8756–8765.

[24] Stefano Da Vela et al. "Effective Interactions and Colloidal Stability of Bovine γ-Globulin in Solution". In: *The Journal of Physical Chemistry B* 121.23 (2017), pp. 5759–5769.

[25] Stefano Da Vela et al. "Kinetics of liquid–liquid phase separation in protein solutions exhibiting LCST phase behavior studied by time-resolved USAXS and VSANS". In: *Soft Matter* 12 (46 2016), pp. 9334–9341.

[26] B Derjaguin and L Landau. "Theory of the stability of strongly charged lyophobic sols and of the adhesion of strongly charged particles in solutions of electrolytes". In: *Progress in Surface Science* 43.1 (1993), pp. 30 –59. ISSN: 0079-6816.

[27] PETRA III synchrotron at DESY. *P10 Beamline layout*. 2020. URL: `https://photon-science.desy.de/facilities/petra_iii/beamlines/p10_coherence_applications/beamline_specifications/index_eng.html`.

[28] PETRA III synchrotron at DESY. *P10 Coherence Beamline User Guide*. 2016.

[29] Russel F. Doolittle. "The evolution of the vertebrate plasma proteins". In: *The Biological Bulletin* 172.3 (1987), pp. 269–283.

[30] A Duri and L Cipelletti. "Length scale dependence of dynamical heterogeneity in a colloidal fractal gel". In: *Europhysics Letters (EPL)* 76.5 (2006), pp. 972–978.

[31] William A. Eaton and James Hofrichter. "Sickle Cell Hemoglobin Polymerization". In: ed. by C.B. Anfinsen et al. Vol. 40. Advances in Protein Chemistry. Academic Press, 1990, pp. 63 –279.

[32] P. Falus, L. B. Lurio, and S. G. J. Mochrie. "Optimizing the signal-to-noise ratio for X-ray photon correlation spectroscopy". In: *Journal of Synchrotron Radiation* 13.3 (2006), pp. 253–259.

[33] A. Fulton. "How Crowded Is The Cytoplasm?" In: *Cell* 30.2 (1982), pp. 345–347.

[34] Hiroshi Furukawa. "Dynamics-scaling theory for phase-separating unmixing mixtures: Growth rates of droplets and scaling properties of autocorrelation functions". In: *Physica A: Statistical Mechanics and its Applications* 123.2 (1984), pp. 497 – 515. ISSN: 0378-4371.

[35] Yongxiang Gao, Juntae Kim, and Matthew E. Helgeson. "Microdynamics and arrest of coarsening during spinodal decomposition in thermoreversible colloidal gels". In: *Soft Matter* 11 (32 2015), pp. 6360–6370.

[36] Warren M. Garrison. "Reaction mechanisms in the radiolysis of peptides, polypeptides, and proteins". In: *Chemical Reviews* 87.2 (1987), pp. 381–398.

[37] Thomas Gibaud and Peter Schurtenberger. "A closer look at arrested spinodal decomposition in protein solutions". In: *Journal of Physics: Condensed Matter* 21.32 (2009), p. 322201.

[38] Thomas Gibaud et al. "New routes to food gels and glasses". In: *Faraday Discuss.* 158 (0 2012), pp. 267–284.

[39] Valeriy V. Ginzburg. "A simple mean-field model of glassy dynamics and glass transition". In: *Soft Matter* 16 (3 2020), pp. 810–825.

[40] A. Girelli et al. "Microscopic dynamics underlying arrested phase separation of a model protein solution revealed by XPCS". In preparation.

[41] L. Gmachowski. "Fractal model of anomalous diffusion." In: *Eur Biophys J* 44 (2015), pp. 613–621.

[42] J. W. Goodman. *Statistical Optics*. John Wiley & Sons, 2015.

[43] A. Guinier and G. Fournet. *Small-Angle Scattering of X-rays.* New York: W.H. Freeman and Company, 1955.

[44] Lisa J. Harris et al. "Refined Structure of an Intact IgG2a Monoclonal Antibody," in: *Biochemistry* 36.7 (1997), pp. 1581–1597.

[45] Tina Hecksher et al. "Toward broadband mechanical spectroscopy". In: 114.33 (2017), pp. 8710–8715. ISSN: 0027-8424.

[46] P. H. Hermans. *In H. R. Kruyt (Ed.), Colloid Science II (pp. 484).* Vol. 48. 4. Berlin, Boston: De Gruyter, 1976, pp. 471 –483.

[47] Clément Y. J. Hémonnot and Sarah Köster. "Imaging of Biological Materials and Cells by X-ray Scattering and Diffraction". In: *ACS Nano* 11.9 (2017), pp. 8542–8559.

[48] J. H. Hubbell. *Photon Cross Sections, Attenuation Coefficients, and Energy Absorption Coefficients From 10 keV to 100 GeV*. 1969.

[49] Anthony A. Hyman and Clifford P. Brangwynne. "Beyond Stereospecificity: Liquids and Mesoscale Organization of Cytoplasm". In: *Developmental Cell* 21.1 (2011), pp. 14 –16. ISSN: 1534-5807.

[50] J. Israelachvili. *Intermolecular and Surface Forces.* London, 3rd edition: Academic Press, 2011.

[51] J Jackle. "Models of the glass transition". In: *Reports on Progress in Physics* 49.2 (1986), pp. 171–231.

[52] Avni Jain et al. "Anisotropic and heterogeneous dynamics in an aging colloidal gel". In: *Soft Matter* 16 (11 2020), pp. 2864–2872.

[53] Cy M. Jeffries et al. "Limiting radiation damage for high-brilliance biological solution scattering: practical experience at the EMBL P12 beamline PETRAIII". In: *Journal of Synchrotron Radiation* 22.2 (2015), pp. 273–279.

[54] I Johnson et al. "Eiger: a single-photon counting x-ray detector". In: *Journal of Instrumentation* 9.05 (2014), pp. C05032–C05032.

[55] Karin Julius et al. “Impact of Macromolecular Crowding and Compression on Protein–Protein Interactions and Liquid–Liquid Phase Separation Phenomena”. In: *Macromolecules* 52.4 (2019), pp. 1772–1784.

[56] Ferenc KILÁR et al. “Conformation of human IgG subclasses in solution”. In: *European Journal of Biochemistry* 147.1 (1985), pp. 17–25.

[57] T. Kindt, R. Goldsby, and B. Osborne. *Kuby immunology.* New York: W.H. Freeman and Company, 2007.

[58] Nigel Kirby et al. “Improved radiation dose efficiency in solution SAXS using a sheath flow sample environment”. In: *Acta Crystallographica Section D* 72.12 (2016), pp. 1254–1266.

[59] Jan Kmetko et al. “Can radiation damage to protein crystals be reduced using small-molecule compounds?” In: *Acta Crystallographica Section D* 67.10 (2011), pp. 881–893.

[60] A Knaebel et al. “Aging behavior of Laponite clay particle suspensions”. In: *Europhysics Letters (EPL)* 52.1 (2000), pp. 73–79.

[61] Shigeo Kuwamoto, Shuji Akiyama, and Tetsuro Fujisawa. “Radiation damage to a protein solution, detected by synchrotron X-ray small-angle scattering: dose-related considerations and suppression by cryoprotectants”. In: *Journal of Synchrotron Radiation* 11.6 (2004), pp. 462–468.

[62] Sooheyong Lee et al. “Single shot speckle and coherence analysis of the hard X-ray free electron laser LCLS”. In: *Opt. Express* 21.21 (2013), pp. 24647–24664.

[63] P. Lu et al. “Gelation of particles with short-range attraction.” In: *Nature* 453 (2008), pp. 499–503.

[64] Anders Madsen et al. “Beyond simple exponential correlation functions and equilibrium dynamics in x-ray photon correlation spectroscopy”. In: *New Journal of Physics* 12.5 (2010), p. 055001.

[65] Liliana Malinovska, Sonja Kroschwald, and Simon Alberti. “Protein disorder, prion propensities, and self-organizing macromolecular collectives”. In: *Biochimica et Biophysica Acta (BBA) - Proteins and Proteomics* 1834.5 (2013). The emerging dynamic view of proteins:Protein plasticity in allostery,evolution and self-assembly, pp. 918 –931. ISSN: 1570-9639.

[66] S. Manley et al. “Glasslike Arrest in Spinodal Decomposition as a Route to Colloidal Gelation”. In: *Phys. Rev. Lett.* 95 (23 2005), p. 238302.

[67] MATLAB. *version R2018a.* Natick, Massachusetts: The MathWorks Inc., 2018.

[68] W. van Megen, S. M. Underwood, and P. N. Pusey. “Nonergodicity parameters of colloidal glasses”. In: *Phys. Rev. Lett.* 67 (12 1991), pp. 1586–1589.

[69] R. Mezzenga et al. "Understanding foods as soft materials." In: *Nature Mater* 4 (2005), pp. 729–740.

[70] Allen P. Minton. "The Influence of Macromolecular Crowding and Macromolecular Confinement on Biochemical Reactions in Physiological Media". In: *Journal of Biological Chemistry* 276.14 (2001), pp. 10577–10580.

[71] Johannes Möller and et. al. "Dynamics of biological samples traced by low dose X-ray Speckle Visibility Spectroscopy". In preparation.

[72] Johannes Möller et al. "X-ray photon correlation spectroscopy of protein dynamics at nearly diffraction-limited storage rings". In: *IUCrJ* 6.5 (2019), pp. 794–803.

[73] Efstratios Mylonas and Dmitri I. Svergun. "Accuracy of molecular mass determination of proteins in solution by small-angle X-ray scattering". In: *Journal of Applied Crystallography* 40.s1 (2007), s245–249.

[74] Janaky Narayanan and X.Y. Liu. "Protein Interactions in Undersaturated and Supersaturated Solutions: A Study Using Light and X-Ray Scattering". In: *Biophysical Journal* 84.1 (2003), pp. 523 –532. ISSN: 0006-3495.

[75] Robin Leslie Owen, Enrique Rudiño-Piñera, and Elspeth F. Garman. "Experimental determination of the radiation dose limit for cryocooled protein crystals". In: 103.13 (2006), pp. 4912–4917.

[76] Pierre Papon, Jacques Leblond, and Paul H. E. Meijer. *The Physics of Phase Transition*. Springer, 2002.

[77] Fivos Perakis and Christian Gutt. "Towards molecular movies with X-ray photon correlation spectroscopy". In: *Phys. Chem. Chem. Phys.* (2020).

[78] W.C.K. Poon et al. "Non-equilibrium behaviour of colloid-polymer mixtures". In: *Physica A: Statistical Mechanics and its Applications* 235.1 (1997). Proceedings of the Workshop on Colloid Physics, pp. 110 –119. ISSN: 0378-4371.

[79] Mario Reiser. "Xana".

[80] B. Ruta et al. "Wave-Vector Dependence of the Dynamics in Supercooled Metallic Liquids". In: *Phys. Rev. Lett.* 125 (5 2020), p. 055701.

[81] D Sappelt and J Jäckle. "Spinodal decomposition with formation of a glassy phase". In: *Europhysics Letters (EPL)* 37.1 (1997), pp. 13–18.

[82] Dirk Sappelt and Josef Jäckle. "Computer simulation study of phase separation in a binary mixture with a glass-forming component". In: *Physica A: Statistical Mechanics and its Applications* 240.3 (1997), pp. 453 –479.

[83] DESY photon science. URL: `https://photon-science.desy.de/research/students__teaching/primers/synchrotron_radiation/index_eng.html`.

[84] DESY photon science. *PETRA IV: Conceptual Design Report*. URL: https://bib-pubdb1.desy.de/record/426140/files/DESY-PETRAIV-Conceptual-Design-Report.pdf.

[85] Francesco Sciortino and Emanuela Zaccarelli. "Equilibrium gels of limited valence colloids". In: *Current Opinion in Colloid & Interface Science* 30 (2017), pp. 90 –96.

[86] Francesco Sciortino et al. "Interference of phase separation and gelation: A zeroth-order kinetic model". In: *Phys. Rev. E* 47 (6 1993), pp. 4615–4618.

[87] Yongdae Shin and Clifford P. Brangwynne. "Liquid phase condensation in cell physiology and disease". In: *Science* 357.6357 (2017). ISSN: 0036-8075.

[88] Oleg G. Shpyrko. "X-ray photon correlation spectroscopy". In: *Journal of Synchrotron Radiation* 21.5 (2014), pp. 1057–1064.

[89] Nicholas Skar-Gislinge et al. "A Colloid Approach to Self-Assembling Antibodies". In: *Molecular Pharmaceutics* 16.6 (2019), pp. 2394–2404.

[90] Robert J. Southworth-Davies et al. "Observation of Decreased Radiation Damage at Higher Dose Rates in Room Temperature Protein Crystallography". In: *Structure* 15.12 (2007), pp. 1531 –1541. ISSN: 0969-2126.

[91] National Institute of Standards and Technology. *Photon Cross Sections Database*. 2010. URL: https://www.nist.gov/pml/xcom-photon-cross-sections-database.

[92] Anna Stradner and Peter Schurtenberger. "Potential and limits of a colloid approach to protein solutions". In: *Soft Matter* 16 (2 2020), pp. 307–323.

[93] Hajime Tanaka and Yuya Nishikawa. "Viscoelastic Phase Separation of Protein Solutions". In: *Phys. Rev. Lett.* 95 (7 2005), p. 078103.

[94] E. J. W. Verwey and J. T. G. Overbeek. *Theory of the Stability of Lyophobic Colloids*. Amsterdam: Elsevier, 1948.

[95] Jan Verwohlt et al. "Low Dose X-Ray Speckle Visibility Spectroscopy Reveals Nanoscale Dynamics in Radiation Sensitive Ionic Liquids". In: *Phys. Rev. Lett.* 120 (16 2018), p. 168001.

[96] A. Vrij. "Polymers at Interfaces and the Interactions in Colloidal Dispersions". In: *Pure and Applied Chemistry* 48.4 (1976), pp. 471 –483.

[97] Ying Wang et al. "Phase transitions in human IgG solutions". In: *The Journal of Chemical Physics* 139.12 (2013), p. 121904.

[98] Stephanie C. Weber and Clifford P. Brangwynne. "Getting RNA and Protein in Phase". In: *Cell* 149.6 (2012), pp. 1188 –1191. ISSN: 0092-8674.

[99] Graham Williams and David C. Watts. "Non-symmetrical dielectric relaxation behaviour arising from a simple empirical decay function". In: *Trans. Faraday Soc.* 66 (0 1970), pp. 80–85.

[100] Z.W. Wu et al. "Stretched and compressed exponentials in the relaxation dynamics of a metallic glass-forming melt". In: *Nat Commun* 9 (2018), p. 5334.

[101] Isseki Yu et al. "Biomolecular interactions modulate macromolecular structure and dynamics in atomistic model of a bacterial cytoplasm". In: *eLife* 5 (2016). Ed. by Yibing Shan, e19274. ISSN: 2050-084X.

[102] Emanuela Zaccarelli. "Colloidal gels: equilibrium and non-equilibrium routes". In: *Journal of Physics: Condensed Matter* 19.32 (2007), p. 323101.

Acknowledgement

At this point I would like to thank all the people who supported me during the last years.

First I like to thank my supervisor and first reviewer **Christian Gutt**:
Dear Christian, thank you for giving me the opportunity to write my PhD thesis in the new and exciting field of protein dynamics research using XPCS. Many thanks for your excellent support during the last years. You have been a decisive help during the beamtimes. Thank you for your expertise, time and patience in discussing the results of this thesis.

I thank my second reviewer **Fajun Zhang** as well as the further examiners **Ulrich Jonas** and **Markus Risse** for their availability to be part of my defence.

Special thanks to **Mario Reiser** for the great support during the last years. Your Xana software has been a great help for the data analysis. Thank you for letting me work with Xana and for your time and patience with my questions about using the software. Furthermore, you were an outstanding support in preparing and performing the beamtimes at DESY. You always knew what to do when problems arose and it was a lot of fun to discuss the measurements with you.

Also special thanks to **Anita Girelli** for your collaboration investigating the dynamics of the IgG-PEG model system. Your simulations are a milestone to understand our data. Thank you for many shared shifts during our beamtimes, both for data discussion and also for many friendly moments during the strenuous beamtimes.

Furthermore, I would like to thank **Fabian Westermeier** for his support as beamline scientist during the beamtimes. No matter at what time of day or night we needed help to control the beamline, you patiently solved our problem and you did not lose your northern German calmness.

Moreover, thank you to **Fajun Zhang**, **Anita Girelli**, **Nafisa Begam**, **Anastasia Ragulskaya** and **Frank Schreiber** for the successful collaboration with the University of Tübingen in the field of protein dynamics. Many thanks for the preparation of the

samples. The joint beamtimes and the subsequent discussion were always great fun.

I like to thank my office mates **Lisa Randolph**, **Sonja Timmermann**, **Clémentine Lovato** and **Anna-Lena Becker** for the pleasant and sporty working environment. You were always helpful both in scientific discussions and with everyday problems. I will not forget your efforts to prepare a special 30th birthday for me.

Jan Verwohlt, thank you for your help to understand the XPCS method at the beginning of my time in Siegen.

I thank my master student **Kevin Lopata** for the time we spent together in the laboratory investigating the protein samples using DLS.

I would also like to thank the other members of the group **Dmitriy Ksenzov**, **Mohammad Akhundzadeh**, **Ahmed Al-Masoodi** and **Frederic Schon** for the common beamtimes. It was a pleasure to go out after work with the whole group for Christmas parties or bowling.

Finally, thanks to my **family** and my **friends** for their support over the last decade. I thank my **parents** for the seven great weeks in spring as a family at home in Norden, which saved me from living like a hermit on 35 square metres during the lockdown.

Erklärung

Ich erkläre hiermit an Eides statt, dass ich die vorliegende Arbeit ohne unzulässige Hilfe Dritter und ohne Benutzung anderer, nicht angegebener Hilfsmittel angefertigt habe. Die aus anderen Quellen direkt oder indirekt übernommenen Daten und Konzepte sind unter Angabe der Quelle gekennzeichnet.
Die Arbeit wurde bisher weder im In- noch im Ausland in gleicher oder ähnlicher Form einer anderen Prüfungsbehörde vorgelegt.
Es wurden keine Dienste eines Promotionsvermittlungsinstituts oder einer ähnlichen Organisation in Anspruch genommen.

Zu den vorgeschlagenen Mitgliedern der Promotionskommission bestehen keine verwandtschaftlichen Beziehungen, keine Verwandtschaft ersten Grades, Ehe, Lebenspartnerschaft oder ehe- ähnliche Gemeinschaft.

Siegen, den 29. September 2020

. . . . . .

Hendrik Rahmann